THE BINDING POCKETS OF Q_A AND Q_B IN THE PHOTOSYNTHETIC REACTION CENTER OF *RBA. SPHAEROIDES* PROBED BY PULSED EPR

BY

ERIK W. MARTIN

DISSERTATION

Submitted in partial fulfillment of the requirements
for the degree of Doctor of Philosophy in Biophysics and Computational Biology
in the Graduate College of the
University of Illinois at Urbana-Champaign, 2011

Urbana, Illinois

Doctoral Committee:

Professor Colin A. Wraight, Chair
Professor Robert B. Gennis
Professor Emeritus Anthony R. Crofts
Professor Emeritus Linn R. Belford

Abstract

The bacteria *Rhodobacter sphaeroides* uses photosynthetic reaction centers to convert light into chemical energy. Light absorption by the reaction center results in electron transfer through a series of cofactors, the final two are identical ubiquinones (Q_A and Q_B). Both ubiquinones can be stabilized in their reduced (semiquinone) state allowing for their binding pockets to be studied with EPR (electron paramagnetic resonance) spectroscopy. Using the pulsed EPR technique, ESEEM (electron spin echo envelope modulation) the interactions between the reaction center semiquinones and their environment were studied for wild type and a mutant reaction centers.

Nitrogen ESEEM modulations showed different nuclear couplings between the Q_A and Q_B sites. Both quinone sites showed two strongly coupled nitrogen nuclei. However, the hyperfine interactions were greater in magnitude at Q_A while the Q_B site showed a larger additional contribution from "matrix" nitrogen. Nitrogen ($S = 1$) has a quadruple moment and the quadrupole parameters are dependent on the electric field gradient at the nucleus of interest. Using these values, the two strongly coupled nitrogen nuclei were assigned to peptide and histidine for both quinone binding sites. The quadrupole asymmetry parameter was measureable only for the Q_A site nitrogen. An asymmetry parameter close to ~1 for the histidine nitrogen versus 0.63 for the peptide nitrogen is used to conclude that the histidine has a stronger H-bond than peptide.

Mutations to the M265 isoleucine in the Q_A site to the polar amino acids threonine or serine have shown a significant (80-100mV) change in redox potential versus the wild type. Comparing nitrogen ESEEM from the M265 threonine mutant to the wild type

provided insight into these redox potential changes. While nitrogen hyperfine parameters were nearly unchanged between the histidine and the Q_A semiquinone, changes in the quadrupole parameters indicate a significant change in the electric field gradient. Additionally, resolution of the hyperfine coupling between the peptide nitrogen and the semiquinone is decreased in the mutant.

Proton ESEEM showed a 2 exchangeable protons coupled to Q_A while there were up to 4 coupled to Q_B. In the Q_A site these are assigned to histidine at M219 and alanine at M260. In order to assign the protons in the Q_B site, experimental parameters were compared to ONIOM (QM/MM) calculations. The protons coupled to Q_B were thus assigned to histidine at L190, peptide protons from L225 and L224 and a serine hydroxyl from L223.

Acknowledgements

I would like to thank Dr. Colin Wraight who always allowed me the freedom to make own mistakes and pursue courses of study that piqued my interest, while simultaneously pushing me and giving honest criticism when needed, Colin's impact on me as a scientist and a person are undeniable. I will always be thankful for the impact working with him had on my life. This thesis would not have been possible without his help.

Additionally, I owe a lot to Dr. Sergei Dikanov who taught me everything I know about magnetic resonance spectroscopy. I believe it took several years learning the techniques used in this thesis before I understood them well enough to truly appreciate both the elegance of the data that could be obtained, and how wonderful and knowledgeable of a teacher I had in Sergei. Few people have the opportunity to work with such an expert in their field.

I am also indebted to my many of my colleagues. Dr. Eiji Takahashi, and Aidas Mattis provided the site directed mutations to the reaction centers used in this work. In particular, Eiji's knowledge of the, often mysterious, art of molecular biology was crucial. I would also like to thank Dr. Sasha Kokhan with whom I had many conversations about our research and research in general.

Finally, I am indebted to my family particularly my mother and father for their constant support and my good friends Molly Bartlett and Mike Konczal who always had faith in me.

Table of Contents

Chapter 1: General Introduction To *Rhodobacter sphaeroides* Reaction Centers ……...1

Abstract……1

Introduction……..2

RC Structure, Composition and Cofactors……...3

Electron Transfer Reactions…….4

Q_A and Q_B Binding Pockets……..5

Mutation of Residue M265 in the Q_A Pocket……..7

Mutation of Residue L223 in the Q_B Pocket…….10

Reaction Center Optical Spectroscopy……..11

Discussion……..12

References……..14

Figures……18

Chapter 2: Cell Growth and Isolation and Preparation of Photosynthetic Reaction Centers

(RCs)……..24

Abstract……..24

Introduction……25

Cell Growth and RC Isolation……26

RC Metal Exchange……...31

RC Sample Analysis……..36

Discussion……..39

References……..……41

Figures……43

Chapter 3: Electron Paramagnetic Resonance: Theory and Application to Reaction Center Quinones from *Rba. sphaeroides*……...45

Abstract……..45

Introduction……46

Basic CW-EPR Theory……..47

CW-EPR Spectroscopy and Photosynthetic Reaction Center Quinones……...52

Electron Nuclear Double Resonance (ENDOR) Spectroscopy…….55

ESEEM (Electron Spin Echo Envelope Modulation) Spectroscopy…….60

References……..75

Figures……77

Chapter 4: The Structure of Nitrogen Electronically Coupled to Q_A^- and Q_B^- - Computational and Pulsed EPR Studies……85

Abstract……..85

Introduction……...…….86

Q_A site EPR Spectroscopy and Coupled Nitrogen…….88

Q_B site EPR Spectroscopy and Coupled Nitrogen ……97

Analysis of NQI Parameters for Q_A and Q_B…….102

Analysis of the HFI Tensors for Q_A and Q_B .……..106

References……112

Figures……..116

Chapter 5: Mutation of the Residue M265 Isoleucine to Threonine Examined by Pulsed EPR……..124

Abstract……124

Introduction……..125

Q_A^- Sample Generation in M265IT Mutants……130

1D 3-pulse ESEEM of the M265IT Q_A Semiquinone……..131

2D HYSCORE of the M265IT Q_A Semiquinone…….132

Analysis of the NQI Parameters ..……...133

Analysis of the HFI Parameters…….……..135

Molecular Dynamics Investigation of M265IT Mutant RCs……...136

Conclusions……..138

References……140

Figures……..143

Chapter 6: The Protons Hydrogen Bonded to the Q_A and Q_B Semiquinones Studied by Pulsed EPR...……...151

Abstract……151

Introduction……..152

Sample Preparation……..154

^{1}H ENDOR of Q_A^- in the Context of HYSCORE……155

Q_A Semiquinone ^{1}H HYSCORE……..159

Q_B Semiquinone ^{1}H HYSCORE……..164

Discussion……167

Conclusions……..171

References……173

Figures……..175

Chapter 1:

General Introduction to *Rhodobacter sphaeroides* Reaction Centers

Abstract

This chapter introduces the experimental system used in this thesis, the photosynthetic reaction center from *Rhodobacter sphaeroides*. The secondary and tertiary structure of the reaction center, and especially the binding sites for the quinones, Q_A and Q_B, are described in detail. The optical and kinetic properties of the RC are also described and the significance of mutations at the M265 and L223 residues is discussed. The aims of the subsequent chapters are outlined in the final section.

Introduction

Electron transfer reactions are ubiquitous in biology and are central to respiration, metabolism and photosynthesis. Understanding the complex interactions between the enzymes and cofactors that facilitate these processes is greatly assisted by the use of a model system. The studies presented in the following chapters will use the photosynthetic reactions in the bacterium *Rhodobacter (Rba.) sphaeroides*, which contains photosynthetic machinery that is simple relative to those in oxygenic photosynthetic bacteria and higher plants.

Rba. sphaeroides is a purple non-sulfur photosynthetic bacterium in the alpha subclass of the Proteobacteria. The bacterium is capable of adapting to different growth environments by using several different metabolic pathways. Photosynthesis is the primary form of energy transduction in these organisms under anaerobic conditions in the light. The *Rba. sphaeroides* photosynthetic machinery is located in membrane folds and the periplasmic space (between the cell membrane and outer cell wall).

The photosynthetic electron transport pathway involves the cyclic reduction and oxidation of ubiquinone cofactors by a type II photosynthetic reaction center, soluble cytochrome *c* and cytochrome bc_1 complex. The reaction center (RC) is a bacteriochlorophyll containing pigment-protein complex. It is surrounded by light harvesting complexes (LHI and LHII) that assist in funneling the energy of photons to a photoactive "special pair" of bacteriochlorophylls (P) in the RC. In less than a nanosecond following light absorption, the RC forms a semistable charge separated state,

in which the excited stated P^* transfers an electron to an acceptor quinone, Q_A. The oxidized donor, P^+, is reduced by soluble cytochrome c_2 located in the periplasm. The absorption of a second photon is coupled to another electron transfer and the uptake of two protons, resulting in double reduction of the secondary acceptor quinone, Q_B, to quinol, which is free to diffuse in the membrane. The cytochrome bc_1 complex couples the oxidation of quinol to the net movement of two protons across the membrane and rereduction of cytochrome *c* completing the cycle.(*1-3*)

RC Structure, Composition and Cofactors

The function of the RC is to convert light energy into electrochemical energy including the reduction of quinone and generation of a membrane potential. Functionally and structurally the RC in *Rba. sphaeroides* is a close analog to photosystem II in higher plants. (Figure 1.1) The primary transmembrane region of the RC contains the core cofactors and consists of a heterodimer of two subunits designated L and M.(*4-6*) These two subunits are arranged around a pseudo two-fold rotational symmetry and have significant, 33%, identity.(*7*) A third RC subunit, H, contains one transmembrane helix anchoring it in the membrane and a soluble domain that caps the L and M polypeptides on the cytosolic side of the membrane.(*8-10*) The H subunit contains none of the active cofactors, but contributes to RC structural stability and contains residues implicated in proton transfer.(*2, 11-18*) (Figure 1.1)

The subunits L and M each contain five transmembrane helices and bind all the active cofactors - four bacteriochlorophylls, two bacteriopheophytins, two ubiquinones, and a histidine-liganded non-heme, high spin, ferrous iron. (*3, 19*) The cofactors are

arranged into A and B branches exhibiting the same symmetry as the LM dimer.(*2*) Each branch originates at the primary donor (P), near the periplasmic side of the membrane, and continues through a single bacteriochlorophyll (B) and bacteriopheophytin (H).(Figure 1.1) The A and B branches terminate, respectively, at the acceptor quinones Q_A and Q_B, which, in the case of *Rba. sphaeroides,* are identical ubiquinone-10 molecules. The high spin iron is located midway between these quinones along the plane of the membrane. The axis of symmetry can be drawn through the Fe^{2+} and the center of the special pair, normal to the plane of the membrane.

Electron Transfer Reactions

Despite the well defined symmetry, electron transfer is asymmetric, only occurring along a pathway through the A branch, including bacteriochlorophyll and bacteriopheophytin bound to the L subunit, and Q_A bound to the M subunit. The electron transfer reactions are initiated at the photo-generated excited singlet of the primary donor, P^*. An electron is transferred down a potential gradient from P^* through BChl (or by a super-exchange mechanism) to BPhe in a very short time, ~3 ps, and then transferred on to Q_A in ~200 ps. (*3, 20*) If the Q_B site is occupied, electron transfer proceeds further, from Q_A to the Q_B, in ~100 μs. In the absence of cytochrome *c* or any similar secondary electron donor to reduce P^+, these semiquinone species are not stable and relax via both thermal and electron tunneling mechanisms from Q_A^- in ~100 ms and from Q_B^- in ~1 s. (*2*) If cytochrome *c* - or another secondary donor - is present, P^+ will be rereduced to P, trapping the state $P(Q_AQ_B)^-$ which is quite long-lived (many minutes). After

photoactivation a second electron can be transferred to Q_B and is coupled to the uptake of two protons.

First photon: $PQ_AQ_B \xrightarrow{h\nu} P^+Q_A^-Q_B \leftrightarrow P^+Q_AQ_B^-$

Second photon: $PQ_AQ_B^- \xrightarrow{h\nu} P^+Q_A^-Q_B^- + H^+ \leftrightarrow P^+Q_A^-Q_BH + H^+ \leftrightarrow P^+Q_AQ_BH_2$

The doubly reduced quinol Q_BH_2, produced after the second electron transfer, can diffuse out of the binding pocket and be replaced by an oxidized quinone, restarting the cycle.

Despite being chemically identical, the functions of the two acceptor quinones are dramatically different. Q_A is a tightly bound prosthetic group, only capable of one electron chemistry, and facilitates the double reduction of Q_B. Additionally, the equilibrium of electron transfer favors the "forward" direction, the reduced state of Q_B being at lower free energy than reduced Q_A (The equilibrium between Q_A^- and Q_B^- can be described by: $K_{AB} = e^{-(\Delta G/kT)}$). Since Q_A and Q_B are chemically identical, it is inferred that the local protein environment in the quinone binding pockets and, at larger distances, electrostatic effects, are responsible for imparting these functional differences.

Q_A and Q_B Binding Pockets

High resolution crystal structures of the RC have provided a lot of insight into the structure of the quinone binding pockets.(*4, 10*) Knowledge of protein features in the immediate regions of bound Q_A and Q_B is important in generating a framework through which relationships between protein structure and quinone function can be viewed. Even though there are substantial functional differences between the two quinones, presumably originating from their interaction with the protein, there are many similarities between the two binding pockets. Both quinones are located in interhelical loops located

symmetrically around the non-heme Fe^{2+}. (Figure 1.2) In both binding pockets, the quinones are H-bonded through their O4 carbonyl to the Nδ of a histidine coordinated with the Fe^{2+}. In the case of Q_A, this residue is M219 with an Nδ to O4 heavy atom distance of 2.80±0.15 Å, from the average of available crystal structures.(*3*) In molecular dynamics simulations, the average distance over an ~15 ns trajectory is slightly longer, with average distances close to 3 Å.[1] (Figure 1.3)

Q_B is observed in crystal structures to occupy at least two different conformations - an inactive form, distal to the non-heme Fe^{2+}, and a proximal configuration. (*9*) All structures obtained from crystals frozen in the charge separated state show Q_B in the proximal position and it is concluded that this is the "active" conformation. The proximal conformation shows the Q_B O4 carbonyl H-bonded to the Nδ of the Fe ligand histidine at L190 at a distance of 2.69±0.23 Å.(*3*) Within the resolution of the crystal structures, this distance is nearly identical to the C4 hydrogen bond in Q_A. After ~15 ns of relaxation in molecular dynamics simulations, the average H-bond distance is close to 3 Å, similar to Q_A. (Figure 1.4)

The O1 carbonyl of Q_A is H-bonded to the backbone NH from alanine at M260 with a heavy atom distance estimated from crystal structures to be 2.79±0.09 Å.(*3*) Isoleucine at M265 and tryptophan at M252 are close enough to be in van der Waals contact with the quinone head group and could contribute to the structural stability of the binding site. Trp-M252 is oriented with its aromatic side chain nearly parallel to the quinone head group and has been suggested to be involved in π stacking interactions with

[1] Molecular dynamics trajectories were run using the program NAMD, starting with coordinates from crystal structure 1AIG.pdb and relaxed in a lipid bilayer and water box. Unless otherwise indicated distances measured from MD trajectories are the average distance while the trajectory is in a steady state.

the quinone.(*21*) However, it is unclear if these specific interactions exist, or what effect they would have on electron transfer, but at least van der Waals interactions are clearly important to quinone binding.(*21, 22*)

H-bonding interactions at the Q_B O1 carbonyl are less defined than in the Q_A binding pocket, but there is still presumed to be a hydrogen bond to a peptide backbone amide nitrogen when in the proximal position. Crystal structures suggest that Ile-L224, Gly-L225, or both are potential hydrogen bond donors, with approximate heavy atom distances of 2.96 Å and 3.27 Å, respectively. After molecular dynamics relaxation, the picture is no clearer with both L224 and L225 having nearly identical average heavy atom distances of ~2.8 Å.[2] (Figure 1.5) There are a number of additional residues near to Q_B in the proximal position, none of which seem to directly mirror the VDW interactions present in the Q_A site – potentially contributing to the different binding behavior between quinone sites.

Peculiar to the Q_B binding site is the possibility of a H-bond between the sidechain OH from serine L223 and the O1 carbonyl. (Figure 1.3) Ser-L223 could both play a role in stabilizing the semiquinone state, and assist in proton transfer.(*23*) The side chain hydroxyl is expected to form a H-bond to Asp-L213 in the dark adapted state and could rotate to the quinone O1 carbonyl after charge separation.(*24*)

Mutation of Residue M265 in the Q_A Pocket

Ile-M265 is in van der Waals contact with the Q_A headgroup - specifically the C3-methoxy, O4 carbonyl, C5, C6 and the C5' methyl. Its close proximity to, and presumed

[2] Molecular dynamics trajectories show that the average H-bond length between Q_A O1 and the M260 peptide N is similar, but slightly larger at 3.06 Å.

interaction with, the quinone made this residue a good candidate for site directed mutagenesis. The bulky isoleucine at M265 was mutated to the small amino acids valine, serine and threonine, reducing van der Waals contact and, in the case of serine and threonine, introducing a hydroxyl group. Differences in the measured rate of charge recombination indicated that the polar mutations, threonine and serine, at M265 lowered the midpoint potential of Q_A by ~100 and 85 mV respectively, while valine had little effect.(*22, 25*) Similar results (~115 and 60 mV for threonine and serine) were obtained when the free energy of Q_A^- was directly measured via the delayed fluorescence from $P^+Q_A^-$.(*26*) The existence of this shift only in the threonine and serine mutants indicates that the hydroxyl group, and not simply a difference in size, generates this shift.

The orientations of quinone methoxy groups have been implicated in redox poising.(*27*) Small amino acids at M265 could allow for a greater number of conformations than in wild type and polar sidechains from threonine or serine could stabilize a specific, alternate, methoxy conformation through H-bonding. However, substituting the native ubiquinone with anthraquinone, which lacks any methoxy groups, showed similar energetic effects, eliminating methoxy orientation as a significant contributor to the cause of the redox shift. (*22*)

These mutations can affect the protein-quinone interactions by changing binding pocket structure, specific steric or van der Waals interactions with Q_A, or electrostatically. H-bonding has been shown to substantially affect the redox potential of cofactors in the RC. (*28-30*) Rotamers generated by rotating the C_α-C_β bond of threonine or serine showed potential hydrogen bonding and steric interactions with binding site residues M261-M262. It was suggested that the global result could involve a movement

of the peptide backbone away from the quinone, increasing the hydrogen bond distance between the O1 carbonyl and the Ala-M260 peptide NH. Energy minimization using GROMOS96 showed that the H-bond could be lengthened by ~0.1 Å.(*25*)

Fourier transform IR spectroscopy was used to explore small structural changes in the M265 mutants. (*25*) Spectra showing differences between the semiquinone and neutral quinone showed a number of unassigned shifts relative to the wild-type, but a distinct upshift of the 1601 cm^{-1} band to 1603 cm^{-1} stands out. This IR band is assigned to the O4 carbonyl stretch. (*31*) The implication is that there is some change in the H-bonding between this carbonyl and the Nδ from His M219. There were no energetically favorable rotamers where the M265 sidechain would directly interact with the O4 carbonyl or His-M219, but a change in the H-bond to the O1 carbonyl could affect the overall position of the quinone causing this shift. The slight increase in H-bond length at the O1 carbonyl that was suggested would be expected to generate a shift around 1660 cm^{-1}, but this was unresolved due to overlap with the amide I band.(*25*)

The hypothesis that polar mutations at M265 push the protein backbone away from the O1 side of Q_A is plausible, but FTIR data provided only hints of this, and no confirmation. Recent crystal structures, as well as Molecular Dynamics and EPR data that will be presented in Chapter 5, aim to add clarity to the mechanism(s) causing the redox potential shift in these mutants. There do not seem to be any significant changes in Q_A binding site geometry and it is possible that, in addition to tiny shifts in H-bond distances, the hydroxyl introduced by the polar mutations has a direct electrostatic effect.

Mutation of Residue L223 in the Q_B Pocket

Protein dynamics play a significant role in the electron transfer between the acceptor quinones. The rate of the first electron transfer between quinones is not congruent with rates estimated by the distance between the donor and acceptor alone, suggesting an impact from conformational gating.(*32*) Additionally, protein relaxation is required for electron transfer to Q_B and is apparent in the temperature dependence of the reaction.(*3*) Charge separation between P^+ and Q_A^- is possible at cryogenic temperatures, but electron transfer to Q_B displays a temperature dependence, and is effectively blocked in RCs frozen in the dark.(*33*)

The relative stability of Q_B^- suggests contributions from the protein environment. Serine at L223 has been proposed to switch hydrogen bonding partners between the semiquinone O1 carbonyl and Asp-L213.(*24*) A significant decrease in the proton coupled second electron transfer rate was observed when L223 was mutated to alanine (from ~1300 s^{-1} in wild type to ~4 s^{-1} in the alanine mutant). (*34, 35*) However, the exact contribution Ser-L223 makes to the stabilization of Q_B^- is unclear.

Recent Q-band ENDOR data suggested that the hydrogen bond to the quinone is formed on generation of Q_B^-.(*24, 36*) When L223 is mutated to alanine a peak associated with hyperfine splitting of one exchangeable proton disappears. In ENDOR samples of a RC mutant designed to allow electron transfer via the B branch, Q_B^- can be generated at cryogenic temperatures by exposure to an actinic light source. In this mutant, samples can be prepared in the dark-adapted state and be frozen prior to generation of Q_B^- eliminating any protein relaxation in response to semiquinone formation.(*24*) The L223

serine to alanine mutant appeared to have a similar structure to the Q_B site in dark adapted RCs. It was concluded that the serine hydroxyl is only coupled to the semiquinone after electron transfer to Q_B at non-cryogenic temperatures. When not H-bonded to Q_B, the serine hydroxyl probably H-bonds to Asp-L213. The presence of an additional hydrogen bond to the semiquinone O1 carbonyl could play a role in the stabilization of this species. Further examination of H-bonding partners to Q_B is required to aid in this model. Chapter 6 will examine proton couplings, using pulsed EPR, and will clarify the picture of H-bonding to Q_B.

Reaction Center Optical Spectroscopy

Reaction center cofactors absorb light at characteristic ultraviolet (UV), visible (Vis) and near infra-red (NIR) wavelengths. Well characterized extinction coefficients at specific wavelengths facilitate straight-forward analysis of RC preparation, yield and quality, cofactor redox states, and electron transfer kinetics. While the primary experiments presented in the following chapters use EPR techniques, all RCs used were first assayed by optical spectroscopy.

The UV-Vis-NIR spectrum shows peaks characteristic of RCs – in particular, three peaks between ~700 nm and ~900 nm.(Figure 1.6) In the center of this region is a dominant peak at 802 nm, attributable to bacteriochlorophyll absorption with an extinction coefficient of $\varepsilon = 0.288\ \mu M^{-1}\ cm^{-1}$. The 802 nm peak can be used to measure the concentrations of RC samples and the ratio of this peak to 280 nm (tryptophan absorption) is used to determine RC purity. This is discussed in Chapter 2 in the context of RC isolation and purification.

Bacteriopheophytin absorbs light at 755 nm and the bacteriochlorophyll dimer absorbs at 860 nm. Generally, these two peaks are of nearly equal intensity and about 50% of the intensity of 802 nm bacteriochlorophyll peak. The peak at 860 nm almost disappears when the primary donor is fully oxidized and can be bleached by a strong spectrophotometer measuring beam, or exposure to light. Additional peaks attributable to bacteriopheophytin and bacteriochlorophyll are seen at 540 nm and 600 nm respectively.(*37*) Semiquinones and the oxidized primary donor both have absorbance at 430-450 nm. Charge recombination and electron transfer between the quinones can be measured as transient changes in absorption following light activation . (*38, 39*)

Discussion

Many of the specifics of the electron transfer reactions and the redox properties of the RC cofactors are known and have been reviewed many times.(*2, 3, 6, 38, 40-42*) The fact that this system is so well characterized is an advantage when examining interactions between the cofactors and protein. The aim of the work in this thesis is to integrate the knowledge of quinone electrochemistry and binding pocket structures with modern pulsed EPR techniques to examine the interplay between protein and semiquinones.

The major methodological elements will be presented in Chapters 2 and 3. Generating high quality samples with high concentrations of the desired paramagnetic species is one of the chief difficulties in obtaining pulsed EPR data. Chapter 2 will outline the growth, isolation and preparation of RCs. The preparation of RCs for EPR study requires biochemical replacement of the native ferrous Fe with a diamagnetic Zn.

Chapter 3 discusses the theory of EPR measurements, especially pulsed techniques, in the context of the current state of EPR research on RC quinones.

Pulsed EPR data describing nitrogen couplings to Q_A^- and Q_B^- are presented in Chapter 4. The quadrupole parameters and hyperfine coupling constants provide new information about the H-bonding partners to quinones. This information is used in Chapter 5 to provide insight into the source of the redox potential drop of the Q_A semiquinone in the M265 isoleucine to threonine mutant. Chapter 6 describes measurements of the proton couplings to the RC quinones, and further elaborates the picture of H-bonding in the Q_A and Q_B sites.

References

1. Okamura, M. Y., Paddock, M. L., Graige, M. S., and Feher, G. (2000) Proton and electron transfer in bacterial reaction centers. *Biochim. Biophys. Acta 1458*, 148-163.
2. Wraight, C. A. (2004) Proton and electron transfer in the acceptor quinone complex of photosynthetic reaction centers from *Rhodobacter sphaeroides*. *Frontiers Biosci. 9*, 309-337.
3. Wraight, C. A., and Gunner, M. R. (2009) The Acceptor Quinones of Purple Photosynthetic Bacteria- Structure and Spectroscopy, In *Advances in Photosynthesis and Respiration: The Purple Photosynthetic Bacteria* (Hunter, C. N., Daldal, F., Thurnauer, M., and Beatty, J. T., Eds.), pp 379-405, Springer, Dordrecht, The Netherlands.
4. Feher, G., Allen, J. P., Okamura, M. Y., and Rees, D. C. (1989) Structure and function of bacterial photosynthetic reaction centres. *Nature 339*, 111-116.
5. Feher, G., and Okamura, M. Y. (1978) Chemical composition an properties of reaction centers, In *The Photosynthetic Bacteria* (Clayton, R. K., and Sistrom, W. R., Eds.), pp 349-386, Plenum, New York.
6. Feher, G., Okamura, M. Y., and McElroy, J. D. (1972) Identification of an electron acceptor in reaction centers of *Rhodopseudomonas spheroides* by EPR spectroscopy. *Biochim. Biophys. Acta 267*, 222-226.
7. Williams, J. C., Steiner, L. A., and Feher, G. (1986) Primary structure of the reaction center from *Rhodopseudomonas sphaeroides*. *Proteins: Structure, Function, and Bioinformatics 1*, 312-325.
8. Deisenhofer, J., Epp, O., Miki, K., Huber, R., and Michel, H. (1984) X-ray structure analysis of a membrane protein complex. Electron density map at 3 Å resolution and a model of the chromophores of the photosynthetic reaction center from *Rhodopseudomonas viridis*. *J. Mol. Biol. 180*, 385-398.
9. Stowell, M. H. B., McPhillips, T. M., Rees, D. C., Soltis, S. M., Abresch, E., and Feher, G. (1997) Light-induced structural changes in photosynthetic reaction center: implication for mechanism of electron-proton transfer. *Science 276*, 812-816.
10. Koepke, J., Eva-Maria Krammer, E.-M., Klingen, A. R., Sebban, P., Ullmann, G. M., and Fritzsch, G. (2007) pH modulates the quinone position in the photosynthetic reaction center from *Rhodobacter sphaeroides* in the neutral and charge separated states. *J. Mol. Biol. 371*, 13.
11. Paddock, M. L., Rongey, S. H., Feher, G., and Okamura, M. Y. (1989) Pathway of proton transfer in bacterial reaction centers: replacement of glutamic acid 212 in the L subunit by glutamine inhibits quinone (secondary acceptor) turnover. *Proc. Natl. Acad. Sci. USA 86*, 6602-6606.

12. M. L. Paddock, P. H. M., G. Feher, M. Y. Okamura (1990) Pathway of proton transfer in bacterial reaction centers: Replacement of serine-L223 by alanin inhibits electron and proton transfers associated with reduction of quinone to dihydroquinone. *Proc. Nat. Acad. Sci. USA 87*, 5.
13. Takahashi, E., and Wraight, C. A. (1992) Proton and electron transfer in the acceptor quinone complex of *Rhodobacter sphaeroides* reaction centers: characterization of site-directed mutants of the two ionizable residues, GluL212 and AspL213, in the Q_B binding site. *Biochemistry 31*, 855-866.
14. Paddock, M. L., Rongey, S. H., McPherson, P. H., Juth, A., Feher, G., and Okamura, M. Y. (1994) Pathway of proton transfer in bacterial reaction centers: role of aspartate-L213 in proton transfers associated with reduction of quinone to dihydroquinone. *Biochemistry 33*, 734-745.
15. Paddock, M. L., Feher, G., and Okamura, M. Y. (1997) Proton and electron transfer to the secondary quinone (Q_B) in bacterial reaction centers: the effect of changing the electrostatics in the vicinity of Q_B by interchanging asp and glu at the L212 and L213 sites. *Biochemistry 36*, 14238-14249.
16. Paddock, M. L., Graige, M. S., Feher, G., and Okamura, M. Y. (1999) Identification of the proton pathway in bacterial reaction centers: inhibition of proton transfer by binding of Zn^{2+} or Cd^{2+}. *Proc. Natl. Acad. Sci. USA 96*, 6183-6188.
17. Adelroth, P., Paddock, M. L., Sagle, L. B., Feher, G., and Okamura, M. Y. (2000) Identification of the proton pathway in bacterial reaction centers: both protons associated with reduction of Q_B to Q_BH_2 share a common entry point. *Proc. Natl. Acad. Sci. USA 97*, 13086-13091.
18. Wraight, C. A. (2006) Chance and design - proton transfer in water, channels and bioenergetic proteins. *Biochim. Biophys. Acta 1757*, 886-912.
19. Abresch, E. C., Paddock, M. L., Stowell, M. H. B., McPhillips, T. M., Axelrod, H. L., Soltis, S. M., Rees, D. C., Okamura, M. Y., and Feher, G. (1998) Identification of proton transfer pathways in the X-ray crystal structure of the bacterial reaction center from *Rhodobacter sphaeroides*. *Photosynth. Res. 55*, 119-125.
20. Woodbury, N. W., Becker, M., Middendorf, D., and Parson, W. W. (1985) Picosecond kinetics of the initial photochemical electron-transfer reaction in bacterial photosynthetic reaction centers. *Biochemistry 24*, 7516-7521.
21. Stilz, H. U., Finkele, U., Holzapfel, W., Lauterwasser, C., Zinth, W., and Oesterhelt, D. (1994) Influence of M subunit Thr222 and Trp252 on quinone binding and electron transfer in *Rhodobacter sphaeroides* reaction centres, *Eur. J. Bioch. 223*, 233-242.
22. Takahashi, E., Wells, T. A., and Wraight, C. A. (2001) Protein control of the redox potential of the primary quinone acceptor in reaction centers from *Rhodobacter sphaeroides*. *Biochemistry 40*, 1020-1028.
23. Paddock, M. L., Feher, G., and Okamura, M. Y. (1995) Pathway of proton transfer in bacterial reaction centers: further investigations on the role of Ser-L223 studied by site-directed mutagenesis. *Biochemistry 34*, 15742-15750.

24. Paddock, M. L., Flores, M., Isaacson, R., Chang, C., Abresch, E. C., and Okamura, M. Y. (2007) ENDOR spectroscopy reveals light induced movement of the H-bond from Ser-L223 upon forming the semiquinone (Q_B^-*) in reaction centers from *Rhodobacter sphaeroides*. *Biochemistry 46*, 8234-8243.
25. Wells, T. A., Takahashi, E., and Wraight, C. A. (2003) Primary quinone (Q_A) binding site of bacterial photosynthetic reaction centers: mutations at residue M265 probed by FTIR spectroscopy. *Biochemistry 42*, 4064-4074.
26. Rinyu, L., Martin, E. W., Takahashi, E., Maróti, P., and Wraight, C. A. (2004) Modulation of the free energy of the primary quinone acceptor (Q_A) in reaction centers from *Rhodobacter sphaeroides*: contributions from the protein and protein-lipid(cardiolipin) interactions. *Biochim. Biophys. Acta 1655*, 93-101.
27. McComb, J. C., Stein, R. R., and Wraight, C. A. (1990) Investigations on the influence of headgroup substitution and isoprene side-chain length in the function of primary and secondary quinones of bacterial reaction centers. *Biochim. Biophys. Acta 1015*, 156-171.
28. Michel-Beyerle, M. E., Plato, M., Deisenhofer, J., Michel, H., Bixon, M., and Jortner, J. (1988) Unidirectionality of charge separation in reaction centers of photosynthetic bacteria. *Biochim. Biophys. Acta 932*, 52-70.
29. Dutton, L. P. (1978) Redox Potentiometry: Determination of Midpoint Potentials of Oxidation-Reduction Components of Biological Electron Transfer Systems. *Methods in Enzymology LIV*, 411-435.
30. Prince, R. C., Dutton, L. P., and Bruce, J. M. (1983) Electrochemistry of ubiquinones Menaquinones and plastoquinones in aprotic solvents. *FEBS 160*, 273-276.
31. Breton, J., Boullais, C., Burie, J.-R., Nabedryk, E., and Mioskowski, C. (1994) Binding sites of quinones in photosynthetic bacterial reaction centers investigated by light-induced FTIR difference spectroscopy: assignment of the interactions of each carbonyl of Q_A in *Rhodobacter sphaeroides* using site-specific ^{13}C-labeled ubiquinone. *Biochemistry 33*, 14378-14386.
32. Mulkidjanian, A. Y., Kozlova, M. A., and Cherepanov, D. A. (2005) Ubiquinone reduction in the photosynthetic reaction centre of *Rhodobacter sphaeroides*: interplay between electron transfer, proton binding and flips of the quinone ring. *Biochem. Soc. Trans. 33*, 845-850.
33. Kleinfeld, D., Okamura, M. Y., and Feher, G. (1984) Electron transfer in reaction centers of *Rhodopseudomonas sphaeroides*. I. Determination of the charge recombination pathway of $D^+Q_AQ_B^-$ and free energy and kinetic relations between $Q_A^-Q_B$ and $Q_AQ_B^-$. *Biochim. Biophys. Acta 766*, 126-140.
34. Paddock, M., McPherson, P., Feher, G., and Okamura, M. (1990) Pathway of proton transfer in bacterial reaction centers: replacement of serine-L223 by alanine inhibits electron and proton transfers associated with reduction of quinone to dihydroquinone. *Proc. Natl. Acad. Sci. USA 87*, 6803-6807.
35. M. L. Paddock, G. F., M. Y. Okamura. (1995) Pathway of proton transfer in bacterial reaction centers: furtherinvestigations on the role of Ser-L223 studied by site-directed mutagenesis. *Biochemistry 34*, 15742-15750.

36. Paddock, M. L., Isaacson, R. A., Abresch, E. C., and Okamura, M. Y. (2007) Light induced EPR spectra of reaction centers from *Rhodobacter sphaeroides* at 80K: Evidence for reduction of Q_B by B-branch electron transfer in native reaction centers. *Appl. Magn. Reson. 31*, 29-43.
37. Deisenhofer, J., and Norris, J. R. (1993) *The Photosynthetic Reaction Center* Vol. 2, Academic Press Inc, San Diego.
38. Wraight, C. A. (1979) Electron acceptors of bacterial photosynthetic reaction centers II. H^+ binding coupled to secondary electron transfer in the quinone acceptor complex, *Biochim. Biophys. Acta 548*, 309-327.
39. Wraight, C. A., Cogdell, R. J., and Clayton, R. K. (1975) Some experiments on the primary electron acceptor in reaction centres from *Rhodopseudomonas sphaeroides*. *Biochim. Biophys. Acta 396*, 242-249.
40. Deisenhofer, J., and Michel, H. (1989) The photosynthetic reaction center from the purple bacterium *Rhodopseudomonas viridis*. *Science 245*, 1463-1473.
41. Feher, G. (1971) Some chemical and physical properties of a bacterial reaction center particle and its primary photochemical reactants. *Photochem. Photobiol. 14*, 373-387.
42. Okamura, M. Y., Paddock, M. L., Graige, M. S., and Feher, G. (2000) Proton and electron transfer in bacterial reaction centers. *Biochim. Biophys. Acta 1458*, 148-163.

Figures

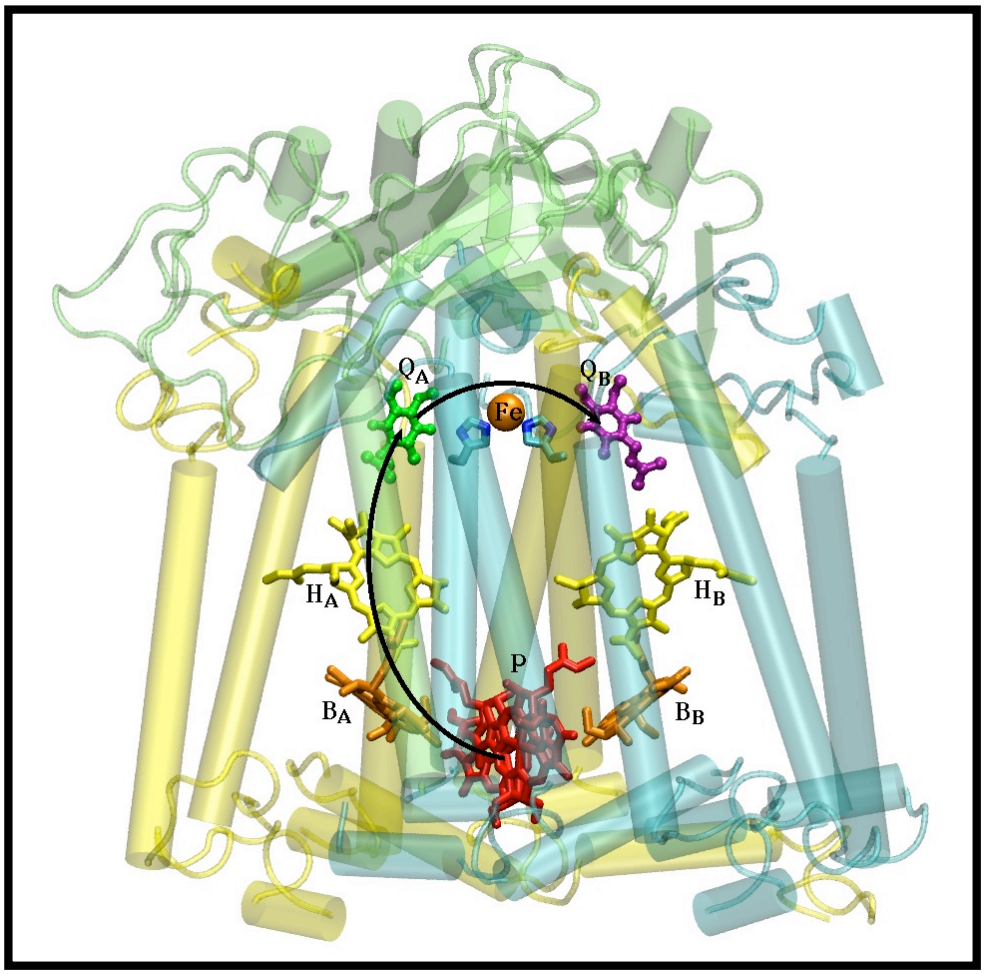

Figure 1.1. The structure of the reaction center from *Rba. sphaeroides* with the L, M and H subunits shown in yellow, blue and green respectively. The active cofactors including the primary donor (P), a dimer of bacteriochlorophyll, bacteriochlorophyll monomers (B), bacteriopheophytins (H) and ubiquinones (Q), are all labeled with subscripts indicating the A or B branch. The non-heme Fe^{2+} is also labeled and two of its histidine ligands (L190 and M219) are shown but not labeled. (from Wraight and Gunner, 2009 (3))

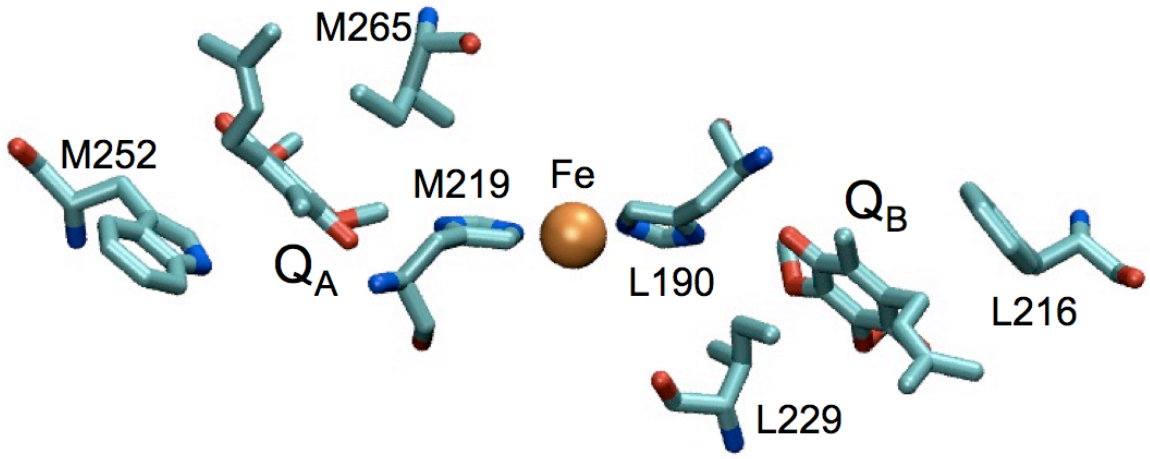

Figure 1.2. Q_A and Q_B are shown located symmetrically around the non-heme Fe^{2+}. The O4 carbonyl of each quinone is hydrogen bonded to a Fe-coordinated histidine. On either side of the quinone plane, bulky residues are in VDW contact with the headgroup. (Prepared from structure: 1AIG.pdb)

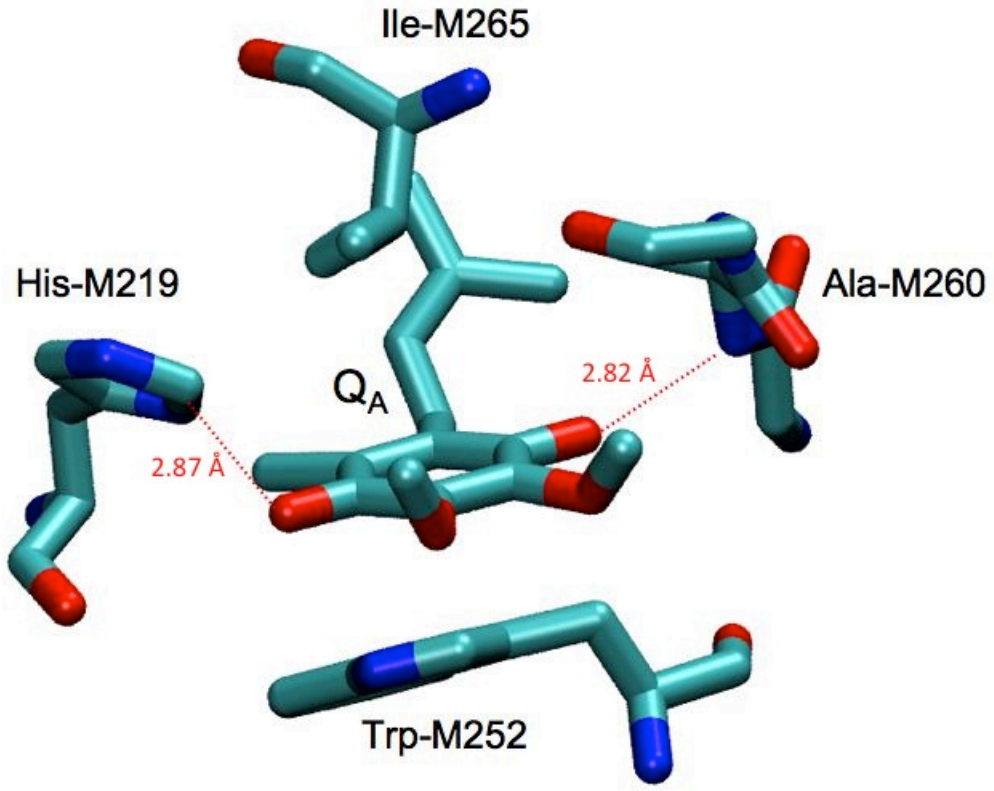

Figure 1.3. The Q_A site showing the quinone and four residues of known importance to quinone binding and function. His-M219 and Ala-M260 form H-bonds with the O4 and O1 carbonyls, respectively. Trp-M252 and Ile-M265 are on opposite sides of the quinone and in van der Waals contact. Mutations to these residues have shown their importance to quinone binding affinity and redox tuning. (from structure 1AIG.pdb

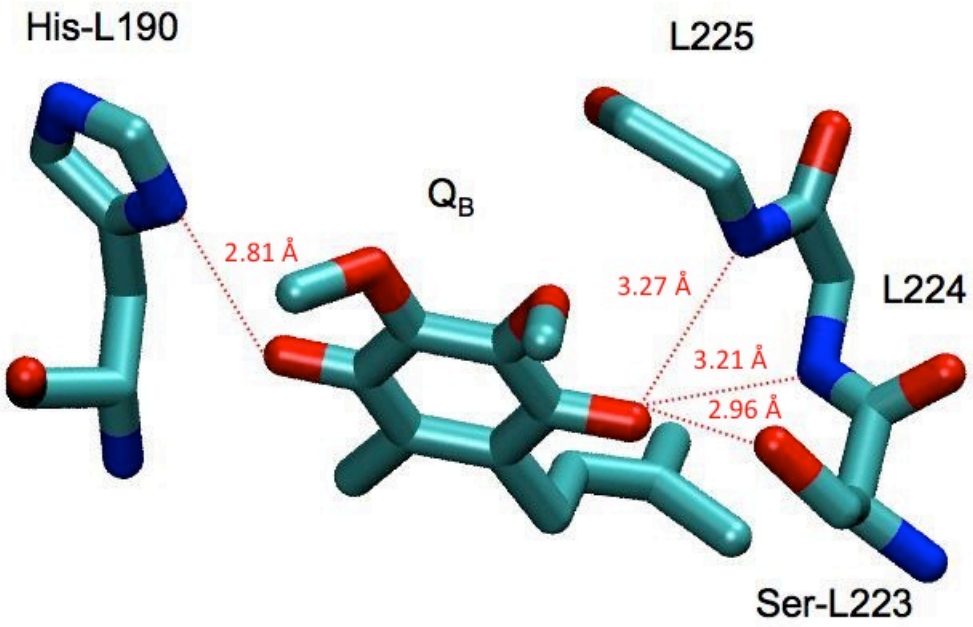

Figure 1.4. The Q_B binding site with the quinone and 4 potential H-bonding partners. His-L190 is certain to form a strong H-bond at the O4 carbonyl. However, the H-bonding structure at O1 is more ambiguous and likely contains contributions from Ser-L223, Ile-L224 and Gly-L225. (from structure 1DV3.pdb)

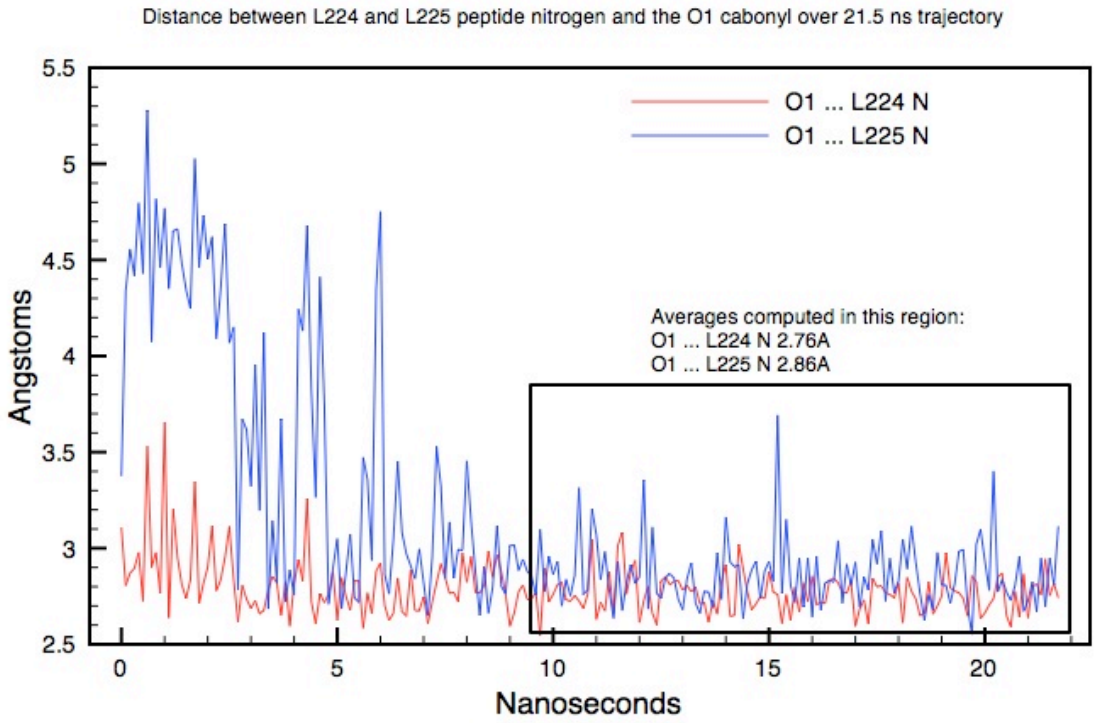

Figure 1.5. Heavy atom distances between the Q_B O1 carbonyl and the backbone, amide nitrogens from both L224 and L225 over the course of a MD trajectory. After approximately 1 ns the distances "stabilize" and the averages shown were computed from the rest of the trajectory.

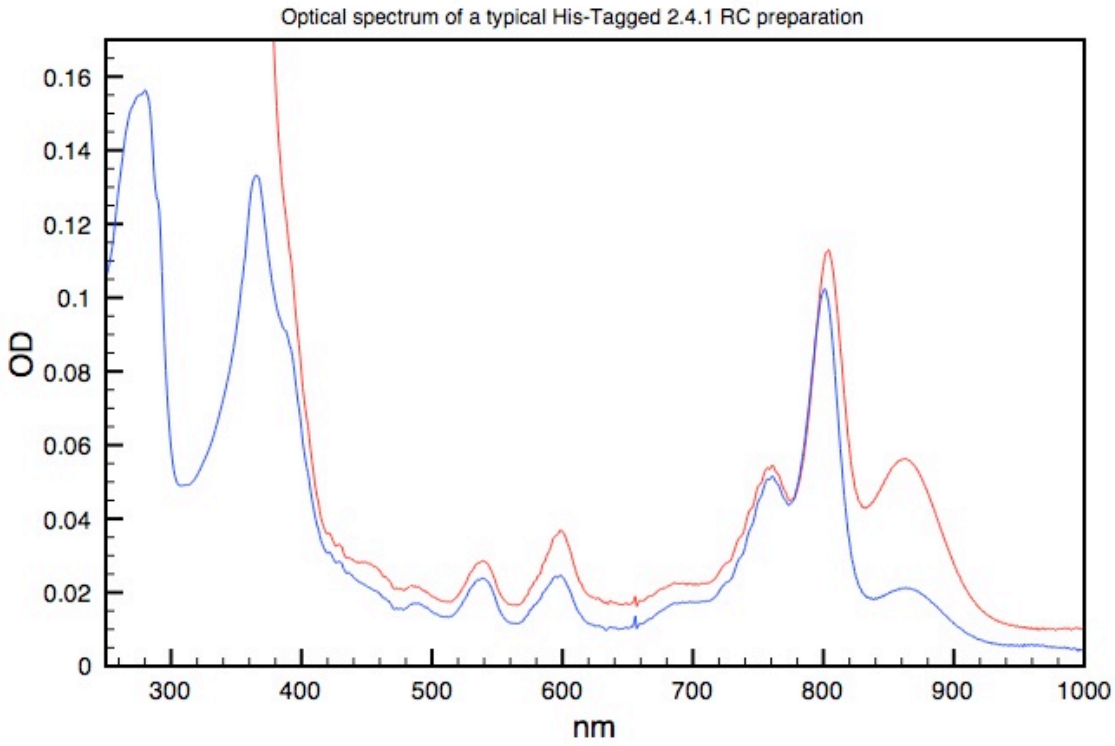

Figure 1.6. The optical spectrum of a typical RC fraction after purification. The 755 nm peak is ~50% of the 802 nm peak. The 860 nm peak in the blue trace shows the bleaching that is often observed due to light activation from the measuring beam. The red trace shows the spectrum with dithionite added to fully reduce the sample.

Chapter 2:

Cell Growth and Isolation and Preparation of Photosynthetic Reaction Centers

Abstract

The steps involved in obtaining the material for EPR samples are described in Chapter 2. *Rba. sphaeroides* strains that can be grown phototropically and strains that require semi-aerobic growth are both used for the experiments in this thesis. These cell types are described along with their growth conditions and reaction center isolation procedures. The steps to biosynthetically replace the native ferrous Fe with Zn are also explained. Finally, the tests for function and metal exchange efficiency are outlined here.

Introduction

Obtaining high quality information about the binding sites of both Q_A and Q_B in the photosynthetic RC hinges on the quality of the prepared samples. While the details of generating the desired semiquinone species in EPR sample tubes are discussed in the following chapters, the methods of cell growth and preparation of RCs also contribute to the quality of the final sample. Methods of cell growth and RC isolation have been well documented. (*1-3*) The challenge in creating samples is integrating established processes with small modifications to maximize yield and quality of our specific RCs. This chapter will outline the basic mode of bacteria growth, which required some modifications to accommodate isotopic labeling. RC isolation was greatly simplified by using His-tagged proteins and required only small optimization from existing procedures for the metal exchange. (*4*)

Removal of the native high spin Fe^{2+} is required to observe the signal from the RC semiquinones. The fact that in the native RCs the semiquinone signal is coupled to the Fe has been known for nearly forty years and metal exchange procedures have been evolving for almost as long. (*5-8*) The procedures here are principally from the work of Utschig et al. (*7*) with minor modifications to concentrations and exact methodology. Metal exchange has proved to be highly sensitive to small, idiosyncratic aspects of the actual process that were not mentioned in published procedures, but are outlined in this chapter.

Cell Growth and RC Isolation

All reaction centers used in these studies were expressed in *Rba sphaeroides*. However, even when referring to so-called "wild type" RCs, they were expressed in bacteria with some mutations. Depending on the particular mutation, the mode of bacteria growth varied between anaerobic, semiaerobic and aerobic conditions. In all cases, the basis of the growth medium was Sistrom's minimal medium but with malate used as the carbon source, in place of succinate. (*9*)

RCs referred to as "wild type" in these studies are from the 2.4.1 strain with a polyhistidine tag inserted at the C-terminus of the M-subunit. (*4*) The gene encoding the M subunit, *pufM*, was cloned into the phage plasmid M13 and histidine codons were inserted via the oligonucleotide insertion method. (*2, 10*) The *puf* operon was reassembled in a pRK plasmid and inserted into a strain of 2.4.1, in which the *pufL* and *pufM* genes on the chromosome were deleted, called ΔLM1.1. (*4*) The plasmid carrying the RC also contained the gene for tetracycline resistance. These cells were grown in malate Sistrom's medium containing 2 μg/ml of tetracycline in 1 liter bottles covered with red filters (to protect tetracycline from photodegradation). The cells were grown photosynthetically and anaerobically under an array of 40 watt incandescent light bulbs. For large-scale growth, the 1 liter stock is transferred to 12 liter carboys containing no antibiotic. When inoculated with this concentration of cells, there were few contamination issues in the final cell harvest.

This work also includes RCs with site specific mutations to the L and M subunits. The pRK plasmid containing these mutations was transferred into a *Rba. sphaeroides* background containing no light harvesting complex (courtesy of Dr. E. Takahashi). These

cells grow very inefficiently under photosynthetic conditions, as used for the His-tagged 2.4.1 strain. However, *Rba. sphaeroides* is also capable of growing aerobically in the absence of light and these mutants were grown in Sistrom's medium supplemented with yeast extract, shaking, in the dark. Pigmentation in *Rba. sphaeroides*, including RC biosynthesis, is under oxygen control and can be induced under semi-aerobic conditions. Initially, therefore, 450 ml of Sistrom's medium supplemented with 0.1% yeast extract was inoculated with cell stock. At the mid logarithmic growth stage, (typically ~3 days after initial inoculation) an additional 1 liter of Sistrom's medium supplemented with 0.6% yeast extract was added to the flasks and, the rate of shaking was reduced from 300 rpm by increments of ~50 rpm daily to a final rate of ~100 rpm, to maximize RC expression. Strains of *Rba. sphaeroides* containing RC mutations carried a resistance to both tetracycline and kanamycin. The Sistrom's medium typically contained both antibiotics (tetracycline at 2 μg/ml and kanamycin at 25 μg/ml) at the initial stage of growth, but only tetracycline was present in the additional 1 liter of medium.

Obtaining uniformly ^{15}N labeled RCs was achieved by using ^{15}N labeled ammonium sulfate, the only significant nitrogen source in Sistrom's medium (Cambridge Isotopes, catalog number: NLM-713). In the case of the His-tagged 2.4.1 strain, there was no need to change the growth conditions beyond using isotopically labeled Sistrom's medium. However, due to the cost of labeled ammonium sulfate, the bacteria were typically grown in multiple 1 liter bottles instead of 12 liter carboys. This allowed for growth with tetracycline under red filters and kept any contamination isolated in single 1 liter bottles.

Mutations expressed in the strain lacking light harvesting complex were normally grown in medium supplemented with yeast extract, which is a significant source of nitrogen (similar in scale to ammonium sulfate). If this medium were used for ^{15}N enrichment, the yeast extract would cause a significant, ~50%, isotope dilution. It was determined that, albeit at lower yield (2.3 grams of material per liter as opposed to 3-4.6g in yeast extract semi-aerobic growth) and slower rate, the cells could be grown in Sistrom's medium without yeast extract. In this type of growth, there was no apparent advantage in starting the culture in an aerobic environment with 450 ml of medium and adding an additional liter at the logarithmic growth stage. The greatest yield of cells per liter of material was obtained from inoculating flasks containing 1200 ml of ^{15}N labeled Sistrom's medium with both antibiotics tetracycline and kanamycin.

When it appeared that the cultures had reached a maximum density (estimated from the color) the cells were harvested from the carboys, bottles or flasks by a combination of filtration and centrifugation. The His-tagged 2.4.1 strain, grown phototrophically in bottles or carboys, typically contained very few large particulates and most of the liquid medium could be easily removed by filtration. The cells could then be collected by centrifugation at 8000 rpm in 250 ml bottles. However, semi-aerobic growth would sometimes generate a large amount of precipitate that could clog the filter. Additionally, there was always some risk of cell loss when concentrating by filtration. Therefore, despite the cost in time, it was prudent to collect these cells exclusively by centrifugation.

The RCs were isolated in more or less the same manner for the His-tagged 2.4.1 strain and for mutants lacking the light harvesting complex and the vast majority of work

in the following chapters used RCs containing a poly-histidine tag.[1] The basic method has been previously outlined (*4*), and the initial steps in RC isolation are very similar to the isolation of RCs lacking the poly-histidine tag. (*3*)

Regardless of whether cells were frozen post collection or used immediately, the cell pellets were combined with buffer containing 100 mM NaCl, 10 mM Tris at pH 7.9, and 50 μM EDTA (NET buffer), and stirred at 4 °C overnight. The buffer maintains ionic strength and chelates divalent ions, thereby inhibiting some protease activity. Cells were washed and recollected via centrifugation two times (or more if the supernatant is still very cloudy). Following the final wash, cells were suspended in a volume of NET buffer at ~0.5 g/ml, and were broken by passage through a French press at 18,000 psi. To maximize the yield of breakage, the suspension was routinely run through the French press twice. Unbroken cells were separated by centrifugation at 15,000 rpm for 20 minutes. If the quantity of unbroken cells was substantial, the pellet was resuspended in NET buffer and French pressed again.

The result of crushing cells in the French press is the formation of chromatophores. These are small vesicles reformed after disruption of the cell membrane folds that contain the RCs and other membrane proteins. In the isolation of RCs that do not contain the poly-his tag, the chromatophores would be purified by centrifugation to remove some soluble proteins. However, this step is not required for His-tagged RCs and the membrane proteins were immediately solubilized by addition of the detergent lauryldimethylamine-N-oxide (LDAO). In order to maximize the efficiency of detergent

[1] While the data presented in this thesis are nearly exclusively from His-tagged RCs, all methods were also tested with the wild type "Ga" or carotenoidless strain "R26". All RCs showed similar spectroscopic properties and His-tagged RCs were routinely used due to the simplicity of isolation.

solubilization, the broken cells were diluted in NET buffer prior to the addition of 1% LDAO. The degree of dilution is somewhat arbitrary but, for a typical preparation with less than 100 g of starting material, the total volume was increased to 290 ml buffer, which conveniently fits into twelve 25 ml ultracentrifuge tubes after the addition of 10 ml of LDAO (1% total LDAO from 30% stock). Because of the selectivity of the His-tag, there was no need to take care to not over solubilize the membranes with detergent, as in previously published procedures. To ensure maximum solubilization, the suspension was stirred at room temperature for one hour in NET buffer with 1% LDAO. Solubilized proteins were separated from insoluble proteins and aggregates by centrifugation at 40,000 rpm for 90 minutes – solubilized RCs were in the supernatant.

After solubilization, the His-tag was used to purify the RCs. The supernatant following 40,000 rpm centrifugation (approximately 250 ml for a prep smaller than 100 g) was diluted to a total volume of 500 ml in buffer containing 100 mM NaCl, 10 mM Tris at pH 7.9, 10 μM EDTA, 0.045% LDAO, and 4 mM imidazole (TL045 + 4 mM imidazole). This solution was loaded onto a column of Ni-NTA (Qiagen) resin at a rate as slow as could be generated with the valve on the gravity-fed column, typically taking up to 12 hours (overnight), in order to get the majority of His-tagged protein to adhere to the nickel column.

Washing the Ni-NTA column with approximately 500 ml of TL045 buffer provided the best compromise between removing as much unwanted cell residue and protein from the column as possible, yet preventing RCs from leaking off the column or any denaturation. The RCs were removed from the Ni-NTA column with an elution buffer comprised of TL045 and 150 mM imidazole. In order to ensure that the RCs are

eluted from the column at the highest possible concentration, the flow rate was set as slow as was manageable in the gravity fed column.

5 ml fractions were collected from the column and assayed for RC concentration. RC concentration is based on the extinction coefficient at 802 nm of 0.288 μM^{-1} cm^{-1}. A typical 2.4.1 RC isolation, starting with 100 g of cells, yields at least two 5 ml fractions with a concentration of ~50μM. The yield of high concentration fractions from mutant RCs grown semi-aerobically was highly variable, but seemed to correlate to the quantity of RCs expressed during cell growth. It was very unlikely to produce a single high concentration 5 ml fraction in preparations starting with less than 50 g of cells. Purity of the RCs was assayed via the ratio of the 802 nm absorption versus the typical tryptophan 280 nm protein absorption. (*11*) A 280:802 ratio of approximately 1.2 is considered to be very pure. However, for samples destined for EPR, 280:802 ratios closer to 1.4-1.6 have been shown to produce better samples (personal communication from Lisa Utschig, ANL). The reason for this is unclear, but it is possible that extensive purification of RCs removes lipids from the sample that stabilize the RC throughout the chaotropic metal exchange procedure.

RC Metal Exchange

For EPR studies of the RC semiquinones it is necessary to remove the native high spin iron (Fe^{2+}, S=2) in order to see the narrow, approximately g=2.004, EPR signal attributable to semiquinones Q_A^- and Q_B^-. It has previously been shown that replacing Fe^{2+} with diamagnetic divalent cations yields RCs with essentially no change in kinetics and function. (*7, 12*) Zn^{2+} is widely used to replace Fe^{2+} in samples used for EPR

spectroscopy due to its EPR inactivity (as opposed to Cu^{2+} that restores wild type kinetics but introduces an EPR signal near g=2). (*12-14*) Early preparations focused on complicated biochemical processes and recognized that detergent type and concentration were an important factor in the effective replacement of Fe^{2+}.(*6*) Procedures where the LDAO concentration was left unchanged, through RC isolation to the metal exchange, resulted in significant loss of the H subunit and required protein reconstitution, unnecessarily complicating the preparation and resulting in low yield. (*12*) Refinements in metal exchange procedures attempted to combat this problem by replacing LDAO with other detergents such as sodium cholate. However, the extensive dialysis procedures described by Debus et al. (*12*) were later shown by Utschig et al. (*7*) to leave a substantial amount of LDAO associated in micelles around the RCs. The resulting conclusion was that an efficient metal exchange required low LDAO concentration, below the CMC, but no exchange of detergent.

In addition to the biochemical procedures, Zn RCs have been made biosynthetically, but these preparations have complications that limit their usefulness. Wild type RCs grown in a medium with high Zn concentration and minimal Fe showed incorporation of Zn so low they were not sufficient for most EPR experiments. An attempt was made to increase Zn incorporation by mutating the Fe ligand His-M266 to Cys.(*8*) While this mutation increased Zn content in RCs (up to ~20%), there are clear indications that the EPR properties of the semiquinones are significantly altered. (*8, 15, 16*) Thus, the M266HC mutant does not seem like a good source for metal exchanged RCs.

RCs for EPR experiments have been isolated from a wide variety of cell types. The procedures of Utschig et al. were tested using RCs from the carotenoidless R26 strain as well as the Ga strain, isolated by well established protocols. (*3*) More recently, all RCs have contained a poly-his tag and were isolated according to Ni-NTA chromatography. (*4*) Published metal exchange procedures were successfully refined using His-tagged RCs from the 2.4.1 strain.

An essential element for good metal exchange is maintaining a low detergent concentration. In protein isolation procedures for both His-tagged and "standard" RC, the LDAO concentration is ~1% immediately after solubilization. In "standard" preparations, the isolation procedure of Takahashi et. al. (*2*) was modified by limiting ammonium sulfate (AS) precipitation to one precipitation with 0.27 g/ml AS. The RCs form a floating aggregate referred to as the "levitate". These RCs are suspended in buffer containing no AS and 0.045% LDAO. RCs were placed in a 10:20:30:40% sucrose step gradient and centrifuged at 40,000 rpm over night. The RCs accumulated in the 20% step of the gradient and were pipetted out. All these steps affect the micelle structure or solubility of the RCs. The LDAO concentration was certainly close to 0.045%, and below the 0.051% CMC, prior to the standard anion exchange (DEAE) chromatography step. (*2*)

For His-tagged RC preparations, the yield from metal exchange was always quite good and RCs retained the H subunit. This implies that the 500 ml wash on the Ni-NTA column was sufficient to reduce the LDAO concentration below the CMC. RCs should be removed from the column at as high a concentration possible. High concentration fractions were obtained by nearly saturating the column with material and eluting as

slowly as possible. In order to achieve a good (~70%) yield from the metal exchange, RCs are ideally removed from the column at OD_{802} 12-20 (~50-70μM). Metal exchange procedures were best performed on RCs immediately after removal from the column, and at OD_{802} 18-20. Using previously frozen RCs resulted in very low yield.

It has been reported that centrifugal concentration of RCs results in low metal exchange yield and loss of the H subunit. (*7*) It was presumed that along with protein concentration the centrifugal filter also concentrates LDAO beyond levels where metal exchange can be successful. In M265IT, L223SA and ^{15}N labeled 2.4.1 RCs, where there is less starting material, it is often impossible to remove RCs from the Ni-NTA column at high enough concentrations to perform metal exchange. In order to circumvent the problems reported with concentrating RCs, a method of dilution and reconcentration was employed. The starting material was diluted with buffer containing no detergent by the same degree as the RCs need to be concentrated. (i.e., OD 9 RCs would be diluted 2x with buffer, then concentrated to OD 18) Additionally, centrifugal concentration was done at very low speeds, ~2000x g. Starting with low concentration samples, this procedure provides adequate (~50%) recovery from metal exchange and, more importantly, with H-subunit retention after centrifugal concentration. It also allows for the use of low concentration fractions that typically would be discarded in wild type preparations.

At the start of the metal exchange procedure, the RC buffer contains 10 mM Tris at pH 7.9, 10 μM EDTA, 100 mM NaCl, up to 150 mM imidazole (0 mM in non-His tagged preps) and 0.045% LDAO. One ~5 ml fraction from the Ni-NTA or DEAE column, at OD_{802} between 12 and 20, was brought to room temperature, the Tris

concentration was raised to 20 mM, and 3 equivalents of ubiquinone-10 (from 2 mM stock dissolved in 1% LDAO) and 5 mM o-phenanthroline (from a 150 mM stock in 50% EtOH) were added. The increase in buffer concentration stabilizes the pH when LiSCN is added at high concentrations in the next step. Adding an excess of ubiquinone-10 maintains occupancy of the Q_A site through the chaotropic treatments. O-phenanthroline is a chaotrope that disrupts the three-dimensional structure of the RC, and it needs to be introduced separately from LiSCN and at room temperature to ensure it is completely soluble.

The RC solution containing o-phenanthroline was incubated for 5 minutes at room temperature followed by addition of LiSCN to a concentration of 1.5 M.[2,3] Typically the LiSCN was added in aliquots of less than 1 mL and was rapidly mixed after each addition to minimize local concentration effects. The solution was incubated for 30 minutes on ice. LiSCN is a chaotrope and loosens the RC structure. Additionally, SCN^- binds the native Fe, creating Fe-thiocyanate complexes - serving the dual role of allowing for the removal of Fe from its His ligands and sequestering the Fe to prevent reincorporation.

After incubation, 1 mM $ZnSO_4$ and 8 mM 2-mercaptoethanol were added. The addition of Zn, which is incorporated into the Fe site, often resulted in some cloudiness

[2] If there is difficulty obtaining a reasonable yield with a particular RC species, this concentration can be decreased to as low as ~900 mM. However, this is coupled with a decrease in efficacy of the Fe replacement.

[3] LiSCN concentration can't be adequately judged by weight alone due, to unknown water content. In order to get the best possible measurement of concentration, LiSCN is dehydrated in a vacuum oven for 24 hours at 110 °C. This material is then used to create a stock at ~4 M. Samples from this stock are diluted 1000x and submitted for ICP analysis. Routinely, the actual concentration of these samples is measured to be 3.2-3.5 M.

that dissipated after mixing. The 2-mercaptoethanol is thought to assist in Zn incorporation. If there is difficulty in getting adequate Zn incorporation, the quantity of 2-mercaptoethanol can be varied between 0-10 mM. (Lisa Utschig, ANL, personal communication). 2-mercaptoethanol concentrations were adjusted in Ga and R26 type RCs, but only 8 mM was used with His-tagged 2.4.1 and His-tagged mutant RCs. The resulting solution was incubated on ice for 30 minutes and was then dialyzed against 2 L of TL045 buffer with 20 g Chelex-100 resin (Biorad #143-2832). Chelex-100 is a cation exchange chromatography resin, used here to chelate remaining unincorporated Zn and Fe. Regardless of sample volume, 1 cm wide dialysis tubing was used. Wider tubing decreased RC yield and the efficiency of metal exchange. The reason for this is unclear, but it is suspected that the greater surface area to volume of smaller diameter tubes increases the rate of equilibration between the inside and outside of the tubing. After 48 hours of dialysis, including 3 buffer changes, the RCs were separated from precipitate by centrifugation at 12000 rpm for 15 minutes. The precipitate should be pink in color indicating successful Fe removal.

RC Sample Analysis

The pigments present in RCs make UV and visible light spectroscopy useful in analyzing isolated and metal exchanged RCs. RCs from *Rba. sphaeroides* have three characteristic peaks between 700 and 900 nm due to light absorption by the bacteriopheophytin and bacteriochlorophyll. (See Chapter 1). The peak at 860 nm is readily bleached and largely disappears when the primary donor is oxidized. A reducing agent such as Na-dithionite, ascorbate or ferrocene can be added to the cuvette to reduce

P and maximize intensity at 860 nm. The 802 nm peak is routinely used to measure the concentration of RC samples and the ratio of this peak to the peak at 280 nm (tryptophan absorption) is used to determine RC purity. However, the three peaks must be viewed as a whole. Free bacteriochlorophyll dissociated from light harvesting complex or degraded RCs can contaminate the 755 and 802 nm peaks causing them to be artificially high, and intact light harvesting complexes can distort the 802 and 860 nm peaks If the ratio of peak intensities isn't correct, it is likely the concentration and purity calculated from the intensity of the 802 nm peak will be inaccurate. (*11*) It is also possible to obtain information about the degree of Zn incorporation after metal exchange. RCs that lack a divalent ion in the Fe site show an ~15 nm blue shift in the long wavelength bacteriochlorophyll dimer peak. (*7*) Spectra of RCs after successful metal exchange show virtually no difference from wild type.[4]

The X-band cw-EPR signal in the region of g=2 is indicative of semiquinones and is used to judge the decoupling of semiquinones from Fe. EPR samples can be generated by reducing the RC sample with ~8-10 mM Na-dithinonite, resulting in a symmetric signal from Q_A^-, theoretically located at g=2.0046 with a linewidth of approximately 8.5 Gauss. Unfortunately, this signal can be easily confused with background radicals in the sample or even in the cavity. If the semiquinone radical is generated by photo-reduction, a characteristic signal that is the sum of the P^+ cation and the semiquinone, centered at g=2.0037, appears in the spectrum. The signal shows asymmetry between the two peaks, more intense at lower field. (Figure 2.1) In order to generate the light induced signal,

[4] Despite the identical location of the UV/Vis peaks, it is often the case that metal exchange procedures result in a small amount of irreversible bleaching of the 860 nm peak. This bleaching showed little impact on the function of working RCs.

light from a 25 V actinic source was focused onto a plexiglass lightguide abutted to the cavity window.

Isothermal coupled plasma spectroscopy (ICP) analysis can provide accurate measurement of the metal content in RC samples. ICP samples were submitted for analysis to both the School of Chemical Sciences microanalysis lab and Illinois Sustainable Technology Center (formerly Waste Management Resource Center), and results were typically quite similar. Samples were diluted to 1 μM RC in 20 ml of distilled H_2O for submission for analysis. For stochiometric ratios of 1 Fe or 1 Zn per RC, it is expected that results of 56 ng/ml and 66 ng/ml will be obtained, respectively. Previous results indicate that a ratio of ~2 Zn per RC is not atypical. Unfortunately, detection limits for Fe are at ~5 ng/ml and an Fe concentration of zero will give a result of only <10 ng/ml. All high quality metal exchanged RCs showed Fe levels below this detection limit.

Retention of the H subunit is a serious concern when performing metal exchange procedures. Running metal exchanged samples on an SDS PAGE gel shows whether or not the protocol substantially retains the H subunit. In order to get good quality results on a PAGE gel, the following 5x sample buffer was used: 18% SDS w/v, 180 mM Tris at pH 7.8, 0.05% bromphenol blue, 1.8 M urea and 20% glycerol. As the name suggests, this buffer is a stock designed to be diluted 5 fold in the sample. Samples for SDS PAGE are generated by calculating the quantity of RC stock to yield ~12 μg of RCs. The gels used were pre-poured 10% gels (BioRad #161-1155) and held ~50 μl of sample per lane. Gels were typically run at ~250 V using a BioRad Mini PROTEAN 3 assembly (BioRad #525BR). For these, 10 μl of the 5x sample buffer is used. The remaining 40 μl consist

of a combination of RC stock and distilled H_2O. Prior to loading on the gel, the samples are incubated at 37 °C for 30 minutes to ensure the RCs are completely dissolved in SDS. The SDS PAGE gels were stained with "Imperial Protein Stain" (Thermo Scientific, catalog #24165), using the manufacturer's procedures. Complete RCs should have three bands (H, M and L subunits) that compare in size and relative intensity to wild type controls.

Measuring the rate of the $P^+Q^- \rightarrow PQ$ back reaction (Figure 2.2) can provide insight into the kinetics and relative energetics of the acceptor quinones in the RC. The rate of this reaction reflects the equilibrium between Q_A^- and Q_B^- and changes in the measured rate can be related to changes in the free energy difference between the two quinones. Since the metal exchanged RCs are meant to be identical to the wild type, it is important to see that the charge recombination rates are similar. The back reaction is measured by flash spectroscopy at 430 nm and the rate is expected to be on the order of 1 s^{-1} for RCs with active Q_B vs. 0.1 s for RCs with Q_A only. Analysis of the kinetics is done by fitting the trace to a biexponential decay. The fast component is attributable to relaxation of $P^+Q_A^-$ in RCs lacking Q_B activity. Introducing an inhibitor (e.g., 100 μM turbutryn) to block electron transfer to Q_B reveals this component. Figure 2.2 shows a typical measurement. These samples show a back reaction rate on the order of 1.3 sec^{-1}, which is in reasonable agreement with wild type.

Discussion

RCs from numerous strains are now routinely isolated and metal exchanged, and the necessary growth and isolation procedures are reasonably well established. Metal

exchange procedures, however, are somewhat more dynamic. While exact concentrations are given for every step, it is often necessary to adjust the quantities at nearly every step. There appears to be no distinct set of rules as to how this is best accomplished, but, generally speaking, the closer a particular reaction center is to the "wild type" construction, the greater the concentration of chaotropes required. Using too low a concentration will result in incomplete Fe removal, and concentrations that are too high will quickly diminish yield and produce high concentrations of free bacteriochlorophyll resulting from denatured RCs. In addition to reagent concentration, several, seemingly arbitrary details make a significant difference. For example, metal exchange is far more efficient when the reactions are performed in a tall skinny tube; similarly dialysis is always done in 1 cm diameter tubing in a tall cylinder. All of these features speak to the lack of complete understanding of the mechanisms involved in the metal exchange process. However, when a defined set of conditions is established to work for a particular RC species, these conditions have always been repeatable.

References

1. Feher, G., and Okamura, M. Y. (1978) Chemical composition an properties of reaction centers, In *The Photosynthetic Bacteria* (Clayton, R. K., and Sistrom, W. R., Eds.), pp 349-386, Plenum, New York.
2. Takahashi, E., Maroti, P., and Wraight, C. A. (1990) In *Current Research in Photosynthesis* (Baltscheffsky, M., Ed.), pp 169-172, Kluwer Academic Publishers, Boston.
3. Takahashi, E., and Wraight, C. A. (1992) Proton and electron transfer in the acceptor quinone complex of *Rhodobacter sphaeroides* reaction centers: characterization of site-directed mutants of the two ionizable residues, Glu^{L212} and Asp^{L213}, in the Q_B binding site, *Biochemistry 31*, 855-866.
4. Goldsmith, J. O., and Boxer, S. G. (1996) Rapid isolation of bacterial photosynthetic reaction centers with an engineered poly-histidine tag, *Biochim. Biophys. Acta 1276*, 171-175.
5. Dutton, P. L., Leigh Jr, J. S., and Reed, D. W. (1973) Primary events in the photosynthetic reaction centre from *Rhodopseudomonas spheroides* strain R26: Triplet and oxidized states of bacteriochlorophyll and the identification of the primary electron acceptor, *Biochim. Biophys. Acta 292*, 654-664.
6. Tiede, D. M., and Dutton, P. L. (1981) Orientation of the primary quinone of bacterial photosynthetic reaction centers contined in chromatophore and reconstituted membranes, *Biochim. Biophys. Acta 637*, 278-290.
7. Utschig, L. M., Greenfield, S. R., Tang, J., Laible, P. D., and Thurnauer, M. C. (1997) Influence of iron-removal procedures on sequential electron transfer in photosynthetic bacterial reaction centers studied by transient EPR spectroscopy, *Biochemistry 36*, 8548-8558.
8. Lubitz, W., and Feher, G. (1999) The primary and secondary acceptors in bacterial photosynthesis III. Characterization of the quinone radicals Q_A^- and Q_B^- by EPR and ENDOR, *Appl. Magn. Reson. 17*, 1-48.
9. Sistrom, W. R. (1960) A requirement for sodium in the growth of *Rhodoseudomonas spheroides*, *J. Gen. Microbiol. 22*, 778-785.
10. Williams, J. C., Alden, R. G., Murchison, H. A., Peloquin, J. M., Woodbury, N. W., and Allen, J. P. (1992) Effects of mutations near the bacteriochlorophylls in reaction centers from *Rhodobacter sphaeroides*, *Biochemistry 31*, 11029-11037.
11. Deisenhofer, J., and Norris, J. R. (1993) *The Photosynthetic Reaction Center* Vol. 2, Academic Press Inc, San Diego.
12. Debus, R. J., Feher, G., and Okamura, M. Y. (1986) Iron-depleted reaction centers from Rhodopseudomonas sphaeroides R-26.1: characterization and reconstitution with Fe^{2+}, Mn^{2+}, Co^{2+}, Ni^{2+}, Cu^{2+}, and Zn^{2+}, *Biochemistry 25*, 2276-2287.

13. Calvo, R., Passeggi, M. C., Isaacson, R. A., Okamura, M. Y., and Feher, G. (1990) Electron paramagnetic resonance investigation of photosynthetic reaction centers from *Rhodobacter sphaeroides* R-26 in which Fe^{2+} was replaced by Cu^{2+}. Determination of hyperfine interactions and exchange and dipole-dipole interactions between Cu^{2+} and Q_A^-, *Biophys. J. 58*, 149-165.
14. Utschig, L. M., Poluektov, O., Tiede, D. M., and Thurnauer, M. C. (2000) EPR investigation of Cu^{2+}-substituted photosynthetic bacterial reaction centers: evidence for histidine ligation at the surface metal site, *Biochemistry 39*, 2961-2969.
15. Poluektov, O. G., Utschig, L. M., Dubinskij, A. A., and Thurnauer, M. C. (2005) Electron transfer pathways and protein response to charge separation in photosynthetic reaction centers: time-resolved high-field ENDOR of the spin-correlated radical pair $P865^+Q_A^-$, *J. Am. Chem. Soc. 127*, 4049-4059.
16. Utschig, L. M., Thurnauer, M. C., Tiede, D. M., and Poluektov, O. G. (2005) Low-temperature interquinone electron transfer in photosynthetic reaction centers from *Rhodobacter sphaeroides* and *Blastochloris viridis*: characterization of Q_B^- states by high-frequency electron paramagnetic resonance (EPR) and electron-nuclear double resonance (ENDOR), *Biochemistry 44*, 14131-14142.

Figures

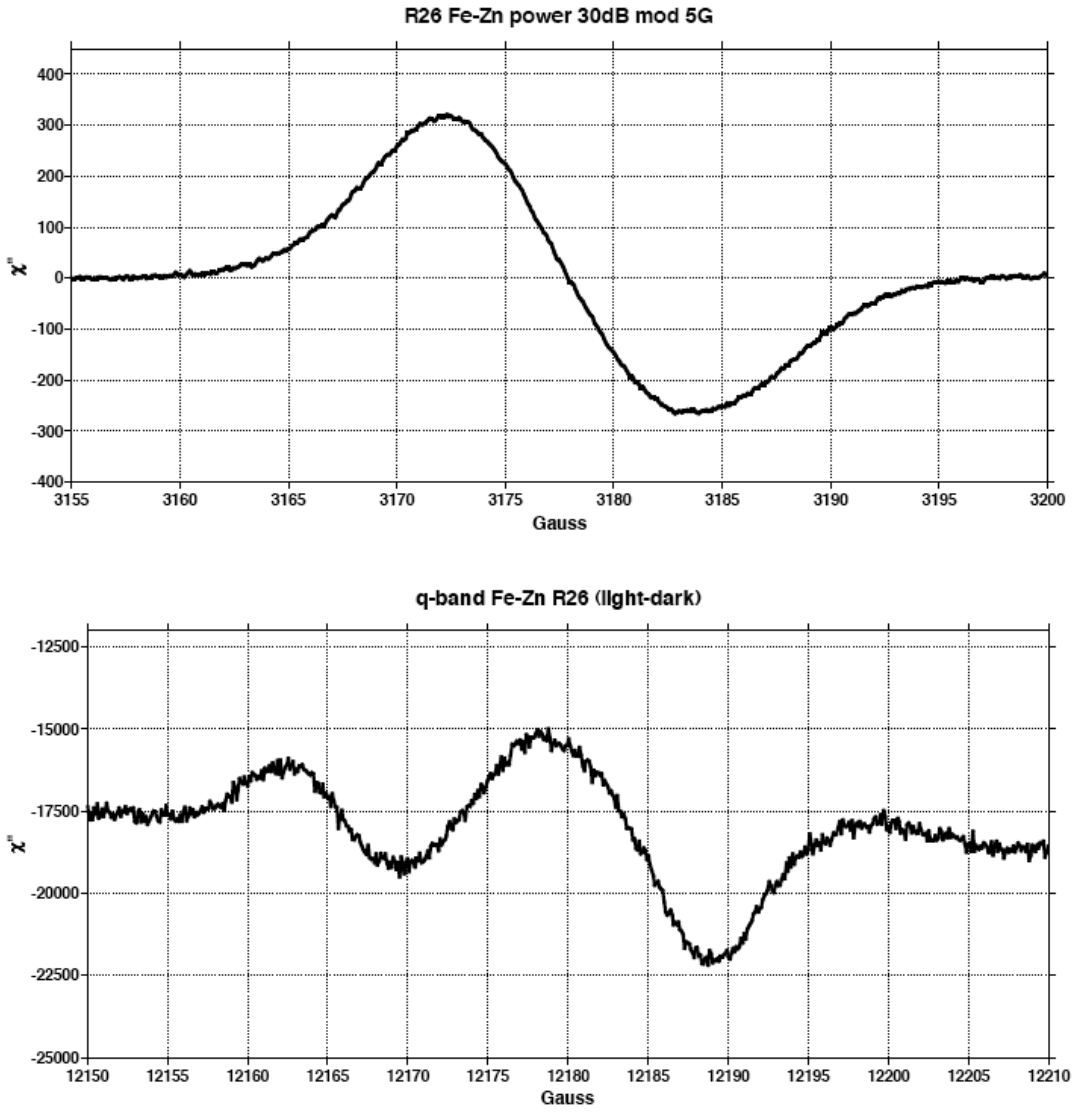

Figure 2.1. The top spectrum shows a characteristic X-band signal from reaction centers containing Zn recorded at 0.1 mW power and 5G modulation amplitude at 14^0 K. The distinctly higher intensity at low magnetic field indicates combination of P^+ and semiquinone signals. The bottom spectrum is the higher microwave Q-band spectrum recorded at 0.01mW power and 5G modulation amplitude at 60^0K. In this spectrum P^+ and the semiquinone are resolved but, due to the complexity in getting an adequate amount of light activation in the local Q-band cavity, X-band is currently the easier analytic tool. In both X- and Q-band samples the background (dark adapted) signal was subtracted from the light activated signal.

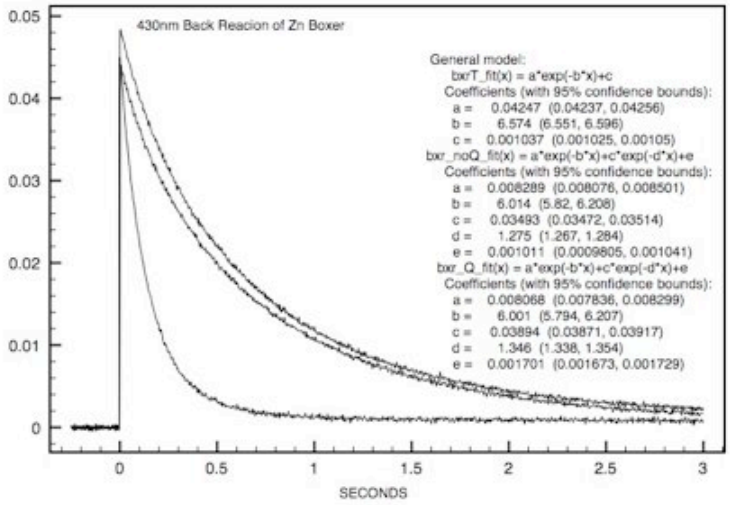

Figure 2.2. The back reaction in metal-exchanged reaction centers in a buffer containing 10 mM Tris at pH 8, 2.5 mM KCl and 0.002% LDAO. The two slower traces represent samples with no additional quinone added (lower) and with an additional 50 μM ubiquinone-10 (upper). The fast trace is from RCs in the presence of the inhibitor turbutryn to block electron transfer to Q_B. The slow recombination rate constants for the top traces are on the order of 1.3 sec^{-1}, in reasonable agreement with wild type.

Chapter 3:

Electron Paramagnetic Resonance: Theory and Application to Reaction Center Quinones from *Rba. sphaeroides*

Abstract

Electron paramagnetic resonance (EPR) has been used to explore the binding sites of the RC acceptor quinones. In the past, both continuous wave (CW) and double resonance techniques have been used to measure the properties of the g-tensor of Q_A^- and Q_B^- and hyperfine couplings of some nonexchangeable and exchangeable protons. ESEEM measurements have also been reported for two nitrogen nuclei coupled to Q_A^-. Chapter 3 outlines the theories behind these various techniques with particular emphasis on ESEEM and HYSCORE that are used in experiments in Chapters 4-6. Additionally, the current state of EPR knowledge is summarized as it applies to the experiments on quinone binding sites in this thesis.

Introduction

Electron paramagnetic resonance (EPR) is a spectrometric technique that exploits atoms having a net electron magnetic moment. In a magnetic field, these atoms can only adopt discrete orientations possessing individual energies. Interaction between electron spins and the magnetic field component of applied microwave radiation is analogous to absorption of light in optical spectroscopy. In the case of optical spectroscopy, the electromagnetic energy corresponding to the energy of a specific transition stimulates an electric dipole. Similarly, the magnetic component interacts with a magnetic dipole generated by net electron spin. (*1*) Optical spectroscopy measures the light absorption from induced electronic transitions, similarly EPR measures the attenuation of microwave radiation due to flipping electron spin between energy states.

Generically, the information in an EPR spectrum of any particular molecule can be described as measuring the departure of a signal due to the paramagnetic species from that of a "free electron", thus indicating the effect of surroundings on the magnetic properties of the unpaired electron spin. As a result, the positions of nearby electrons and nuclei have an impact on the lineshape and line location. Thus, EPR spectra can provide valuable information about the structure and quantum mechanical properties of the paramagnet and its environment.

Redox enzymes that function to transport electrons can contain transient radical species that possess unpaired electron spins. (*2*) EPR is an ideal technique for probing the atomic and electronic structure of these types of enzymes. Because EPR is sensitive to

the electronic structure surrounding the radical species, such measurements can provide information beyond the resolution of x-ray crystallography and even specifically about the molecular orbital symmetry. In the case of the photosynthetic reaction center, where both quinone electron acceptors are identical, sensitive information about their binding sites is required to understand the relationship between protein structure and function.

The major preparatory challenge of EPR studies on redox enzymes is trapping the specific radical species of interest. If cofactor redox potentials are similar targeting specific radicals can be very complicated. Fortunately the sequential nature of the light induced electron transfer reactions in the photosynthetic reaction center makes trapping specific radicals possible. This is particularly true of the acceptor quinones that are the focus of these studies, both of which form a semi-stable semiquinone radical. The general aspects of sample preparation were discussed in Chapter 2 and the specifics will be further addressed in the following chapters.

Basic CW-EPR Theory

Electrons possess an intrinsic angular momentum, the magnitude of which is given by the relationship $[S(S + 1)]^{1/2}h/2\pi$ where S is the electron spin quantum number. In the case of the semiquinones in reaction centers (and free radicals in general) $S = 1/2$. The magnetic moment of a free electron is related to the magnitude of the angular momentum multiplied by the electron gyromagnetic ratio ($\gamma_e = -ge/2m_e$). The symbol "g" represents a correction that must be used for spin angular momentum (as opposed to orbital angular momentum) and, in the case of a free electron, g = 2.00232, and

departures from this value for atomic and molecular systems reflect the electronic environment. The magnetic moment, along a specific direction or axis, z, is written as:

$$\mu_z = \gamma_e m_s h/2\pi = -g\beta m_s \qquad (1)$$

Here the gyromagnetic ratio has been separated into the g factor and the Bohr magneton, $\beta = eh/(4\pi m_e)$. The allowed values for electron spin are given by m_s. Values of m_s are quantized and span between –S and S. The importance of the g factor will become clear in the discussion of EPR spectroscopy. The subscript "z" placed on the magnetic moment indicates the direction of the magnetic field, and the coordinate system is defined, by convention, so that the magnetic field points in the z direction.

When placed in a magnetic field, electron spins only occupy discrete orientations. This quantization of the orientation is what makes the electron spin resonance phenomenon possible. The energy of a spin state can be described classically as that of a magnetic dipole in an external field:

$$E = -\boldsymbol{\mu}\cdot\mathbf{H} \qquad (2)$$

Given that the possible values of m_s are ±½, the energy of an electron placed in an external magnetic field, H_o, is expressed as follows:

$$E = \pm\tfrac{1}{2}\, g\beta H_o \qquad (3)$$

This describes two energy levels, or Zeeman states, generated by the splitting of a degenerate electron state in an external magnetic field (the "Zeeman effect"). (Figure 3.1) The energy for the transition between these states is then:

$$\Delta E = g\beta H_o \qquad (4)$$

The energy difference between the two electron Zeeman states increases linearly with the applied magnetic field.

The typical EPR spectrometer operates at a single microwave frequency, and sweeps through a region of magnetic field. Microwaves are defined as the portion of the electromagnetic spectrum between 0.3 GHz and 300 GHz, and the most common microwave frequency used in EPR spectroscopy is X-band, typically between 9-9.5 GHz.[a] However, higher and lower frequencies are increasingly used to provide information specific to the samples of interest. (Table 3.1)

Table 3.1. Microwave Frequency Band Designations

Band Designation	Frequency (GHz)
L	1-2
S	2-4
C	4-8
X	8-12
Q	30-50
W	75-110
D	110-170

In an experiment, the attenuation of applied microwave radiation is measured as a function of magnetic field. When the magnetic field separates the Zeeman levels of the

[a] The ubiquitous nature of X-band EPR spectroscopy at these frequencies happened by chance and originated purely out of existence of surplus microwave sources operating at this frequency left over from WWII radar applications. In fact, all the "letter" designations of microwave frequencies were originally military code.

free electron to an energy that matches the applied microwave radiation (the resonance condition), a signal will be observed.

In EPR, the condition of resonance for a particular radical is typically expressed as a g-value, Eqns. 3 and 4. In addition, it is often useful to express g with the constants combined in the common units for the microwave radiation and magnetic field of "GHz" and "Gauss", respectively:

$$g = h\nu/\beta H \qquad (5)$$

$$g = 714.484 \times (\nu/H)$$

ν is in units of GHz and H is in units of Gauss

In a perfectly spherically symmetric and isolated radical, the g-value will be a scalar and the EPR signal will be a single, narrow line broadened only by the spin-lattice relaxation time (T_1). In the typical ensemble there is additional homogeneous broadening due to spin-spin relaxation (T_2) causing the instantaneous magnetic field felt by individual electrons in the samples to be non-equivalent. This type of isotropic, homogeneous broadening of a line results in a Lorentzian line shape.

A radical that is not isolated or spherically symmetric can also be inhomogeneously broadened resulting in a Gaussian lineshape. The major source of inhomogeneous broadening is unresolved hyperfine interactions (HFI) originating from magnetic coupling between nuclei and the unpaired electron spin. Similar to electrons, nuclei also possess intrinsic angular momentum and thus a magnetic moment. The g-value at which an EPR transition occurs is a function of the magnetic field felt by the electron. As so far described, this magnetic field is supplied by a source exterior to the sample. However, the magnetic field from nearby nuclei (H_N) will add to the applied

external field (H_o) resulting in an effective field at the electron that is the vector sum: $\mathbf{H} = \mathbf{H_o} + \mathbf{H_N}$. Similar to electron spin, nuclear spin is also quantized, and therefore the sum magnetic field will have discrete values. The multiplicity of hyperfine splitting is dependent on the nuclear spin (I) and will obey the general equation 2I+1. Therefore, in the simplest case of an I = ½ nucleus, the EPR line will be split once. In this case, the nuclear spin can have either of the allowed values $m_I = \pm ½$, producing two different magnetic fields at the electron.

$$H = H' \pm A/2 \qquad (6)$$

In Equation 6, the magnetic field, H, describes where the resonance will occur relative to the magnetic field, H', that would induce the transition in the absence of any HFI. The term $A/2$ describes the magnetic field supplied the nucleus. A is the splitting between two levels, and is referred to as the hyperfine coupling constant.[1] In cases where A is large compared to the CW-EPR linewidth, HFIs are not resolved in CW-EPR and instead manifest as inhomogeneous broadening. This is true in the case of the quinone radicals in the photosynthetic reaction center. HFI has only been resolved in spectra where carbon or oxygen on the quinone head group has been isotopically labeled. (*3, 4*) Hence, discussion of hyperfine coupling is limited here, and will be referred to in greater detail later in the context of pulsed EPR techniques.

Anisotropy of the g-value also causes line broadening and, in many cases, gives rise to line shapes dramatically different from either Gaussian or Lorentzian. Anisotropic effects are defined as those that depend on the orientation of the magnetic field. In the

[1] It should be noted that the symbol "*A*" will typically be used to denote the total hyperfine coupling. The complete coupling constant can be divided into isotropic and anisotropic (independent or dependent on magnetic field orientation) components which are designated with the symbols *a* and *T* respectively.

case of g-value anisotropy, the resonance condition depends on the orientation of the external magnetic field relative to the molecular axis - g is now expressed as a tensor rather than a scalar. In "powder type" samples, it is assumed that all elements of the ensemble are randomly oriented relative to the applied magnetic field. It follows that EPR transitions will be visible at all values of the magnetic field spanning the entire g-tensor. In randomly oriented samples, the probability of transitions is greater at magnetic fields corresponding to the inflection points between principle components of the g-tensor.

CW-EPR Spectroscopy and Photosynthetic Reaction Center Quinones

The light-induced events of photosynthesis are a cascade of single electron transfers. This makes EPR an ideal technique to identify the electron carrier species. Initial measurements at X-band saw an EPR response to light activation, producing a spectrum with a narrow line at g = 2.0026 and a broad signal centered about g = 1.8. (*5-7*) (Figure 3.2) The narrow signal was attributed to the primary donor, and the broad signal was assumed to be from an (at the time unidentified) acceptor. The broad signal was suggestive of transition metals that can exhibit large g anisotropy and was initially expected to originate from an Fe. However, the Fe^{3+}/Fe^{2+} (or Fe^{2+}/Fe^{+}) redox couples that would operate if Fe were an electron donor or acceptor would not produce the observed EPR signal. For example, Fe^{2+} has an even number of electrons and wouldn't produce an X-band EPR signal by itself, and Fe^{3+} (and the improbable Fe^{+}) would have a distinctive signal at g values significantly greater than 2. (*6*)

Another report of the light induced EPR signal showed a shift of the g = 2.0026 signal to g ~ 2.005, (*8*) which was attributed to a second, unresolved, narrow signal combining with that of the primary donor. In a case of serendipity, it was concluded that a harsh reaction center isolation procedure resulted in partial removal of the native Fe^{2+}. This chance occurrence led to the eventual, correct conclusion that the broad, g = 1.82, EPR signal was attributable to the coupling of a high spin Fe^{2+} to the organic radical, ubisemiquinone-10. (*6*) In the supervening years it has become established that the native Fe can be consistently removed (and replaced with alternate divalent cations) with various biochemical procedures, making it possible to study the EPR properties of the individual quinone acceptors. (*4, 9, 10*)

Signals specific to Q_A and Q_B semiquinones were first identified at X-band and proved to be quite similar with values of g = 2.0046 and g = 2.0045 respectively. (*4, 11*) At X-band the components of the g-tensor are not resolved, and the lineshape is a single Gaussian curve suggesting the presence of anisotropy and unresolved HFI. Overcoming this inherent shortcoming of X-band spectroscopy has been approached in three different ways. The protein, quinone, buffer or all three can be deuterium exchanged, changing and eliminating some HFI that inhomogeneously broaden the spectrum. The microwave frequency can be increased from X-band, spreading apart the components of the g-tensor. Finally, single reaction center crystals have been studied where the orientation of the reaction center relative to the magnetic field is known.

A significant amount of the broadening of the semiquinone signals is due to unresolved hyperfine interactions. By substituting protons (I = 1/2) with deuterons (I = 1), the splitting due to hyperfine coupling is diminished, resulting in a narrowing of the

linewidth. At X-band, the result is to reveal a pronounced asymmetry in the Gaussian signal, indicating inhomogeneous broadening due to g-tensor anisotropy in addition to unresolved hyperfine interactions. However, the use of deuterated reaction centers must still be combined with higher field EPR measurements to fully resolve the g-tensor.

Equation 4 and Figure 3.1 indicate that increasing the microwave field frequency will spread the spectrum over a wider range of magnetic field. Therefore, features unresolved at X-band may be seen at higher frequency, and this is the case with the reaction center semiquinones. When measured at Q-band, Q_A^- shows a lineshape typical of a radical with axial symmetry, (*1*) with parallel and perpendicular components of the g-tensor at $g_{\|} = 2.0022$ and $g_{\perp} = 2.0059$. (*12*) The complete g-tensor has been resolved at Q-band for Q_A^- using single reaction center crystals (where the orientation relative to the magnetic field was known) and for Q_B^- in fully deuterated samples. (*11*) (Table 3.2)

Table 3.2 g-tensor for Q_A and Q_B measured in single crystals (*11*)

	Q_A	Q_B
g_x	2.00649	2.00626
g_y	2.00532	2.00527
g_z	2.00210	2.00210

The values in Table 3.2 support all previous conclusions from Q-band and W-band studies that show the g-tensor to have near axial symmetry. The principle axis of the g-tensor is shown in Figure 3.3. The z-axis points out of the plane of the quinone while the

x-axis lies along the quinone carbonyl oxygen. An interesting feature of the g-tensor becomes apparent when the semiquinone in either binding pocket is compared to semiquinone in solution, in DME-MTHF (1,2-dimethoxy ethane, 2-methyl tetrahydrofuran) or 2-propanol. (*13*) The g-tensor is quite similar, but does deviate in the x component. As indicated in Figure 3.3, the x component points along the carbonyl groups and these deviations are consistent with hydrogen bonding. The nature of these interactions can be studied by specific isotope labeling of the carbonyl oxygen and carbon (with ^{17}O I = 5/2 and ^{13}C I = 1/2) on the quinone. (*4, 14*) In these cases, the hyperfine interactions are large enough to be resolved in CW-EPR spectra, and the size of these couplings is related to the spin density residing on the particular nuclei. However, to examine the hyperfine coupling of the hydrogen bonding partners, more sophisticated double resonance (ENDOR) or pulsed techniques such as ESEEM are required.

Electron Nuclear Double Resonance (ENDOR) Spectroscopy

Hyperfine interactions (HFI) with neighboring nuclei can provide critical information about a radical's environment. However, most hyperfine interactions with distant nuclei are sufficiently small that they are unresolved in CW-EPR spectra. These small interactions can be detected by measuring the effect on the EPR signal of radio frequency-induced nuclear transitions. (*15*) Essentially, NMR signals are detected by EPR and, as such, the technique was aptly named Electron Nuclear Double Resonance (ENDOR). Due to the higher energy of the EPR transitions, it is possible to resolve NMR transitions by this method at far lower concentrations than is possible by NMR alone.

The basic CW-EPR experiment shows a signal at a certain g-value for a given EPR transition, which typically increases in amplitude with the square root of the microwave radiation power. With increasing power the proportionality diminishes and eventually the amplitude begins to decrease as the EPR signal saturates. In a static field ENDOR experiment, the values of microwave frequency and magnetic field are held constant at resonance for a particular EPR transition, and the power of the microwave radiation is increased to the point where the signal is saturated. Hyperfine coupling between nuclei and the unpaired electron splits the Zeeman energy for each electron spin manifold.(Figure 3.4) Triggering a transition between the nuclear energy levels will change the magnetic field at the electron and hence the energies in the electron spin manifolds. Changes in the energies will decrease the degree of saturation of the EPR transition and increase the signal at the detector. To see this effect, the sample is swept through a range of radio frequencies at high enough power to induce an NMR transition. The resulting spectrum of the EPR signal amplitude as a function of radio frequency will have peaks separated by the hyperfine coupling and centered on the frequency (ν_N) for the particular nucleus (Eqn 7). This is referred to as the ENDOR spectrum.

$$\nu = |A/2 \pm g_N \beta_N H| \qquad (7)$$

$$g_N \beta_N H = \nu_N$$

In Eqn 7, the parameters g_N and β_N are the nuclear constants similar to those presented in Eqn 4 for electrons – the nuclear g factor and magneton. This type of ENDOR experiment can provide very detailed information about the hyperfine coupling, given by the splitting of the pair of peaks, and about the type of nucleus, which is characterized by the frequency ν_N. Much like the g-tensor, the hyperfine coupling can exhibit anisotropy.

In the case of hyperfine anisotropy, the splitting is dependent on magnetic field orientation and the coupling constant must be expressed as a tensor. If the sample is free to rotate, any effects due to the orientation relative to the magnetic field are averaged out and Eqn. 7 describes isotropic hyperfine interactions. However, in frozen "powder type" spectra, as for typical reaction center samples, anisotropy can be resolved in ENDOR when components of the g-tensor can be resolved in CW-EPR. If the magnetic field and microwave frequency are set at the center of an EPR line, the ENDOR signal will be broadened by all the anisotropic components contributing to that point in the EPR spectrum. However, the experiment can be set at a section (away from the line center) of the EPR signal relating to a particular component of the g-tensor, and in single crystals the orientation of the tensor will be known.

ENDOR is particularly sensitive to nuclei with large Larmor frequencies – the frequency of the nucleus in a magnetic field - making it a very useful technique for examining protons surrounding the unpaired electron. Signals attributable to protons can be organized into three types. The major contribution to the spectrum, with large isotropic and anisotropic hyperfine coupling values, is due to protons integral to the radical of interest. In the case of ubisemiquinone, these would be the methyl and methylene protons from the quinone headgroup alkyl substituents. (Table 3.3) Distant (matrix) nuclei show very small, almost exclusively anisotropic, hyperfine splitting. Falling between the two are protons contributing through hydrogen bonding to the radical. These are potentially exchangeable with the addition of deuterated buffer.

Various methods of orientation selection have been used to examine the complete hyperfine tensors of methyl (at C5) and methylene (at C6) protons in the semiquinones of

reaction centers. (*4*) The conclusion is that the electronic structure of the semiquinone in the Q_A site is highly asymmetric, with electron density favoring the O4 side. Similar measurements on the Q_B semiquinone show a lesser degree of asymmetry. These results are in agreement with the conclusions obtained in CW-EPR experiments using ^{17}O and ^{13}C labeled quinones.

Table 3.3 Hyperfine Tensors for CH_2 and CH_3 Determined at 35GHz and in Single Crystals for Q_A^-

		Frozen	Crystal
CH_2	A_x	8.8	8.85
	A_y	5.4	5.51
	A_z	5.4	4.95
	A	6.5	6.43
CH_3	A_x	6.8 (7.8 - Q_B)	6.68
	A_y	3.6 (4.4 - Q_B)	3.59
	A_z	3.6 (3.9 - Q_B)	3.09
	A	4.6	4.45

(measurements were performed on M266 His -> Cys mutant reaction centers) (*4, 11*)

Also shown in Table 3.3 are values of the hyperfine tensor for CH_3 type protons coupled to Q_B^-, also obtained at Q-band ($\{A_x\ A_y\ A_z\} = \{7.8\ 4.4\ 3.9\}$). An important conclusion from these results is that the electronic structure of Q_B is significantly different from Q_A.

Of particular interest to the work in this thesis are ENDOR data pertaining to protons that are exchangeable in D_2O. In order to gain additional resolution, substituting deuterated quinones, or even using fully deuterated enzyme, allows for elimination of signals from integral and matrix protons. Signals from exchangeable protons are presumed to arise from nuclei participating in hydrogen bonds with the semiquinones, and consequently will provide specific information about interaction between the semiquinone and the protein environment.

Experiments at X-band on reaction center samples in H_2O and D_2O buffers identified three exchangeable ENDOR lines in the Q_A^- spectrum, at $A_1 = 4.6$, $A_2 = 6.2$ and $A_3 = 8.9$ MHz. Similar experiments on Q_B^- only showed 2 lines centered at $A_1 = 3.1$ and $A_2 = 5.0$ MHz. (*4*) Measuring the intensity of these lines as a function of time after the buffer was exchanged from H_2O to D_2O showed the signals in both Q_A^- and Q_B^- spectra to be attributable to at least two different protons. In the Q_A^- spectrum the exchange times were separated by over one order of magnitude and showed that the two smaller couplings (A_1, A_2) were attributable to different protons and were assigned as the $A_\perp$ contribution. The intensity of the peak with larger coupling (A_3) was much weaker but was assigned to $A_\parallel$ and most likely is attributable to the same proton as A_1. However, it could include contributions from both protons. The two couplings shown in Q_B^- spectra also showed different exchange times, (*4*) but the difference in exchange rates (~20 sec and <<10 sec for A_1 and A_2, respectively) was not as dramatic as in spectra of Q_A^-.

For Q_A^- the hyperfine tensor of the exchangeable protons has been studied by orientation selected Q-band ENDOR, using fully deuterated reaction centers to minimize contributions from all non-exchangeable protons. (Table 3.4)

Table 3.4 Hyperfine Tensors for Exchangeable Protons Coupled to Q_A^- (*16*)

Proton	A_x	A_y	A_z	a	exchange
1	10.43	-5.23	-5.20	-1.28	Slow
2	9.12	-4.75	-4.37	-0.17	Fast

The slowly exchanging proton (1) exhibits nearly perfect axial symmetry. The more quickly exchanged proton (2) shows a slight rhombicity of the hyperfine symmetry, but the deviation from axial is small enough that the tensor can be approximated as (9.12, -4.56, -4.56 MHz). These values support the previous assignment of A_1 and A_2 as contributions from $A_\perp$ from two separate protons, and A_3 arising from overlap of the parallel component ($A_\parallel$) of both of these tensors. These values are explicitly calculated and presented in Table 6.1 of Chapter 6. The slowly exchanged proton has been assigned to the hydrogen bond between His-M219 and O4 semiquinone carbonyl, while the quickly exchanged proton is assigned to the Ala-M260 O1 hydrogen bond. (*16, 17*)

ESEEM (Electron Spin Echo Envelope Modulation) Spectroscopy

Much like ENDOR, ESEEM is a technique used to resolve small features that are seen only as inhomogeneous broadening in a CW, field-swept EPR spectrum. Unlike ENDOR, which requires both radio frequency and microwave radiation to induce

electron and nuclear Zeeman transitions, ESEEM measures the direct modulation effect of coupled nuclei on the EPR signal.

ESEEM relies on the electron spin echo (ESE) generated by pulses of microwave radiation. The simplest form of the ESE utilizes a two pulse sequence. (*18*) The sample in the EPR cavity sits in a static magnetic field set to a particular electron Zeeman transition, and then interacts with the magnetic field component of the pulsed microwave radiation, which reorients the net magnetization of the sample. The angle through which a microwave pulse moves the magnetization is given in Equation (8).

$$\theta = \gamma_e H_{mw} t_p \qquad (8)$$

In Eqn. 8 γ_e is the electron gyromagnetic ratio (1.76 x 10^7 rad s^{-1} G^{-1}), H_{mw} is the amplitude of the magnetic field component of the microwave radiation, and t_p is the width of the microwave pulse. The typical excitation component of a Bruker spectrometer generates ~1 kW microwave power, which is sufficient to generate $H_{mw} \sim 10$ G. At this power, a $\pi/2$ pulse will be 12-16 ns in duration (t_p) - most pulses used have a value of $\theta = \pi/2$ or π. In the simple two pulse echo experiment, the sample is exposed to a $\pi/2$ pulse that turns the net magnetization into the xy plane (the z axis is defined as the direction of the external magnetic field, and at equilibrium the magnetization will be parallel to the external field). EPR transitions are frequently inhomogeneously broadened, and comprise many separate homogeneous components. After the $\pi/2$ pulse individual components will "fan" out in the xy plane.(Figure 3.5) A π pulse at time τ will flip the magnetization 180 degrees in the xy plane, causing the dispersion to reverse and the individual spin components subsequently to converge. At a time 2τ the original magnetization in the xy

plane will be restored (minus any loss due to relaxation), accompanied by spontaneous emission of microwaves called the "spin echo". (*18, 19*)

The origin of the emission of microwaves can be understood by examining the behavior of the spin system before, during and after it is exposed to $\pi/2$ or π pulses. Prior to any exposure to microwaves, the sample is in thermal equilibrium with the external magnetic field (H_o). The electron magnetic moments will either align parallel or anti-parallel to H_o. Alignment of the spin magnetic moment with the external magnetic field is the lower energy state and, at equilibrium, has higher occupancy, as given by the Boltzmann relationship: n(anti-parallel)/n(parallel) = $e^{-\Delta E/kT}$. The magnetization is a macroscopic property of the sample and is defined as the vector sum of all magnetic moments. In the case of thermal equilibrium, the magnetization will be aligned with the external magnetic field – and in the z axis of the reference frame by convention.

As described by Eqn 8, a microwave pulse of suitable power and duration can tip this magnetization through the angle $\pi/2$. The microwave radiation is linearly polarized and can be in any orientation in the xy plane. In a case where the microwaves are polarized in the +x direction, a $\pi/2$ pulse will tip the net magnetization from aligned with the z axis to parallel to the –y axis. As soon as the magnetization is tipped away from its alignment with the external magnetic field, the sample is no longer in thermal equilibrium and will proceed to relax from its new orientation. Although many spins cancel out, the result is a rotation of the net magnetization in the xy plane, which functions as a generator creating a microwave signal in the resonator cavity.

The transverse magnetization (describing the magnetization in the xy plane) will spread out in the xy plane because the rate at which individual spins precess depends on

the Larmor frequency, which varies with the magnetic field perturbed locally by contributions from any inhomogeneous broadening. (Figure 3.5) After the $\pi/2$ pulse, the spins fan out evenly in the xy plane and generate a microwave signal which diminishes non-exponentially called the free induction decay.

If, at time τ after the $\pi/2$ pulse, the sample is exposed to a π pulse, the precession of the individual spins will be inverted but will proceed at the same rates. Consequently, the spins will begin to converge on the +y axis. As the sample regains its spin coherence, there will again be a rotation of net magnetization resulting in the generation of microwaves. This signal reaches a maximum at time 2τ after the initial $\pi/2$ pulse and is known as the primary or Hahn echo. The echo can be imagined as the time reversed free induction decay that is generated as the system regains coherence, followed by the free induction decay as it again fans out. (*20, 21*) As the value of τ between pulses increases the amplitude of the spin echo will decrease. The generation of the Hahn echo is based on the progression of the transverse magnetization of the sample, and will decrease in amplitude due spin relaxation processes - spin-lattice relaxation (T_1) and spin-spin relaxation (T_2). T_1 describes the magnetization regaining thermal equilibrium with the z-axis and is slow relative to T_2, which is the spreading of the magnetization in the xy plane. In the two pulse sequence, the coherence is always in the xy plane and the amplitude of the echo depends on T_2.

If the electron spin is coupled to a nuclear spin, the electron energies are split due to hyperfine or nuclear quadrupole interactions and the decay of the spin echo with τ will be modulated at a frequency characteristic of the coupled nucleus. Magnetic coupling between nuclei and the electron spin causes the precession frequency (Larmor frequency)

of a particular spin to increase or decrease depending on the spin state of coupled nuclei. As the magnetization regains coherence some spins will be missing resulting in incomplete echo generation. Measuring the echo intensity as a function of τ and subtracting the baseline decay will give a trace of oscillations generated by nuclei coupled to the paramagnetic electron. A Fourier transform of this signal will provide the spectrum of the frequencies that modulate the echo intensity. This type of measurement is referred to as electron spin echo envelope modulation or ESEEM. (*22*)

The intensity of the echo after the 2-pulse sequence decays as a function of T_2, spin-spin relaxation. (*19*) The orientation of the magnetization is in the xy plane during the entire mixing phase, when the individual spins are allowed to fan out. This phenomenon illustrates the primary shortcoming of a two pulse ESEEM experiment - T_2 is a relatively fast phenomenon and limits measurements to short values of τ, thus reducing the possible resolution of the experiment, particularly in the context of lower frequency nuclei. As the frequency of the nuclear coupling decreases, longer time dependences of echo intensity are required for good resolution. A substantial increase in resolution can be obtained by using a sequence of three $\pi/2$ microwave pulses. (Figure 3.6) A sequence of three pulses will generate five distinct echoes. Three of these are Hahn echoes and one is a refocused echo, all generated from combinations of two pulses. The fifth echo, of primary interest in the 3-pulse ESEEM experiment, is the "stimulated echo" generated at time $T + 2\tau$ after the third pulse, where T is the time between the second and third pulses. In a 3-pulse ESEEM experiment, the second $\pi/2$ pulse flips the magnetization from the xy plane into the xz plane. Samples will regain thermal equilibrium along the z axis based on spin-lattice relaxation (T_1), which occurs on a much

slower time scale than T_2 allowing for the echo to be measured on a much longer time scale. However, it should be noted that the time τ between the first and second pulse is still limited on the high end by T_2 relaxation. (*21*)

Given the greater efficacy of 3-pulse ESEEM experiments, a lot of information about coupled nuclei can be extracted from these data alone. However, in complicated systems, such as the semiquinone binding sites, where the paramagnetic species is coupled to many different types of nuclei with varying strength, it is useful to spread the ESEEM spectrum into two dimensions. A 3-pulse ESEEM experiment can be transformed into two dimensions by collecting spectra as a function of both the time τ between the first two pulses, and the time T between the second and third pulses. In this way its possible to ensure that no peaks are missing due to τ-dependent suppression effects, and 3-pulse spectra are often presented as a stacked plot with multiple values of τ. (*19, 23, 24*)

Highly congested spectra can be spread into two dimensions in a 4-pulse HYSCORE (hyperfine sublevel correlation) experiment. (*25*) The HYSCORE pulse sequence inserts a π pulse between the second and third pulses of the 3-pulse stimulated echo sequence, breaking the time T into t_1 and t_2. The first two pulses are still $\pi/2$ and are referred to as the preparatory time domain, since it is during this time period that the net magnetization is tipped into the xy plane and allowed to precess for time τ before being again tipped into the xz plane, where it is governed by spin lattice relaxation. The evolution period after the second pulse is broken up by a π pulse that flips the magnetization and generates correlations between the α and β spin manifolds (i.e., Zeeman transitions from different nuclear spin states). A π pulse flips the net spin of the

system by 180 degrees. Thus, during the evolution period the electron spin will "experience" the nuclear spin in both the spin up and spin down state for times t_1 and t_2. The final $\pi/2$ pulse serves the same function as in the 3-pulse ESEEM sequence (bringing the magnetization back to the xy plane) and generates the stimulated echo at time τ after the final pulse. HYSCORE data are recorded as a two dimensional data set as both t_1 and t_2 are varied. τ is held constant during each sweep of t_1 and t_2. However, often spectra are recorded at multiple values of τ because peak suppression effects vary with τ and there is generally no single "best" value. After a double Fourier transform with respect to both t_1 and t_2 time coordinates, a two-dimensional spectrum with two frequency axes is obtained. (*21*) In this coordinate system, the classic 3-pulse ESEEM spectrum appears along the diagonal of the (+,+) quadrant (and is mirrored in the (-,-) quadrant). Cross peaks off the diagonal demonstrate correlations between peaks on the diagonal that arise from transitions in the different manifolds of the same nucleus. (*22*)

In the semiquinone sites of the photosynthetic reaction centers, the primary nuclei of interest are nitrogens and protons – the coupling of both can be examined using ESEEM spectroscopy, both 3-pulse and HYSCORE. Analyzing spectra containing proton or nitrogen couplings presents different challenges arising from their different nuclear Larmor frequency and spin.

Analysis of ESEEM from I = 1 Nuclei

ESEEM spectra of the reaction center semiquinones are dominated by peaks associated with ^{14}N, which has spin I = 1 and possesses a quadrupole structure. In these samples, ESEEM modulations due to quadrupole coupling to the paramagnetic electron

overwhelm the spectrum and make analysis for other nuclei impossible. However, valuable information can be obtained from the quadrupole interactions. (*26*) The ESEEM spectrum of an electron spin coupled to a ^{14}N nucleus can be quite complicated with up to six lines (three lines each from opposite electron spin manifolds $+m_s$ and $-m_s$). Even when expanded into two dimensions in a HYSCORE experiment, cross correlations between spin manifolds create even more peaks and can make for an exceptionally congested spectrum. However, under special circumstances, known as a "cancellation condition", the quadrupole contributions to the spectrum are substantially simplified. This arises when the HFI is approximately twice the nuclear Larmor frequency.

In the cancellation condition, the hyperfine contribution disappears in one manifold, allowing for easier spectral analysis. Equation 9 gives the nuclear spin Hamiltonian for a spin S = ½, I = 1 system.

$$\hat{H} = \nu_{ef}\left[\hat{I}_z\cos\theta + \hat{I}_x\sin\varphi + \hat{I}_y\sin\theta\cos\varphi\right] + K\left[3\hat{I}_z - \hat{I}^2 + \frac{\eta}{2}\left(\hat{I}_+^{\,2} + \hat{I}_-^{\,2}\right)\right] \quad (9)$$

The spin Hamiltonian describes the projection of the nuclear spin (*I*) onto the principal axes of the electric field gradient; the angles θ and φ relate the electric field gradient axis system to the laboratory frame. Eqn. 9 consists of the sum of two components. The first half is the observed frequencies, ν_{ef}, which represent the effective nuclear frequency, as determined by hyperfine interactions. The second term is and the nuclear quadrupole interactions.

The frequencies that are manifest in an ESEEM spectrum for ^{14}N nuclei will be dependent on the hyperfine coupling and the relationship, $\nu_{ef} = {}^{14}\nu_N \pm {}^{14}A/2$, (Eqn 7.) where ${}^{14}A$ is the ^{14}N hyperfine coupling constant and ${}^{14}\nu_N$ is the ^{14}N nuclear Larmor

frequency (~1 MHz at X-band). In the event that the hyperfine coupling is approximately twice the nuclear Larmor frequency, the effective nuclear frequency (ν_{ef}) will be ~0 in one electron spin manifold and ~$2\nu_N$ in the other. At X band, this implies a hyperfine coupling constant of ~2 MHz. (*26, 27*) In this special case, the transitions in the cancelled manifold will be similar to the "zero-field" nuclear quadrupole transitions (i.e., in the absence of HFI splitting) and will appear in the 3-pulse ESEEM spectrum as three sharp peaks associated with the three nuclear transitions in that manifold, ν_o, ν_- and ν_+ (Figure 3.7). These three features are easily identified in ESEEM spectra because they obey the relationship: $\nu_o + \nu_- = \nu_+$. In addition to allowing for identification of a spin I = 1 system, the degree to which the peaks fit this model indicates how close the spin system is to exact cancellation.

In spin $I = 1$ systems, the parameter $K = e^2q_zQ/4h$, the quadrupole coupling constant, also determines the line shape (Q is the nuclear quadrupole moment). (*27*) In the ideally canceled case, ν_{ef} will equal 0 but, at $\nu_{ef} > 0$, the extent to which it is possible to see a triplet associated with zero field quadrupole transitions is determined by the ratio of the effective frequency and the quadrupole coupling constant (ν_{ef}/K). At ratios below ~0.75 it is possible to see a well resolved triplet of zero field transitions, while between 0.75-1 the peaks become so broadened that they cannot be distinguished. When $\nu_{ef}/K > 1$, the approximate zero field transitions no longer appear in the spectrum and transitions between nuclear states $m_I = 1$ and $m_I = -1$ (the double quantum transition) from each spin manifold will dominate the spectrum. (*19, 26*) Out of cancellation, single quantum transitions between $m_I = \pm 1$ and $m_I = 0$ are allowed but are not expected to be resolved in

disordered powder-type samples, such as frozen photosynthetic reaction centers, due to a strong orientation dependence.(*19*)

In a spectrum where ν_{ef}/K is sufficiently small, the zero field transitions are characterized by the quadrupole coupling parameter and an asymmetry parameter (η):

$$\eta = \frac{q_{xx} - q_{yy}}{q_{zz}} \tag{8}$$

The asymmetry parameter, which ranges from 0 to 1, describes the structure of the electric field at the nucleus as a ratio of the principal components of the electric field gradient (EFG) tensor given in Equation 8. In contrast, K is only dependent on the z component of the EFG ($K = e^2q_zQ/4h$). In terms of K and η the three zero field transitions can be described by:

$$\begin{aligned} \nu_+ &= K(3+\eta) \\ \nu_- &= K(3-\eta) \\ \nu_o &= 2K\eta \end{aligned} \tag{9}$$

If values for the three transitions are obtained from experiment, these equations can be used to solve for K and η. The quadrupole coupling constant is characteristic for the type of nucleus to which the paramagnetic electron is coupled.[2] (*28*) The asymmetry parameter is less sensitive to the specific type of nucleus, but can provide insight into the electronic and orbital structure. (*29*)

At cancellation, one electron spin manifold will show near zero field nuclear quadrupole transitions. The second solution to the equation $\nu_{ef} = {}^{14}\nu_N \pm {}^{14}A/2$ manifests in

[2] In principle, this analysis applies to any orientationally disordered system with nuclei I ≥ 1. However, in this thesis, the analysis is applied to ^{14}N nuclei, which have very strong nuclear quadrupole interactions, and the phrase "type of nucleus" refers to which type of nitrogen, i.e., its chemical bonding.

experiment as a double quantum transition, which is described by a combination of ν_{ef} and K.

$$\nu_{dq} = 2\left[\nu_{ef}{}^2 + K^2\left(3+\eta^2\right)\right]^{\frac{1}{2}} \qquad (10)$$

The typical 3-pulse ESEEM spectrum of a sample with a coupled ^{14}N nucleus exhibiting near cancellation conditions will therefore contain four peaks – the three zero field quadrupole transitions and a broader, higher frequency feature that is the double quantum transition. If these four features are well resolved, it is possible to solve for ν_{ef} and, in turn, obtain a reasonable estimate of the hyperfine coupling despite the fact that the spectrum is overwhelmed by nuclear quadrupole features.

In principle this type of analysis can be applied to 3-pulse ESEEM spectra but, expanding the spectrum into two dimensions, as in HYSCORE, can be very beneficial. In complicated systems, where the paramagnetic electron is coupled to multiple spin I = 1 nuclei, it is often difficult to ascertain which peaks are associated with the zero field quadrupole peaks of a single nucleus. Correlations between electron spin manifolds generated in a HYSCORE spectrum can clarify this by generating off-diagonal peaks attributable to a single nucleus. (*25*) Additionally, cross correlations generated by a HYSCORE pulse sequence greatly increase the resolution of peaks associated with double quantum transitions. Generally, the double quantum peak is of low intensity (relative to the zero field transitions) and is broadened. In samples that contain couplings to multiple I = 1 nuclei, the double quantum transitions can form a very broad feature without distinct, multiple maxima. A HYSCORE spectrum correlates the zero field transitions from one electron spin manifold with the associated double quantum transition

in the opposite spin manifold. These correlations make it possible to resolve accurate values for the double quantum transition frequency for multiple nuclei in a HYSCORE experiment, whereas only a general estimate for all nuclei is available in a 3-pulse experiment, calculated from the center of overlapping broad peaks.

Analysis of ESEEM from I = 1/2 Nuclei

The above analysis applies only to systems with nuclei possessing spin greater than ½ having quadrupole structure and thus energy levels separated by the EFG in addition to the external field. Analyses of ESEEM and HYSCORE of paramagnetic electrons coupled to spin I = ½ nuclei require different approaches. Of particular interest in the case of redox proteins such as the reaction center are ^{1}H and ^{15}N. The complexity of analyzing spin I = ½ nuclei is dependent on the specific nucleus, in particular the Larmor frequency, which determines the position and shape of the peaks. The majority of nuclei coupled to the paramagnetic electron occupy the "weak hyperfine" limit that encompasses I = ½ nuclei with virtually no isotropic (independent of magnetic field orientation) hyperfine coupling. The primary peak is expected to be at the nuclear Larmor frequency for the particular nucleus (~14.7 MHz and 1.4 MHz for ^{1}H and ^{15}N, respectively, at X-band). In a 3-pulse ESEEM spectrum a weakly coupled I = ½ nucleus will generate a peak broadened around the Larmor frequency. In HYSCORE spectra, peaks will appear in the (+,+) quadrant on the diagonal. In the limit of zero isotropic hyperfine coupling this feature will be circular and sharp; moving away from the limit, the feature will broaden and elongate. (*19, 21*)

Of particular interest are nuclei that exhibit stronger coupling to the paramagnetic electron and potentially are structurally relevant to the paramagnetic center. HYSCORE is the best technique to analyze these relationships - information from the shape of the correlated spin manifolds can be used to determine the anisotropic hyperfine tensor (***T***) and isotropic (*a*) hyperfine coupling. In these cases, it is expected that there will be two major peaks that significantly deviate from the Larmor frequency and, in the right circumstances, can even appear in the (-,+) coordinate. The quadrant in which hyperfine peaks are expected to appear can be predicted from the relationship between the nuclear Larmor frequency and the strength of hyperfine coupling.

In the case of strong hyperfine interactions, $|T+2a| > 4\nu_N$, it is expected that the peaks will be in the (-,+) quadrant whereas, when $|T+2a| < 4\nu_N$, the peaks are expected to be found in the (+,+) quadrant. In the latter case, the crosspeaks are expected to be centered on the nuclear Larmor frequency and be separated along the antidiagonal according to $\nu_{\alpha(\beta)} = \nu_N \pm A/2$. This is often the case when dealing with strongly coupled protons, given the large Larmor frequency. (*23*) When the opposite condition, $|T+2a| > 4\nu_N$, is true, the hyperfine peaks will appear in the (-,+) quadrant and the location of the two cross peaks is described by $\nu_{\alpha(\beta)} = A/2 \pm \nu_N$ (the peaks are centered on $A/2$ instead of ν_N).

In both cases, $|T+2a| < 4\nu_N$ and $|T+2a| > 4\nu_N$, it is easy to read a value for *A*, which is typically equal to the largest component of the hyperfine tensor ($a + 2T$ in the case of an axially symmetric tensor). When the hyperfine coupling is on the same scale as the Larmor frequency, a value of *A* can be obtained by finding the maximums of the two peaks and locating their center. This is a simple matter of adding the value of the

two coordinates of one of the peaks. In contrast, when the Larmor frequency is significantly larger than the hyperfine coupling, *A* is obtained from the separation of the two maxima. In the (+,+) quadrant *A* is approximately half the difference between the two coordinates. (Both types of calculations will be utilized in Chapter 4.)

When the Larmor frequency is significantly large, *A* may not be obtainable in this manner. This is the case for ^{1}H nuclei, with the Larmor frequency of ~14.7 MHz at X-band. The proton Larmor frequency causes the peaks to be located far from the origin and results in broadening of the features into ridges, often without clear maxima. However, a straightforward method of analysis has been developed to relate the shapes of these ridges to the isotropic and anisotropic contributions to the hyperfine tensor. In a HYSCORE spectrum, the cross correlations consist of coordinates at frequencies ($\nu_{\alpha(\beta)}$, $\nu_{\beta(\alpha)}$) that represent the set of nuclear frequencies in each electron spin manifold, m_S = ±½,. Points along the ridges can be chosen and their coordinates ($\nu_{\alpha(\beta)}$, $\nu_{\beta(\alpha)}$) plotted as ν_α^2 versus ν_β^2. The plot obeys the relationship in Equation 11.

$$\begin{aligned} \nu_\alpha^2 &= Q_\alpha \nu_\beta^2 + G_\alpha \\ Q_\alpha &= \frac{T + 2a - 4\nu_N}{T + 2a + 4\nu_N} \\ G_\alpha &= 2\nu_I \left(\frac{4\nu_N^2 - a^2 + 2T^2 - aT}{T + 2a + 4\nu_N} \right) \end{aligned} \qquad (11)$$

The form of Eqn 11 indicates that a plot of ν_α^2 versus ν_β^2 will be a straight line with a slope of Q_α and intercept of G_α. (*23*) The solutions for the values of the isotropic and anisotropic constants (*a* and *T*, respectively) can be visualized by plotting $|\nu_\alpha + \nu_\beta| = 2\nu_N$ on the same axis as ν_α^2 versus ν_β^2. The points where the two plots intersect indicate the

two potential solutions, which can also be obtained by directly solving for *a* and *T* in Eqn 11. The result is two possible solutions of *a* and *T* couplings with the same value of $|2a+T|$ and two possibilities for $A_{\perp}=|a-T|$ and $A_{\parallel}=|a+2T|$.[3] (Figure 3.8)

In samples with pronounced quadrupole features attributable to ^{14}N nuclei, isotopic labeling with ^{15}N can provide a significant analytic advantage by adding spin I = ½ information for comparison. When ^{15}N nuclei participate in the electronic structure of the paramagnetic center, the hyperfine coupling is typically on the order of the Larmor frequency ($^{15}\nu_N \approx 1.4$ MHz at X-band). Under these circumstances the cross peaks can be expected to appear in either the (-,+) or (+,+) quadrant. Due to the relatively small Larmor frequency of the ^{15}N nucleus, the ridges will be close to the origin and compact (relative to ^{1}H), and the value of *A* is relatively easy to read from the peak maxima. The anisotropic component can often be read from the extremes of the cross feature shapes. (*24*) The same type of analysis presented in Equation (11) is still valid for ^{15}N, but it is rarely required and is often more difficult given the lack of extended cross ridges. Despite the ability to directly read the values of *a* and *T* from the spectrum, often the best way to determine the hyperfine tensor is to simulate the spectrum. There are computational packages available for free to perform this type of analysis. (*30, 31*)

[3] In this work, $A_{\perp}=|a-T|$ and $A_{\parallel}=|a+2T|$. However, there is no reason that the perpendicular component could not be the largest component of the hyperfine tensor. They are defined this way here because this is the case for RC semiquinones.

References

1. Wertz, J. E., and Bolton, J. R. (1972) *Electron Spin Resonance: Elementary Theory and Practical Applications*, McGraw-Hill Inc, United States of America.
2. Hagen, W. (2009) *Biomolecular EPR Spectroscopy*, CRC Press, Boca Raton, FL.
3. van den Brink, J. S., Spoyalov, A. P., Gast, P., van Liemt, W. B. S., Raap, J., Lugtenburg, J., and Hoff, A. J. (1994) Asymmetric binding of the primary acceptor quinone in reaction centers of the photosynthetic bacterium *Rhodobacter sphaeroides* R26, probed with Q-band (35 GHz) EPR spectroscopy, *FEBS Letters 353*, 273-276.
4. Lubitz, W., and Feher, G. (1999) The primary and secondary acceptors in bacterial photosynthesis III. Characterization of the quinone radicals Q_A^- and Q_B^- by EPR and ENDOR, *Appl. Magn. Reson. 17*, 1-48.
5. Dutton, P. L., Leigh Jr, J. S., and Reed, D. W. (1973) Primary events in the photosynthetic reaction centre from *Rhodopseudomonas spheroides* strain R26: Triplet and oxidized states of bacteriochlorophyll and the identification of the primary electron acceptor, *Biochim. Biophys. Acta 292*, 654-664.
6. Feher, G. (1998) The primary and secondary electron acceptors in bacterial photosynthesis: I. A chronological account of their identification by EPR, *Appl. Magn. Res. 15*, 23-38.
7. Feher, G. (1971) Some chemical and physical properties of a bacterial reaction center particle and its primary photochemical reactants, *Photochem. Photobiol. 14*, 373-387.
8. Loach, P. A., and Hall, R. L. (1972) The question of the primary electron acceptor in bacterial photosynthesis, *Proc. Natl. Acad. Sci. USA 69*, 786-790.
9. Tiede, D. M., and Dutton, P. L. (1981) Orientation of the primary quinone of bacterial photosynthetic reaction centers contined in chromatophore and reconstituted membranes, *Biochim. Biophys. Acta 637*, 278-290.
10. Utschig, L. M., Greenfield, S. R., Tang, J., Laible, P. D., and Thurnauer, M. C. (1997) Influence of iron-removal procedures on sequential electron transfer in photosynthetic bacterial reaction centers studied by transient EPR spectroscopy, *Biochemistry 36*, 8548-8558.
11. Isaacson, R. A., Lendzian, F., Abresch, E. C., Lubitz, W., and Feher, G. (1995) Electronic structure of Q_A^- in reaction centers from *Rhodobacter sphaeroides*. I. Electron paramagnetic resonance in single crystals, *Biophys. J. 69*, 311-322.
12. Feher, G., Okamura, M. Y., and McElroy, J. D. (1972) Identification of an electron acceptor in reaction centers of *Rhodopseudomonas spheroides* by EPR spectroscopy, *Biochim. Biophys. Acta 267*, 222-226.
13. Nimz, O., Lendzian, F., Boullais, C., and Lubitz, W. (1998) Influence of hydrogen bonds on the electronic g-tensor and ^{13}C-hyperfine tensors of ^{13}C-labeled ubiquinones — EPR and ENDOR study, *Appl. Magn. Res. 14*, 255-274.
14. Morton, J. R., and Preston, K. F. (1978) Atomic Parameters for Paramagnetic Resonance Data, *J. Magn. Res. 30*, 577-582.

15. Feher, G. (1956) Observation of nuclear magnetic resonances via the electron spin resonance line, *Phys. Rev. 103*, 834.
16. Flores, M., Isaacson, R., Abresch, E., Calvo, R., Lubitz, W., and Feher, G. (2007) Protein-cofactor interactions in bacterial reaction centers from *Rhodobacter sphaeroides* R-26: II. Geometry of the hydrogen bonds to the primary quinone formula by ^{1}H and ^{2}H ENDOR spectroscopy., *Biophys. J. 92*, 671-682.
17. Flores, M., Isaacson, R., Abresch, E., Calvo, R., Lubitz, W., and Feher, G. (2006) Protein-cofactor interactions in bacterial reaction centers from *Rhodobacter sphaeroides* R-26: I. Identification of the ENDOR lines associated with the hydrogen bonds to the primary quinone Q_A^-, *Biophys. J. 90*, 3356-3362.
18. Mims, W. (1972) Electron spin echoes, In *Electron Paramagnetic Resonance* (Geschwind, S., Ed.), p 263, Plenum Presss, New York.
19. Dikanov, S. A., and Tsvetkov, Y. D. (1992) *Electron spin echo envelope modulation (ESEEM) spectroscopy* CRC Press, Boca Raton.
20. Hahn, E. (1950) Spin Echoes, *Phys. Rev. 80*.
21. Schweiger, A., and Jeschke, G. (2001) *Principles of pulse electron paramagnetic resonance*, Oxford University Press, Oxford, UK.
22. Rowan, L. G., Hahn, E. L., and Mims, W. B. (1965) Electron-spin-echo envelope modulation, *Phys. Rev. 137A*.
23. Dikanov, S. A., and Bowman, M. K. (1995) Cross-Peak Lineshape of Two-Dimensional ESEEM spectra in Disordered S = 1/2, I = 1/2 Spin Systems, *J. Magn. Res. A 116*, 125-128.
24. Stoll, S., Calle, C., Mitrikas, G., and Schweiger, A. (2005) Peak suppression in ESEEM spectra of multinuclear spin systems, *J. Magn. Res. 177*, 93-101.
25. Hofer, P., Grupp, A., Nebenfuhr, H., and Mehring, M. (1986) Hyperfine Sublevel Correlation (HYSCORE) Spectroscopy: A 2D ESR Investigation of the Squaric Acid Radical, *Chem. Phys. Lett 132*.
26. Dikanov, S. A., Tsvetkov, Y. D., Bowman, M. K., and Astashkin, A. V. (1982) Parameters of quadrupole coupling of ^{14}N nuclei in chlorophyll a cations determined by the electron spin echo method, *Chem. Phys. Lett. 90*, 149-153.
27. Flanagan, H. L., and Singel, D. J. (1987) Analysis of ^{14}N ESEEM patterns of randomly oriented solids, *J. Chem. Phys. 87*, 5606.
28. Dikanov, S. A., Holland, J. T., Endeward, B., Kolling, D. R. J., Samoilova, R. I., Prisner, T. F., and Crofts, A. R. (2007) Hydrogen bonds between nitrogen donors and the semiquinone in the Q_i-site of the bc_1 complex, *J. Biol. Chem. 282*.
29. Jiang, F., McCracken, J., and Peisach, J. (1990) Nuclear Quadrupole Interaction in Copper(II)- Diethylenetriamin-Substituted Imidazole Complexes and in Copper (II) Proteins, *J. Am. Chem. Soc. 112*.
30. Epel, B., and Silakov, A. (2007) Kazan Viewer
31. Stoll, S., and Schweiger, A. (2006) EasySpin, a comprehensive software package for spectral simulation and analysis in EPR, *J. Magn. Res. 178*, 42-55.

Figures

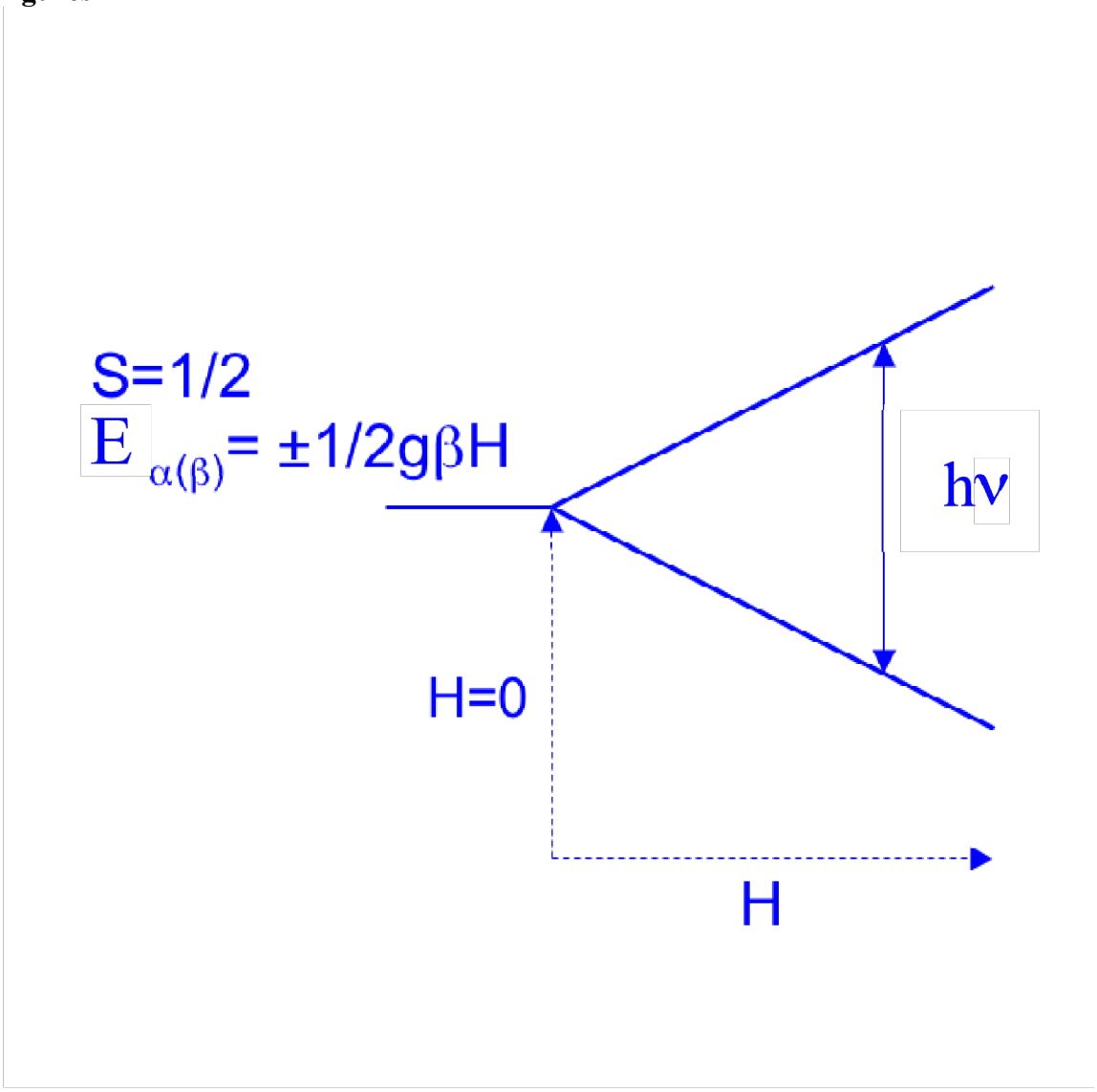

Figure 3.1. Scheme of Zeeman splitting as a function of increasing magnetic field. In an EPR spectrometer the microwave frequency is constant and at X-band $\nu \sim 9.5$ GHz.

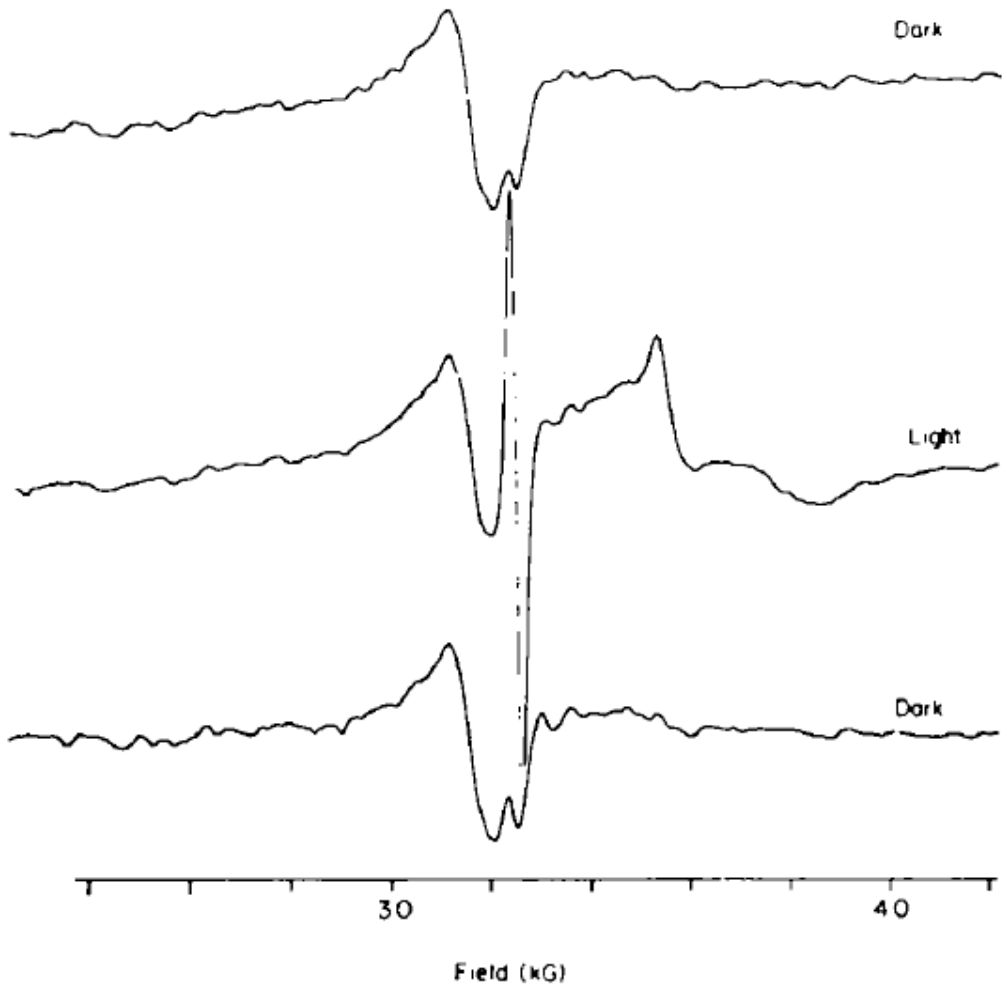

Figure 3.2. The original X-band EPR signal showing a narrow peak attributable to the oxidized donor and a wide peak from the Fe-Q couple (from Dutton et al. 1973 (5)). This spectrum is a first derivative signal at 32 G modulation and 50 mW microwave power. These are very high values of microwave power and modulation compared to what is typically used to observe a free radical signal (~0.5-5 G modulation and 0.1 mW microwave power).

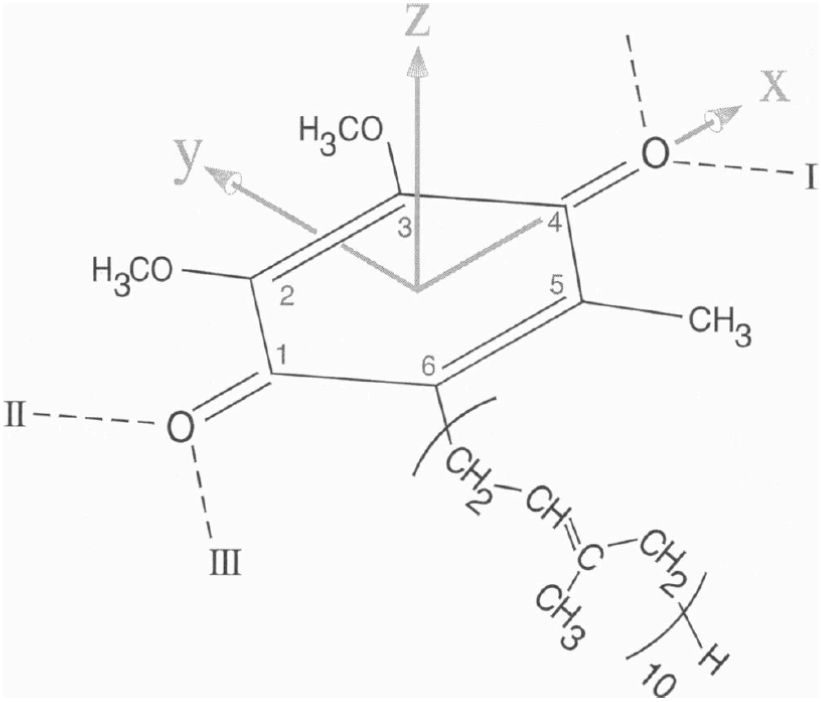

Figure 3.3. A ubiquinone-10 molecule with carbons 1-6 labeled. The molecular axes are defined with the z component perpendicular to the plane of the quinone headgroup, the x component along the quinone carbonyls, and y normal to the x and z axis. (4)

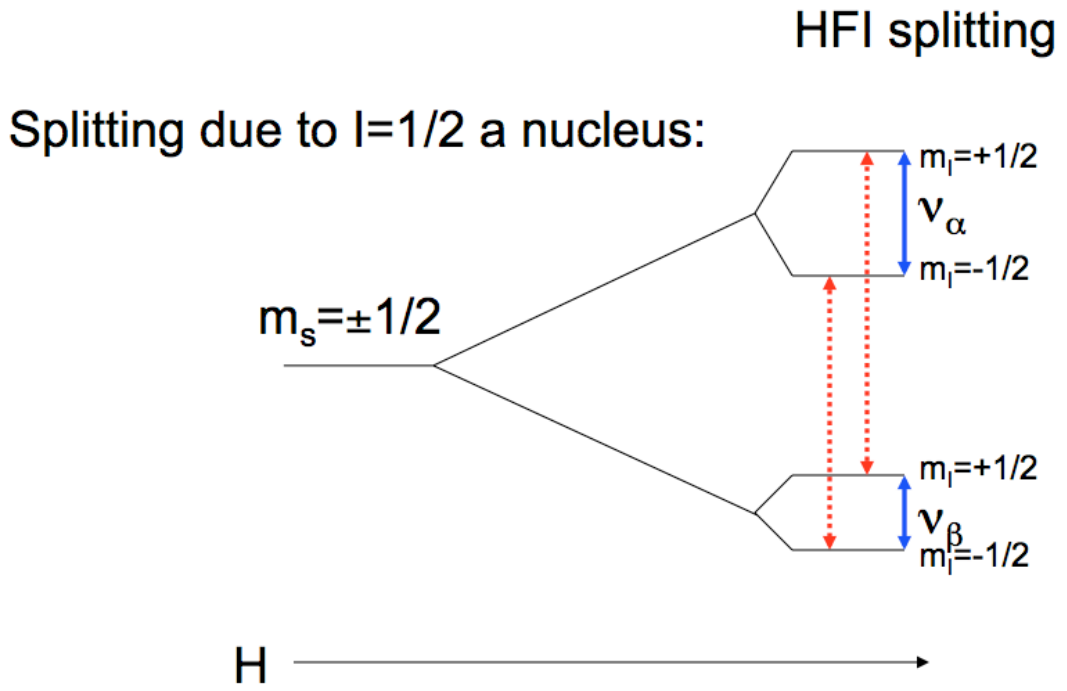

Figure 3.4. The nuclear spin (I = ½ shown here) generates two sets of EPR transitions indicated by red dotted lines based on the nuclear α and β spin manifolds (solid blue arrows). The different magnitude of the α and β spin transitions reflects the impact of the magnetic field "H" on the nuclear spins.

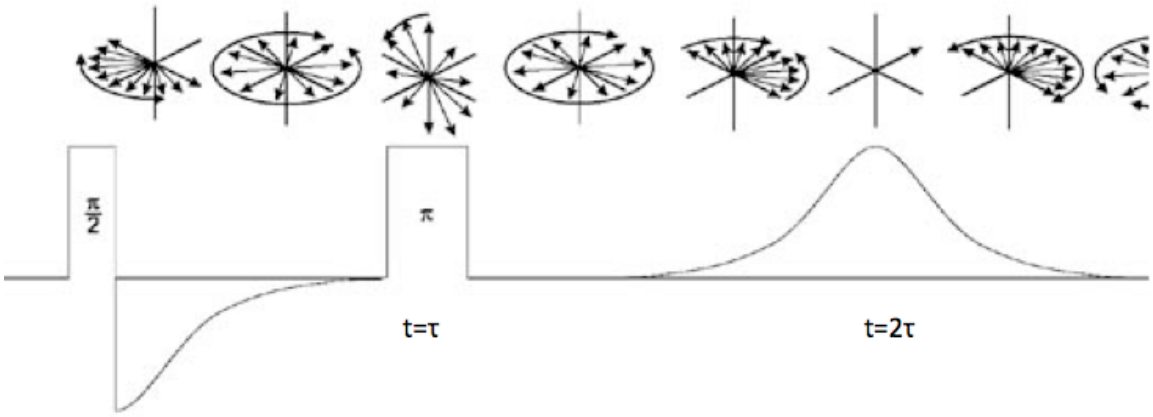

Figure 3.5. The progression of the magnetization vectors after π/2 and π pulses. The curves show free induction decay and the spin echo that represents spontaneous generation of microwaves. (Reproduced from www.bruker-biospin.com)

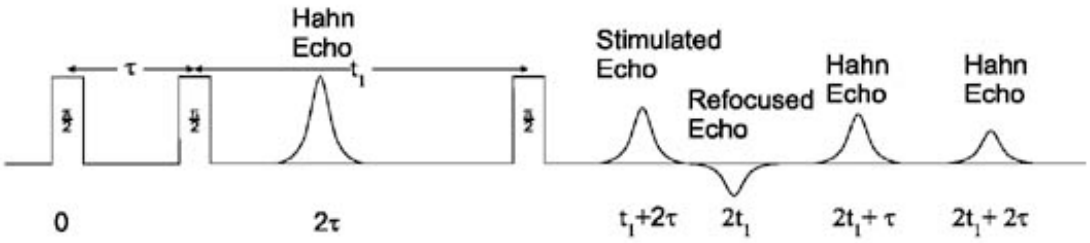

Figure 3.6. A 3-pulse ESEEM sequence, and the five spin echoes forming from combinations of the three pulses. Each echo will appear at well defined times that are a combination of the pulse times t_1 and τ. (reproduced from www.bruker-biospin.com)

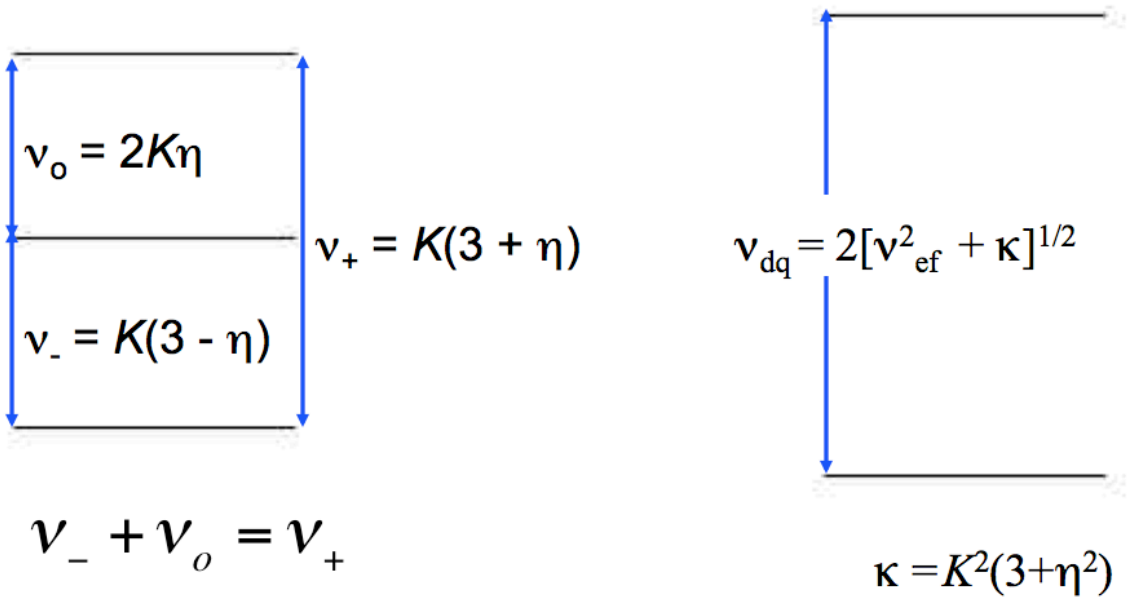

Figure 3.7. The NQI transitions from the spin manifolds S = 1/2 and S = -1/2 are shown above. In this case, the HFI cancels in the S = ½ manifold generating the zero field NQI transitions. In the S = -1/2 manifold the observed transition is the double quantum I = -1 to I =1 transition.

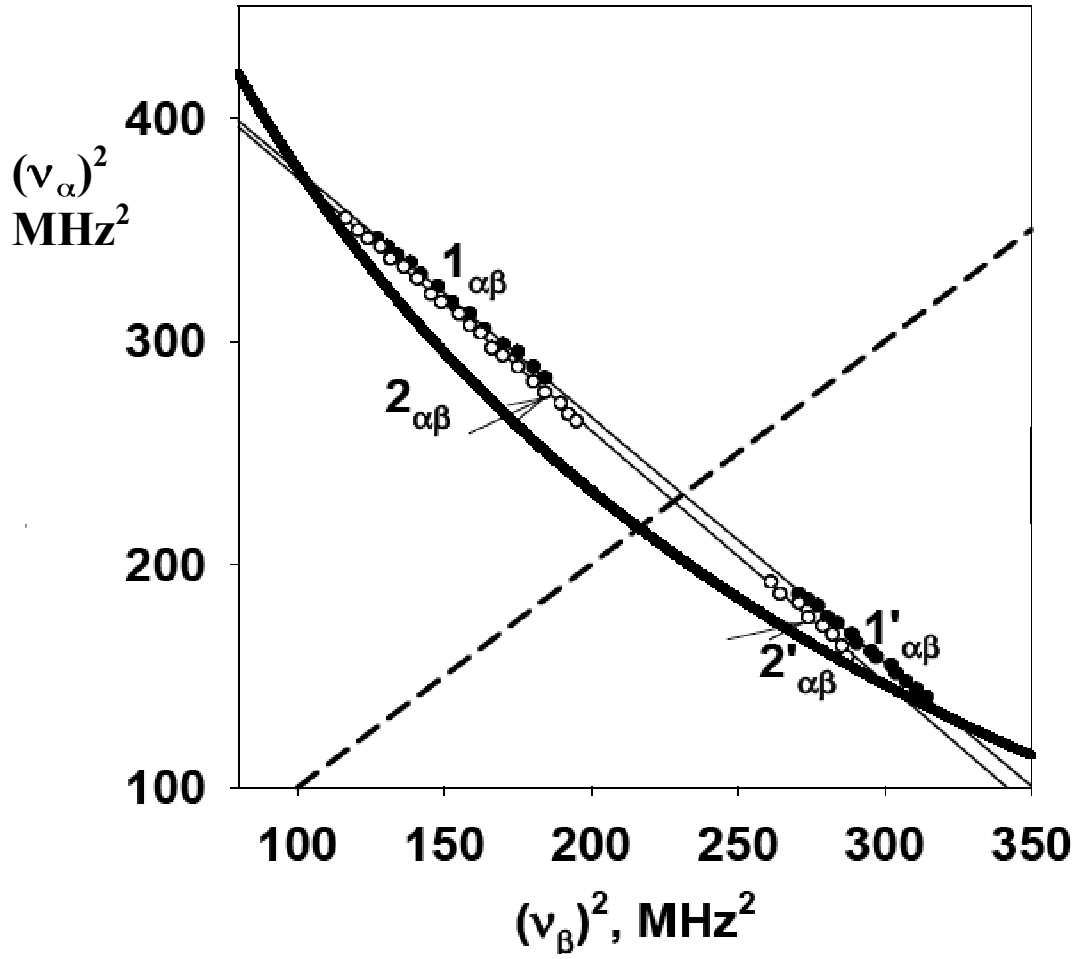

Figure 3.8. The coordinates of points chosen along HYSCORE ridges were assigned to ν_α and ν_β and were plotted as ν_α^2 versus ν_β^2. The curved line is $|\nu_\alpha + \nu_\beta| = 2\nu_N$ and the two intersection points with the lines from each ^{1}H nuclei represent potential solutions for the hyperfine coupling constants *T* and *a*.

Chapter 4:

The Structure of Nitrogen Electronically Coupled to Q_A^- and Q_B^- - Computational and Pulsed EPR Studies

Abstract

RC crystal structures suggest that the majority of H-bond donors to Q_A and Q_B are either backbone amide NH or histidine Nδ. Some of these H-bonds, particularly in the Q_A site, have been examined in detail by proton ENDOR. However, information about the nitrogen donors is still quite sparse. 3-pulse ESEEM and HYSCORE are used here to examine nitrogen nuclei coupled to both RC semiquinones. NQI parameters K and η are calculated for two nitrogens coupled to each quinone. These parameters are analyzed in terms of external sp^2 orbital occupancy and H-bond character. HFI are measured from ^{15}N HYSCORE measurements and are used to discuss the nature of spin densities transferred through H-bonding.

Introduction

The cofactors responsible for the electrochemistry of photosynthetic reaction centers have been reasonably well characterized, and for this reason it is an ideal system to examine the nature of electron transfer reactions. Interplay between the protein and redox cofactors generates the specific properties required for sequential electron transfer. While the structures of the quinone electron acceptor binding sites are quite well defined by X-ray crystallography, these structures provide little insight into the electronic environment of the quinones. (*1*) Ambiguity in RC electronic structure could arise from structural features below the resolution of crystal structures, non-physiological conformations formed due to crystallization conditions, or simply electrostatics not immediately apparent from structural examination alone. High resolution pulsed EPR techniques can be used to locate which nuclei the Q_A^- and Q_B^- semiquinones are coupled to, to what degree spin density is exchanged between the semiquinone and the environment, and what effects these have on the electronic structure of the semiquinones and quinone binding pockets.

The Q_A and Q_B sites in the reaction center (RC) of *Rb. sphaeroides* are both occupied by ubiquinone-10 (UQ-10), i.e., Q_A and Q_B are chemically identical. X-ray structures of the *Rb. sphaeroides* RC have provided valuable information about the position of UQ-10 in both quinone-binding sites. (*1, 2*) Despite the very different

chemistry, the structures reveal a number of substantial similarities in the hydrogen bonding patterns of the Q_A and Q_B sites. In both cases, the quinone carbonyl oxygens, O1 and O4, appear to form hydrogen bonds with an amide NH from the protein backbone and with one of the Fe^{2+}-liganded histidine residues. (See Chapter 1, Figure 1.2) The O4 carbonyl of Q_A forms a strong hydrogen bond with the Nδ of His-M219 and a similar bond exists between Q_B and Nδ of His-L190. The heavy atom distances of these interactions are similar with a span of 2.80 ± 0.15 Å between the Q_A carbonyl and His-M219, and 2.69 ± 0.23 Å between the Q_B carbonyl and His-L190. (*3*)

At the O1 carbonyl, hydrogen bonds are presumed to exist between the quinones and peptide nitrogens. In the Q_A site, the crystal structures show the hydrogen bond donor to be the alanine M260 backbone, with a heavy atom distance of 2.79 ± 0.09 Å. The Q_B binding site at the O1 carbonyl is a bit more ambiguous. A hydrogen bond is likely between the carbonyl and backbone amide nitrogen. However, the peptide NH of both L224 and L225 are at possible H-bonding distances of 2.91 ± 0.24 Å and 3.09 ± 0.16 Å respectively, (*3-5*)[1] and it can be inferred that Q_B could form a hydrogen bond with either of these residues, or possibly both. (See Chapter 1, Figures 1.1-4 for RC structures)

While the distances measured in crystal structures suggest the possibility of strong hydrogen bonding interactions between the semiquinone carbonyls and NH donors, more direct evidence comes from FTIR and EPR spectroscopy. (*6-8*) In the case of Q_A, the FTIR and EPR data verify this supposition and show a distinct asymmetry in the quinone binding site, implying that the interaction with M219 is much stronger than with M260.

[1] Molecular dynamic relaxation of the protein structure suggests even greater similarity with nearly identical distances, ~2.8 Å.

(*6, 9*) Unlike in the case of Q_A, similar studies on the electronic structure of Q_B^- indicate that it is significantly more symmetric.

Q_A site EPR Spectroscopy and Coupled Nitrogen

The Q_A site has been extensively studied using the double resonance technique, ENDOR, in a wide variety of conditions and at multiple frequencies to identify nuclei coupled to the semiquinone. (*6*) A generally accepted shortcoming of ENDOR is its inherent insensitivity to low frequency couplings. (*10*) Thus the existing ENDOR data have provided a good description of the proton environment, but specific parameters of coupled nitrogens are still vague. Previous ESEEM studies on the Q_A site supported the identity of the hydrogen bonding partners - Nδ from His-M219 and a backbone N presumably from Ala-M260. (*7, 11*) However, these studies, based on 1D ESEEM techniques, relied on a small sampling of pulse timing schemes and provide only a basic picture of nitrogen coupling.

Using both 1D 3-Pulse ESEEM and 2D 4-pulse HYSCORE, along with uniform ^{15}N labeling, we have refined the knowledge of the Q_A^- coupling to surrounding nitrogen nuclei and the electronic structure of the Q_A site. Cross correlations in HYSCORE spectra make the location and identification of peaks more precise, and for ^{14}N this precision is carried through to calculated nuclear quadrupole interaction (NQI) parameters. In particular, spin manifold correlations generated in HYSCORE provide a more precise value for the spin I = -1, I = 1 double quantum (dq) transition, allowing estimation of the hyperfine coupling constant. Uniform ^{15}N labeling eliminates NQI transitions from the spectra and allows for direct measurement of the hyperfine

interaction (HFI). NQI parameters are directly related to the electric field gradient tensor at the coupled nitrogen, while hyperfine coupling strength is related to the transfer of spin density between the semiquinone and the coupled nitrogen, and magnetic dipole-dipole interactions.

Q_A^- sample generation

For ESEEM and HYSCORE measurements, the Q_A^- semiquinone anion must be generated with high enough concentration to obtain a good signal – as the complexity of the pulse sequence increases so must the concentration of paramagnetic species. Following photoexcitation of the primary donor, the RC can be trapped in the Q_A^- state by blocking the Q_B site with an inhibitor (terbutryn or stigmatellin are commonly used) and allowing a molecule, such as cytochrome *c*, with sufficiently low redox potential to rereduce the primary donor. Alternatively, the quinone can be reduced chemically with a powerful reducing agent. Photo-trapping the semiquinone would be preferred, but yields in these preparations are smaller by nearly a half compared to those in chemically generated samples. (Figure 4.1) Differences were identified in EPR spectra between chemically generated and phototrapped samples. However, the differences seem to be limited to protein relaxation in response to semiquinone formation and are only visible in time-resolved experiments and disappear very rapidly. (*12*) When examining the steady state, chemical reduction is sufficient.

Reaction centers for EPR and ESEEM experiments were isolated from his-tagged 2.4.1 type cells (*13*) as outlined in Chapter 2, and concentrated to ~200 μM in Amicon Ultra-15 centrifugal concentrators with 30,000 Da MW cutoff (Fisher Scientific Cat #UFC9-030). The native high spin Fe^{2+} was replaced with Zn^{2+} by the methods described

in detail in Chapter 2. Generally 10% glycerol was added to samples as a cryoprotectant - in the absence of glycerol sample tubes often shatter when frozen - but the concentration was kept at a minimum so as to not dilute the samples. The anion was generated chemically by adding 8 mM Na-dithionite to the sample followed by immediate freezing in liquid nitrogen. Na-dithionite was added from a freshly prepared 128 mM stock in 1M Tris buffer at pH 7.9 (unless otherwise indicated). All buffers and RC samples were bubbled with nitrogen or argon in order to increase the efficacy of the dithionite reduction. Samples have also been prepared in an anaerobic cell while measuring the redox potential, to ensure complete Q_A reduction. However, once it was determined that 8 mM Na-dithionite was sufficient, redox measurements were no longer taken. To prevent any precipitation resulting from reduction of the detergent LDAO, used in the isolation and metal exchange procedures, samples were exchanged for the detergent Triton X-100 by a single, approximate 50 fold, dilution and reconcentration via Amicon Ultra-15 centrifugal concentrators at 4^0C.

The EPR spectrum of the Q_A^- semiquinone was measured with both X- and Q-band continuous wave (CW) EPR. X-band measurements were used primarily to assay signal quality, while Q-band measurements allow for resolution of the components of the g-tensor and can positively identify the presence of a RC-bound semiquinone. CW EPR measurements were performed at X-band on a Varian EPR-E122 spectrometer with an Air Products variable temperature cryostat. For Q-band measurements, a Bruker ELEXSYS E580 was equipped with a Q-band microwave bridge and Oxford CF935 cryostat. Both X and Q-band instruments operate at 100 kHz modulation frequency. Pulsed EPR measurements were carried out using the Bruker ELEXSYS E580

spectrometer fitted with an X-band cavity and an Oxford CF935 cryostat. X-band CW EPR spectra were collected at ~15 K while Q-band CW EPR and pulsed X-band experiments were performed at ~70 K.

CW EPR Spectroscopy of Q_A^-

The CW EPR properties of the primary acceptor quinone have been extensively examined and are now well characterized. (*6, 14-17*) The first measurements of the g-value for Q_A^- were obtained at X-band showing a line centered at 2.0046 with a linewidth of ~8.1 Gauss.(*18, 19*) At X-band, the semiquinone signal is nearly symmetric and the linewidth is sufficiently broadened that no information is present in these spectra about the components of the g-tensor.

The g-tensor exhibits near axial symmetry and at Q-band parallel and perpendicular components can be resolved as $g_{||}$ = 2.0022 and $g_{\perp}$ = 2.0059 (and the complete tensor has been measured in single crystals: g_z= 2.0022, g_y= 2.0054 and g_x= 2.0066). (*15, 20*) These parameters are a good basis for assaying the quality of our samples prior to measurement with more methodologically complicated pulsed EPR experiments.

2D nitrogen (^{14}N) HYSCORE spectra, presumed to originate from the Q_A^- semiquinone, were very cluttered (see Figure 4.4). It is possible to analyze these spectra based on the assumption that the signal arises from a semiquinone coupled to multiple nitrogen nuclei, but it was not immediately obvious that the spectra reflected a single paramagnetic species, i.e., Q_A^- alone. While Q-band EPR would not distinguish between

RC quinones, the spectra did confirm that RC-bound semiquinones were the only signals present. (Figure 4.2)

Table 4.1. Semiquinone g-tensor measured from Q-band CW EPR on "wild type" reaction centers

	pH 9.0	**pH 7.9**
g_x	2.0066	2.0066
g_y	2.0056	2.0056
g_z	2.0022	2.0024

Comparison of the values in Table 4.1 with the literature values (g_z= 2.0022, g_y= 2.0054 and g_x= 2.0066) indicate that, despite its apparent complexity, the 2D HYSCORE spectrum is attributable only to RC-bound semiquinone(s).

1D 3-Pulse ESEEM of the Q_A^-

The 1D ESEEM spectrum of Q_A^- has been reported by Bosch et al. (*7*) and Spoyalov et al. (*11*) However, these studies leave significant uncertainties with regards to the measured quadrupole parameters and estimates of hyperfine coupling. In particular, only long pulse delay times, τ, were utilized. To ensure that the data were complete and reproducible over a large range of τ, it is valuable to create a quasi-2D ESEEM spectrum by stacking sequential τ values. This type of representation unmasks τ dependent suppression effects and accentuates true peaks. In order to incorporate significantly smaller values of τ, 3-pulse ESEEM spectra are presented stacked, beginning at 100ns

and followed by 16ns steps (measurements were also performed with a 50 ns step size to ensure that relevant features at long times were not missed).

^{14}N has a spin I = 1 and the 3-pulse ESEEM spectrum is therefore expected to be dominated by nuclear quadrupole transitions (see ESEEM section of Chapter 3). If the cancellation condition is near to met, these quadrupole transitions will be manifest in the spectrum as a sharp triplet, from which the NQI resonance parameters, the coupling constant ($K= e^2q_zQ/4h$) and the asymmetry parameter (η), can be easily calculated. (*21*) Both of these values are dependent on the electric field gradient (EFG) tensor, the components of which are, by convention, chosen such that $|q_{zz}| > |q_{yy}| > |q_{xx}|$ (the primary diagonal of the traceless 3x3 EFG matrix). *K* is dependent on the quadrupole moment and the zz component of the EFG tensor. The asymmetry parameter is given by $|(q_{yy} - q_{xx})/q_{zz}|$, and ranges from 0 to 1.

Our 3-pulse ESEEM spectra show two sets of peaks. (Figure 4.3) The most intense are a pair at ~0.75 MHz and 1.5 MHz. The low frequency peak is likely the overlapping peaks from the ν_o and ν_- NQI transitions. When the low frequency transitions overlap, the quadrupole tensor exhibits near axial symmetry and it is easy to calculate the quadrupole parameters using Eqn. 1: the asymmetry parameter (η) is ~ 1, $\nu_+ = e^2q_{zz}Q/h$ =1.5 MHz, and K=0.375 MHz.

$$\nu_+ = K(3+\eta); \qquad \nu_- = K(3-\eta); \qquad \nu_o = 2K\eta \qquad (1)$$

Also resolved in the stacked 3-pulse representation is a second, weaker, set of peaks at ~1 MHz, 1.8 MHz, and 2.8 MHz. Even though these peaks don't exhibit the

nearly ideal axial symmetry of the first triplet described they do appear to be close to cancellation, with $\nu_o + \nu_- = \nu_+$, and calculating the NQI resonance transitions is again done using Eqn. 1. For the second triplet, nqcc K= 0.766 MHz and η= 0.63.

2D HYSCORE of the Q_A semiquinone

A HYSCORE spectrum provides the same information as a 3-pulse ESEEM spectrum but with greater precision and resolution. However, spreading the spectrum into two dimensions can result in cluttering. Thus, particularly when examining spectra with complicated quadrupole features, it is valuable to combine knowledge from 3-pulse ESEEM and HYSCORE. HYSCORE can resolve peaks missing from a 3-pulse ESEEM spectrum and allow for positive identification of peaks associated with the same nucleus, while the 3-pulse ESEEM spectrum can provide values for quadrupole transitions in a simpler, easy to identify, format. The 3-pulse spectra of the Q_A^- semiquinone showed two distinct triplets attributable to quadrupole transitions, indicating cancellation conditions are exactly or near to being met. In this case it is expected that the HYSCORE spectrum will show correlations between NQI transitions ν_o, ν_+, ν_-, in one manifold and the double quantum transition from the other.

In ^{14}N ESEEM, where NQI transitions dominate the spectrum, a value for the hyperfine coupling can still be calculated by exploiting the relationship $\nu_{ef\pm} = \nu_N \pm A/2$ and Equation 2.(*22*)

$$\nu_{dq^\pm} = 2[\nu^2_{ef^\pm} + \kappa\,]^{1/2} \qquad (2)$$

$$\kappa = K^2(3+\eta^2).$$

HFI values of ^{14}A~2 MHz for the histidine nitrogen and ^{14}A~1.4 MHz for the peptide nitrogen are calculated. (Figure 4.4) However, these values rely on the assumption of perfect cancellation and axial symmetry, and there are indications in the HYSCORE spectrum that complete cancellation did not exist. Particularly, curvature in the ridges and additional cross-ridges, perhaps indicating dq-dq correlations, show there is some departure from perfect cancellation. The extent of the errors in HFI estimated from NQI parameters is difficult to estimate, and it is most prudent to directly measure hyperfine couplings.

Uniform labeling of reaction centers with ^{15}N (I= ½) eliminates NQI transitions from the spectrum. HYSCORE spectra from ^{15}N labeled samples show lines attributable to two separate nitrogen nuclei. From these peaks it is possible to directly read the values of HFI. (Figure 4.5) ^{15}N labeled reaction center HYSCORE shows two pairs of cross-peaks at (+/-3.24, -/+0.35) MHz in the (-,+) quadrant, and (2.83, 0.32) MHz in the (+,+) quadrant. The ^{15}N HFI for these two cross-peaks are 3.57 and 2.68 MHz respectively.[2] The different relationships between the peaks and the hyperfine splitting is discussed in detail in Chapter 3. The complete tensor can be read[3] as a=3.4 and T=(1.0, -0.3, -0.7) for one set of peaks and a=2.53 and T=(-0.8,0.13,0.67). The corresponding HFI scaled for ^{14}N nuclei are 2.55 and 1.91 MHz (^{14}N HFI is 1.4 times smaller than that for ^{15}N).

---

[2] The mathematical treatment to obtain A is different for the two sets of coordinates because they fall in different quadrants. In the (-,+) quadrant the two peaks are centered on the coordinate (A/2, A/2). Thus, $A=\nu_1+\nu_2$, i.e., (3.24+0.35) = 3.57 In the (+,+) quadrant, the peaks are centered on the coordinate (ν_N , ν_N) and are separated by A/2 and $A=\nu_1-\nu_2$. In the case of our data, the (+,+) quadrant was not as well resolved and A was calculated as $(\nu_1-\nu_N)*2$, where ν_1 is the larger frequency, i.e., (2.8-1.49)*2 = 2.68.

[3] The crosspeak shape will span between frequencies for parallel and perpendicular components of the tensor. By measuring the edges of the cross features, the tensor can be estimated. Of course the exact shape of the peaks will be affected by suppression effects and this method is not nearly as accurate as spectral simulation.

The HFI values calculated from ^{14}N NQI lines and double quantum transitions (2 MHz and 1.4 MHz) are significantly different from those scaled from the ^{15}N HYSCORE spectrum. This result is not surprising given suspicion that the cancellation condition was not met, causing imprecision in the estimated hyperfine parameters. Additionally, intrinsic differences in line maxima between ^{14}N and ^{15}N nuclei can account for significant differences between HFI values. Nevertheless, the presence of the two nitrogen nuclei with different values of HFI is in good agreement with the ENDOR results, which show a similar asymmetry in proton HFI.(*6*)

One severe limitation in the current analysis of Q_A site ESEEM and HYSCORE data is an inability to accurately simulate the spectra. This limits the amount of information that can be obtained from NQI parameters and HFI values read from the spectra. Although these parameters are often straightforward to obtain directly, as discussed in Chapter 3, simulation is the best way to analyze spectra from ^{15}N nuclei, particularly when attempting to obtain the anisotropic components of the HFI tensor. While the shape of crossridges in ^{15}N HYSCORE and the location of peaks in ^{14}N 3-pulse ESEEM can be simulated, the significant difference in intensities so far can't be computationally modeled. Similar differences in intensity are present in ENDOR data and were interpreted as evidence of asymmetry in the binding pocket.(*6*) In an ESEEM spectrum, a relatively weaker H-bond would be expected to have a smaller value for HFI, as seen in our samples. However, attempts to simulate the spectra with measured values of NQI and HFI have not reproduced a decrease in peak amplitude with a decrease in HFI.

The simplest explanation is that there is an interaction between the two nuclei coupled to the semiquinone. Current simulations methods treat individual coupled nuclei separately and create a composite spectrum by summing multiple simulations of a nuclear spin with a single m_s=1/2 electron. For simulations of Q_B^- spectra (below), differences in peak intensities can be explained by adding rhombicity to the anisotropic tensor, but the intensity differences seen in Q_A^- spectra are too great and this method has not been successful. However, new simulation techniques, which can account for the whole system and allow for independently defined hyperfine tensors in the same simulation, have shown promise.(*23, 24*)

It is also possible that the issue might have a structural origin. Asymmetric spin density distribution over the quinone might result in incomplete or transient coupling between the backbone and the semiquinone. However, current QM and MD calculations, performed to accompany the ESEEM and HYSCORE presented here, have been unable to detect this phenomenon. HYSCORE spectra taken at different pH values occasionally, but not repeatably, showed a decoupling between the semiquinone and the peptide nitrogen. These measurements could imply that the hydrogen bond to Ala-M260 is not always present.

Q_B site EPR Spectroscopy and Coupled Nitrogen

X-ray crystallography provided a good model for the structures of the reaction center quinone binding sites.(*1*) While the Q_A binding site presents little ambiguity as to the orientation of the quinone or potential hydrogen bonding partners, the structure of the Q_B site is more suspect. Q_B has been seen to occupy two separate locations, proximal and

distal to the Fe-His complex.(*5, 25*) Electrons cannot be transferred to the quinone in the distal position and the degree of occupancy of this site is the subject of debate.(*5, 26*) The active, proximal conformation shows a hydrogen bond between the O4 carbonyl and His-L190 Nδ, analogous to that between O4 of Q_A and His-M219. However, hydrogen bonds at the O1 carbonyl of Q_B could be attributed to the backbone at residues L224 or L225, or both. Additional hydrogen bonds have been proposed between the OH group of Ser-L223 and the O1 carbonyl and between Thr-L226 NH and Q_B methoxy group adjacent to the O1 carbonyl.(*25, 27-29*)

Given the lack of clarity of the structure around the Q_B semiquinone, much benefit could be obtained by EPR spectroscopy. However, there is currently significantly more and higher quality data reported for the Q_A site than the Q_B site.(*6*) The Q_B^- g-tensor components have been obtained in deuterated Q-band studies (g_x= 2.0063, g_y= 2.0053, g_z= 2.0021) and are not significantly different from those measured for Q_A^- (g_x= 2.0066, g_y= 2.0054 and g_z= 2.0022), making identification of Q_A^- versus Q_B^- difficult by this method.(*15*) Using the axial symmetry, Q-band EPR can be used to determine components of the g-tensor, but the value is limited to identifying that the sample contains only a semiquinone radical and no significant background signals.

Examinations of nuclei coupled to the Q_B^- semiquinone are also more limited than those of the Q_A site. The vast majority of this information has been obtained by ENDOR spectroscopy, but it is largely limited to proton couplings.(*6, 26, 27*) The poor efficiency of this technique in observing couplings of nuclei with lower Larmor frequency has yielded little information about N nuclei. One 3-pulse ESEEM study of Q_B^- suggested the presence of a single coupled N nucleus, but the data had low signal to noise.(*30*)

Q_B^- sample generation

Generating EPR samples with a significant population of the Q_B^- state presents more challenges than for Q_A^- but suitable procedures have been developed. (*31, 32*) Samples for these experiments were prepared as described for Q_A^-, up to the point of chemical reduction. Even though there was no risk of detergent reduction in the subsequent procedure, LDAO was exchanged for Triton X-100 detergent to maintain consistency.

RCs were concentrated to 300-400 μM and combined with ~3 eqs of horse heart ferrocytochrome *c*, ~3 eqs of ubiquinone-10 and 10% glycerol in the EPR tubes. The Q_B^- semiquinone was then created by exposing the sample to a single flash at 532 nm using a Spectra Physics Quanta-Ray GCR-11 Nd-YAG laser[4], after which the samples were promptly frozen in liquid nitrogen.

1D 3-Pulse ESEEM of Q_B^-

In reaction center samples with natural abundance isotopes, the 3-pulse ESEEM spectrum of the Q_B semiquinone will primarily feature peaks attributable to ^{14}N NQI. However, ESEEM spectra of Q_B^- are still significantly different from those observed for the Q_A semiquinone. (Figure 4.6) The Q_B^- spectrum is dominated by a line at 1.5 MHz. At lower frequency there is a peak at ~0.3 MHz and a feature around 0.7-0.9 MHz that appears to contain overlapping peaks. At higher frequencies there is a weak peak at 2.9

[4] The laser power was measured with a Melles Griot power meter regularly to ensure proper functionality. The laser output was normally at 1.4 mW at the max power setting for a pulse width of ~10 ns.

MHz and a broad feature around 3.8 MHz. The shape of this spectrum suggests the semiquinone is coupled to more than one ^{14}N nucleus. Superficially some of these features mirror those in the Q_A^- spectrum, but the observed frequencies and intensities of these peaks are difficult to assign to two triplets and a double quantum transition (i.e.: $m_I = -1$ to $m_I = 1$).

An earlier report of the ESEEM spectrum of Q_B^- showed no significant peaks above noise levels at low frequencies, and a peak at 1.5 MHz that was assigned to ν_+ of NQI transitions at cancellation.(*30*) This assignment would suggest low frequency peaks that would sum to equal the peak at 1.5 MHz that were unresolved. However, the higher resolution spectrum in Figure 4.6, which shows overlapping peaks at 0.7-0.9 MHz and a higher frequency feature around 2.9 MHz, cast doubt on this interpretation. In particular, the peaks at frequencies lower than 1.5 MHz do not obey the $\nu_- + \nu_o = \nu_+$ relationship indicative of a NQI triplet in the cancellation condition. It is concluded that there are contributions from multiple nuclei and that, at X-band, the cancellation condition is not met for any of them. In light of this, the shape is substantially different from Q_A^- samples, making similar analysis impossible.

2D HYSCORE of the Q_B semiquinone

In the case of Q_B^-, the difficulty in interpreting the 3-pulse ESEEM spectrum makes the HYSCORE spectrum of particular value. Unlike the complicated features seen in ^{14}N HYSCORE spectra of the Q_A^- semiquinone – where NQI triplets are correlated across spin manifolds with dq-transitions – the HYSCORE spectrum of Q_B^- is very simple. (Figure 4.7) The HYSCORE spectrum exhibits two sets of off-diagonal cross

ridges in the (+,+) quadrant attributable to two nuclei. One pair of features shows a maximum at (3.96, 1.51) MHz with intense, extended ridges, while a second set of cross-peaks has lower intensity and approximately circular shape correlating frequencies of 3.86 and 2.98 MHz. These features fit the model of a system with $\nu_{ef}/K > 1$, where the expected HYSCORE spectrum will correlate double-quantum transitions from opposite spin manifolds (see Chapter 3).

Using Eqn. 2, the two double quantum transitions from each nucleus can be used to solve for the hyperfine coupling constant A and the quadrupole parameter κ. These are estimated to be ^{14}A = 1.57 MHz and κ = 0.49 MHz^2, and ^{14}A = 0.7 MHz and κ = 1.7 MHz^2 for the two sets of peaks. In the absence of the NQI triplets, values for the asymmetry parameter cannot be obtained from this data but, by varying η between 0 and 1, it is possible to obtain ranges of the quadrupole coupling constant K of ~0.35-0.40 MHz and ~0.65-0.75 MHz for the two nuclei.

Spectra from uniformly ^{15}N labeled reaction centers support the conclusion from ^{14}N spectra that two separate nitrogen nuclei are coupled to the Q_B semiquinone. These spectra show a small feature on the diagonal correlating the nitrogen Larmor frequency from both electron spin manifolds, and two pairs of cross peaks located on the antidiagonal symmetric around the central peak. (Figure 4.8) The small, on-diagonal peak is characteristic of matrix nitrogen in the weak hyperfine coupling limit. The two pairs of peaks with maxima at (2.53, 0.49) and (1.83, 1.16) can be assigned to two separate, strongly coupled nuclei. The corresponding ^{15}N hyperfine couplings of ^{15}A = 2.04 MHz and ^{15}A = 0.67 MHz can be read from these features, and these can be scaled to 1.43 MHz and 0.49 MHz, respectively, for ^{14}N.

Simulation of the ^{15}N HYSCORE spectrum of Q_B^- does not suffer from the same shortcomings present in Q_A^- and both the location and intensities of peaks are reproducible. As discussed in Chapter 3, the width and shape of the cross peaks along the antidiagonal are indicative of the maximum and minimum components of the hyperfine tensor, and simulations that match the location of the maximum intensity and width of the cross peaks provide an accurate representation of the data. Initial simulations assumed an axial hyperfine tensor ($2T$, $-T$, $-T$) and were unable to recreate the relative intensities of the crosspeaks. As values of the tensor departed from axial symmetry, approaching a fully rhombic (T, 0, $-T$) tensor, the simulations were able to mimic experiment. These simulations give values for isotropic hyperfine coupling (recalculated for a ^{14}N nucleus) of 1.5 MHz and 0.45 MHz (±0.02 MHz) in good agreement with the direct readouts above. However, the uncertainty in the symmetry of the anisotropic tensor limits precision to a range of values. As the ratio of the two smaller components, T_1/T_2, is varied between 0-1, the range of the maximum component, T_3, is ~0.3-0.5 MHz and ~0.21-0.28 MHz for the larger and smaller couplings, respectively.

Analysis of NQI Parameters for Q_A and Q_B

The quadrupole interactions between a paramagnetic center and I = 1 nuclei are described by the quadrupole coupling constant, $K = e^2q_{zz}Q/4h$, and the asymmetry parameter, $\eta = |(q_{yy} - q_{xx})/q_{zz}|$, which provide information on the strength of the quadrupole moment in the electric field gradient, and the symmetry of the electric field gradient respectively. K is exclusively variable in the z component of the electric field gradient tensor and is particularly sensitive to the bonding arrangement of the nucleus, in

this case, nitrogen. It has been experimentally determined that values of K can be related to particular nuclear species, for example, as found in hydrogen bonding partnerships with either Q_A or Q_B. (*33, 34*)

In 3-pulse spectra of the Q_A site, measurement of K is relatively trivial. The higher intensity triplet showed a value of K = 0.375 MHz, which is typical for the protonated Nδ of an imidazole.(*33, 35*) Given knowledge of the Q_A binding pocket from X-ray crystallography, the Fe ligand His-M219 is the only viable source of this nitrogen. The second, lower intensity triplet has K = 0.766 MHz and η = 0.63. These parameters are similar to those of polyglycine and triglycine (K = 0.76 and K = 0.48 for polyglycine and triglycine respectively). (*34, 36*) This is fully consistent with the conclusion from X-ray structures that this nitrogen originates from the peptide backbone of Ala-M260.

The two sets of peaks present in ^{14}N spectra of the Q_B site did not satisfy cancellation conditions and, as a result, the asymmetry parameter and quadrupole coupling constant can't be calculated from Eqn. 1. However, it was concluded that the peaks 1 and 2 in Figure 4.7 represent correlated double quantum transitions from opposite spin manifolds and κ could be calculated from Eqn. 2. In turn, ranges for K were determined as η was varied between 0 and 1, yielding K ~0.35-0.40 MHz and ~0.65-0.75 MHz for the two nuclei. These ranges are similar to the values of K calculated for Q_A^- for the nitrogens coupled to His-M219 and Ala-M260 and can similarly be attributed to an imidazole Nδ and peptide NH, respectively. Crystal structures with Q_B in the proximal position clearly show the histidine donor to be residue L190. (*5*)

Identification of the peptide donor to Q_B^- is not clear from the crystal structures alone - the peptide NH from either residue L224 or L225, or both, could contribute to the

hydrogen bond. Evidence from the HYSCORE spectra does not give any indication which of these residues is responsible for the H-bond to the O1 carbonyl. Nitrogen HYSCORE data appear to only contain contributions from one NH H-bond donor at the O1 carbonyl. However, in light of the proton HYSCORE described in Chapter 6, it is possible that there is one strong hydrogen bond resulting in HFI splitting and a second nitrogen coupling that is buried in the matrix region. In order to resolve experimentally which residue is involved would require specific isotopic (^{15}N) labeling of isoleucine or glycine, which is not possible at present.

In the spectra of Q_A^-, the near cancellation conditions allow for the calculation of the asymmetry parameter. When nitrogen nuclei are coupled to the semiquinone through a H-bond, the asymmetry parameter can provide some semi-quantitative information about the nature of this bond. The asymmetry parameter depends on the symmetry of the EFG at the quadrupole nucleus. While the gradient depends on all charged or polar species surrounding the nucleus, significant differences in asymmetry between nuclei coupled to the semiquinone are largely due to occupancy of valence orbitals.(*37, 38*) Experiments with different Cu(II)-coordinated imidazole complexes illustrate the correlation between the occupancy of sp^2 hybrid orbitals and η. (*35, 39*) In these imidazole systems, the EFG tensor is defined with the zz component normal to the imidazole plane, and the xx component pointing along the external sp^2 orbital. An increase in η toward 1 is correlated with an increase in occupancy of the external orbital. Density functional theory (DFT) studies of hydrogen bonds between imidazole derivatives and water and imidazole derivates and quinones show that an increase in linearity and/or shortening of the H-bond result in an increase in the asymmetry

parameter. (*39*) The experimental and DFT results indicate that η approaching 1 corresponds to structures with the highest occupancy of the external hybrid orbital, and implies nearly ideal geometry for the H-bond through which spin density is exchanged. (*35*)

The two coupled nitrogen nuclei present in HYSCORE spectra of Q_A^- show markedly different asymmetry, indicating a pronounced difference in electric field gradient at these nuclei. The His-M219 Nδ has a value of η = 1 whereas the M260 peptide NH is substantially smaller with η = 0.63. It is assumed, for the sake of this analysis, that the occupancies of the sp^2 orbitals involved in C-N bonds are symmetric and any change in EFG is primarily due to spin density transferred onto the external hybrid orbital.[5] For the His Nδ, the value of η = 1 is similar to model imidazole complexes that exhibited the greatest relative occupancy of the external sp^2 orbital, whereas the much lower value of η = 0.63 can be related to complexes where there is ~65% less (calculated from model complexes with known external sp^2 orbital occupancy and η~ 0 to η~ 1) spin density transferred to the external orbital. (*35*) This analysis is in line with the conclusion that the H-bond to His is much stronger than the H-bond to peptide, and has a much greater effect on the electronic structure. It is reasonable to expect this type of asymmetry in the Q_A site pointing in the direction of His and, in turn, in the direction of eventual electron transfer.

[5] The assumption that any transferred spin density transferred onto the nitrogen will redistribute symmetrically on the two C-N bonds is on the order that would be required to augment the EFG. There is probably some error introduced by this assumption, but the analysis is meant to be qualitative.

X-band HYSCORE data for the Q_B site do not allow calculation of the asymmetry parameter for either of the coupled nitrogens because the cancellation condition is not met. In order to make use of Eqn. 1, the spectra must be shifted into cancellation conditions, which require that $A/2 \sim \nu_N$. The HFI measured for the coupled nitrogen nuclei of Q_B^- are far too small to achieve this at X-band. However, the Larmor frequency is a function of magnetic field (Chapter 3, Eqn. 7), so experiments at lower frequency - S or L-band - could create cancellation conditions and make possible the calculation of the complete set of quadrupole parameters for nuclei coupled to Q_B^-.

Analysis of the HFI Tensors for Q_A and Q_B

The existence of non-zero isotropic hyperfine coupling values for the nitrogens coupled to the RC semiquinones indicates that unpaired spin density from the semiquinone is transferred onto these nitrogens and implies the existence of H-bonds acting as "atomic bridges". Isotropic hyperfine interactions for nitrogen nuclei arise from unpaired 2s spin density, while unpaired 2p spin density contributes to the anisotropic hyperfine interaction.(*37, 40, 41*) Spin transferred to the 2s orbital, which is responsible for the orientation independent isotropic hyperfine coupling, is exclusively transferred via direct spin delocalization. Using the calculated atomic unit spin value of a = 1811 MHz for a nitrogen nucleus,(*42*) the unpaired s spin density is estimated from the measured isotropic coupling constant relative to the unit spin value, i.e., $\rho_s = a/1811$. (Table 4.2)

Table 4.2. Isotropic HFI constants and related s spin density

	Nitrogen	*a*, MHz	s spin density
Q_A	His-M219 Nδ	2.4	1.33×10^{-3}
	Ala-M260 NH	1.8	0.99×10^{-3}
Q_B	His-L190 Nδ	1.5	0.83×10^{-3}
	L224/L225 NH	0.45	0.25×10^{-3}

Anisotropic HFI will contain a significant contribution from unpaired p spin density transferred from the carbonyl oxygen through the proton by spin polarization.(*37, 41*) Therefore, p populations can be calculated with the *anisotropic* constant for unit spin, T_p^o = 138.8 MHz for nitrogen nuclei. However the methodology needs to account for the symmetry of the anisotropic tensor. For anisotropy derived exclusively from p contributions, a correction must be applied for angular contributions that are not accounted for in the unit spin value for T_p^o. In the case of p orbitals the corrections (4/5, –2/5, -2/5) can be used.(*42*) For a significantly rhombic or axial tensor, the largest component of the anisotropic tensor (2*T*) can be used with the T_p^o value of 111 MHz (applying the 4/5 angular correction).(*40*) (Table 4.3)

Table 4.3. Anisotropic HFI tensors and the related p spin density

	Nitrogen	$2T$ (exptl.), MHz	p spin density
Q_A	His-M219 Nδ	0.74	6.4 x 10^{-3}
	Ala-M260 NH	0.48	4.3 x 10^{-3}
Q_B	His-L190 Nδ	~0.30-0.50	(2.7-4.5) x 10^{-3}
	L224/L225 NH	~0.21-0.28	(1.9-5.5) x 10^{-3}

The $2s^2 2p^3$ valence shell of the nitrogen atom consists of four orbitals. In sp^2 hybridization, as for imidazole and peptide N, the 2s orbital and two 2p orbitals result in three hybrid orbitals, two involved in C-N bonding and one external involved in N-H bonding. The fourth orbital ($2p_z$) is a lone pair. The sp^2 hybrid orbitals can be described by the wave function:

$$\psi = c_s |2s> + c_p |2p_x>$$
$$c_s^2 + c_p^2 = 1 \qquad (3)$$

For the external orbital, the population of the s orbital (c_s^2) is determined by $\cot^2\theta$, where θ is defined as half the CNC bond angle. For ideal sp^2 hybridization geometry with 2θ = 120°, the c_s^2 and c_p^2 population coefficients are 1/3 and 2/3, respectively. In imidazole, the angle is θ = 108-110°, giving $c_s^2 \sim$ ½. From Eqn. 3, a similar spin density, $c_p^2 = 1 - c_s^2$, should derive from the 2p orbital. Thus, sp^2 hybridization typically leads to p/s ratios of 1-2. However, the p/s ratios in Table 4.4, from the spin populations given in Tables 4.2 and 4.3, are all imply substantially larger than expected for an sp^2 hybrid orbital, suggesting additional factors contribute to the anisotropic hyperfine tensor. Additional p

spin density could be due to incomplete sp^2 hybridization, or contributions to the hyperfine tensor from additional nuclei.

After spin density is transferred onto the nitrogen from the semiquinone, it is expected that this would result in a reorganization of the electronic structure. An excess of p spin density could be explained by the resulting structure not regaining sp^2 hybridization. Excess p populations could reside on the unhybridized orbital or be redistributed onto adjacent nuclei to the H-bonded nitrogen. The exact mechanisms require more specific quantitative attention.

Table 4.4. Calculated p/s ratios

	Nitrogen	p/s ratio
Q_A	His-M219 Nδ	4.8
	Ala-M260 NH	5.1
Q_B	His-L190 Nδ	3.2-5.4
	L224/L225 NH	7.6-10

In addition to transferred spin density, anisotropic HFI commonly contains a component from magnetic dipole coupling, T_{dd}, given by equation 4.(*43*)

$$T_{dd} = \left(\frac{b}{r^3}\right)\rho_O\left(3\cos^2\phi - 1\right)$$
$$b = \frac{g_e g_I \beta_e \beta_I}{h} \qquad (4)$$

In powder type spectra, the orientational term ($3\cos^2\phi$ - 1) can be omitted; b is a combination of the nuclear and electronic g-factors and magnetons and is equal to 5.54 for ^{14}N nuclei. ρ_O is the spin density on the oxygen and has been estimated from ENDOR studies of RCs using isotopically labeled quinones (O1: 0.204 and O4: 0.148).(*6*) Distances measured from crystal structures can be used to determine the vector, r, connecting the heavy atoms, in order to calculate T_{dd}. (Table 4.5)

When the dipolar and spin density transfer axes are aligned, the anisotropic tensor should be the sum $T = T_{dd} + T_p$ (and the maximum component of the axial tensor is $2T = 2(T_{dd} + T_p)$). It is unclear what portion of the experimentally determined anisotropic tensor is due to contributions of transferred p spin density. The sp^2 orbitals should have similar s and p character, $c_s^2 \sim c_p^2$, therefore s spin populations from Table 4.2 can be used to estimate the T_p contribution to the anisotropic hyperfine tensor (e.g., $T_p = 55 * 1.33\text{x}10^{-3} = 0.073$ MHz for Q_A His-M219)[6]

Table 4.5. Estimated values for the components of the anisotropic constant

	Nitrogen	N … O Å*	T_{dd} MHz	T_p MHz	$2(T_{dd} + T_p)$ MHz	$2T$ (exptl) MHz
Q_A	M219	2.69	0.042	0.073	0.23	0.74
	M260	2.79	0.052	0.054	0.21	0.48
Q_B	L190	2.80	0.043	0.046	0.18	0.3-0.5
	L224	3.09 Å	0.035	0.014	0.10	0.21-0.28
	L225	2.91 Å	0.042	0.014	0.11	0.21-0.28

* Distances from Wraight and Gunner 2008, with errors omitted (*3*)

[6] The angular correction, 2/5, is applied to the value of T_p^o. In this case we are interested in the anisotropic component of the tensor, T - where $2T$ is the maximum component.

In the absence of any knowledge about the relative orientation of these components, $2(T_{dd} + T_p)$ can be taken as a theoretical ceiling for the maximum component of an axial or rhombic tensor. However, in all cases, the experimental anisotropic hyperfine constants are seen to substantially exceed this value (Table 4.5). Increasing the dipolar component to compensate for these differences would require an unrealistically large decrease in H-bond lengths, particularly given that the distance would need to decrease on both the O1 and O4 sides of the quinones. This strongly suggests that there are additional contributions to the anisotropic HFI tensor not considered by this model. The most likely conclusion is that there is a larger density of unpaired p spin on the coupled N than has previously been predicted. A likely cause could be the redistribution of the electronic structure of H-bonding partners, partially invalidating these calculations. In Table 4.5 all experimental values greatly exceeded the potential ceiling, but the largest discrepancy was at the H-bond to His-M219, indicating a particularly large perturbation from "idealized" electronic structures.

It is likely that the reason for the high p/s ratios is a combination of multiple factors. Futher quantitative work is required to answer these questions about the electronic structure of the quinone binding sites.

References

1. Feher, G., Allen, J. P., Okamura, M. Y., and Rees, D. C. (1989) Structure and function of bacterial photosynthetic reaction centres, *Nature 339*, 111-116.
2. Abresch, E. C., Paddock, M. L., Stowell, M. H. B., McPhillips, T. M., Axelrod, H. L., Soltis, S. M., Rees, D. C., Okamura, M. Y., and Feher, G. (1998) Identification of proton transfer pathways in the X-ray crystal structure of the bacterial reaction center from *Rhodobacter sphaeroides*, *Photosynth. Res. 55*, 119-125.
3. Wraight, C. A., and Gunner, M. R. (2009) The Acceptor Quinones of Purple Photosynthetic Bacteria- Structure and Spectroscopy, In *Advances in Photosynthesis and Respiration: The Purple Photosynthetic Bacteria* (Hunter, C. N., Daldal, F., Thurnauer, M., and Beatty, J. T., Eds.), pp 379-405, Springer, Dordrecht, The Netherlands.
4. Sinnecker, S., Flores, M., and Lubitz, W. (2006) Protein-cofactor interactions in bacterial reaction centers from *Rhodobacter sphaeroides* R-26: effect of hydrogen bonding on the electronic and geometric structure of the primary quinone. A density functional theory study., *Phys. Chem. Chem. Phys. 8*, 5659-5670.
5. Stowell, M. H. B., McPhillips, T. M., Rees, D. C., Soltis, S. M., Abresch, E., and Feher, G. (1997) Light-induced structural changes in photosynthetic reaction center: implication for mechanism of electron-proton transfer, *Science 276*, 812-816.
6. Lubitz, W., and Feher, G. (1999) The primary and secondary acceptors in bacterial photosynthesis III. Characterization of the quinone radicals Q_A^- and Q_B^- by EPR and ENDOR, *Appl. Magn. Reson. 17*, 1-48.
7. Bosch, M., Gast, P., Hoff, A., Spoyalov, A., and Tsvetkov, Y. (1995) The primary acceptor quinone QA in reaction center of Rhodobacter sphaeroides R26 is hydrogen bonded to the Nδ-H of His M2219. An electron spin echo study of QA-, *Chemical Physics Letters 239*, 306-312.
8. Iwaki, M., Andrianambinintosoa, S., Rich, P. R., and Breton, J. (2002) Attenuated total reflection Fourier transform infrared spectroscopy of redox transitions in photosynthetic reaction centers: comparison of perfusion- and light-induced difference spectra, *Spectrochimica Acta Part A 58*, 1523-1533.
9. Breton, J., Boullais, C., Burie, J.-R., Nabedryk, E., and Mioskowski, C. (1994) Binding Sites of Quinones in Photosynthetic Bacterial Reaction Centers Investigated by Light-Induced FTIR Difference Spectroscopy: Assignment of the Interactions of Each Carbonyl of QA in Rhodobacter sphaeroides Using Site-Specific 13C-Labeled Ubiquinone, *Biochemistry 33*, 14378-14386.
10. Schweiger, A., and Jeschke, G. (2001) *Principles of pulse electron paramagnetic resonance*, Oxford University Press, Oxford, UK.
11. Spoyalov, A. P., Hulsebosch, R. J., Shochat, S., Gast, P., and Hoff, A. J. (1996) Evidence that Ala M260 is hydrogen-bonded to the reduced primary acceptor quinone QA-. in reaction centers of Rb. sphaeroides, *Chemical Physics Letters 263*, 715-720.

12. Poluektov, O. G., Utschig, L. M., Dubinskij, A. A., and Thurnauer, M. C. (2005) Electron transfer pathways and protein response to charge separation in photosynthetic reaction centers: time-resolved high-field ENDOR of the spin-correlated radical pair $P865^{+}Q_A^{-}$, *J. Am. Chem. Soc. 127*, 4049-4059.
13. Goldsmith, J. O., and Boxer, S. G. (1996) Rapid isolation of bacterial photosynthetic reaction centers with an engineered poly-histidine tag, *Biochim. Biophys. Acta 1276*, 171-175.
14. Dutton, P. L., Leigh Jr, J. S., and Reed, D. W. (1973) Primary events in the photosynthetic reaction centre from *Rhodopseudomonas spheroides* strain R26: Triplet and oxidized states of bacteriochlorophyll and the identification of the primary electron acceptor, *Biochim. Biophys. Acta 292*, 654-664.
15. Isaacson, R. A., Lendzian, F., Abresch, E. C., Lubitz, W., and Feher, G. (1995) Electronic structure of Q_A^{-} in reaction centers from *Rhodobacter sphaeroides*. I. Electron paramagnetic resonance in single crystals, *Biophys. J. 69*, 311-322.
16. Utschig, L. M., Greenfield, S. R., Tang, J., Laible, P. D., and Thurnauer, M. C. (1997) Influence of iron-removal procedures on sequential electron transfer in photosynthetic bacterial reaction centers studied by transient EPR spectroscopy, *Biochemistry 36*, 8548-8558.
17. Utschig, L. M., Poluektov, O., Tiede, D. M., and Thurnauer, M. C. (2000) EPR investigation of Cu^{2+}-substituted photosynthetic bacterial reaction centers: evidence for histidine ligation at the surface metal site, *Biochemistry 39*, 2961-2969.
18. Feher, G., Okamura, M. Y., and McElroy, J. D. (1972) Identification of an electron acceptor in reaction centers of *Rhodopseudomonas spheroides* by EPR spectroscopy, *Biochim. Biophys. Acta 267*, 222-226.
19. Loach, P. A., and Hall, R. L. (1972) The Question of the Primary Electron Acceptor in Bacterial Photosynthesis, *PNAS 69*.
20. Feher, G., and Okamura, M. (1999) The primary and secondary acceptors in bacterial photosynthesis: II. The structure of the Fe^{2+}-Q^{-} complex, *Appl. Magn. Res. 16*, 63-100.
21. Dikanov, S. A., Tsvetkov, Y. D., Bowman, M. K., and Astashkin, A. V. (1982) Parameters of quadrupole coupling of ^{14}N nuclei in chlorophyll a cations determined by the electron spin echo method, *Chem. Phys. Lett. 90*, 149-153.
22. Dikanov, S. A., and Tsvetkov, Y. D. (1992) *Electron spin echo envelope modulation (ESEEM) spectroscopy* CRC Press, Boca Raton.
23. Stoll, S., Calle, C., Mitrikas, G., and Schweiger, A. (2005) Peak suppression in ESEEM spectra of multinuclear spin systems, *J. Magn. Res. 177*, 93-101.
24. Stoll, S., and Schweiger, A. (2006) EasySpin, a comprehensive software package for spectral simulation and analysis in EPR, *J. Magn. Res. 178*, 42-55.
25. Koepke, J., Eva-Maria Krammer, E.-M., Klingen, A. R., Sebban, P., Ullmann, G. M., and Fritzsch, G. (2007) pH Modulates the Quinone Position in the Photosynthetic Reaction Center from Rhodobacter sphaeroides in the Neutral and Charge Separated States. , *J. Mol. Biol. 371*, 13.

26. Paddock, M. L., Flores, M., Isaacson, R., Chang, C., Abresch, E. C., and Okamura, M. Y. (2007) ENDOR spectroscopy reveals light induced movement of the H-bond from Ser-L223 upon forming the semiquinone (Q_B^-) in reaction centers from *Rhodobacter sphaeroides*, *Biochemistry 46*, 8234-8243.
27. Paddock, M. L., Flores, M., Isaacson, R., Chang, C., Abresch, E. C., Selvaduray, P., and Okamura, M. Y. (2006) Trapped conformational states of semiquinone ($D^+Q_B^-$) formed by B-branch electron transfer at low temperature in *Rhodobacter sphaeroides* reaction centers., *Biochemistry 45*, 14032-14042.
28. Paddock, M. L., Isaacson, R. A., Abresch, E. C., and Okamura, M. Y. (2007) Light induced EPR spectra of reaction centers from Rhodobacter sphaeroides at 80K: Evidence for reduction of Q(B) by B-branch electron transfer in native reaction centers., *Appl. Magn. Reson. 31*, 29-43.
29. Xu, Q., Axelrod, H. L., Abresch, E. C., Paddock, M. L., Okamura, M. Y., and Feher, G. (2004) X-Ray structure determination of three mutants of the bacterial photosynthetic reaction centers from *Rb. sphaeroides*; altered proton transfer pathways., *Structure 12*, 703-715.
30. Lendzian, F., Rautter, J., Kass, H., Gardiner, A., and Lubitz, W. (1996) ENDOR and pulsed EPR studies of photosynthetic reaction centers: Protein-cofactor interactions, *Ber. Bunsen-Ges. Phys. Chem. 100*, 2036-2040.
31. Wraight, C. A. (1978) Iron--quinone interactions in the electron acceptor region of bacterial photosynthetic reaction centers, *FEBS Letters 93*, 283-288.
32. Okamura, M., Debus, R. J., Kleinfeld, D., and Feher, G. (1982) Chapter V, In *Function of Quinones in Endergy Conserving Systems* (Tumpower, B. L., Ed.), pp 299-317, Academic Press, New York.
33. Dikanov, S. A., Holland, J. T., Endeward, B., Kolling, D. R. J., Samoilova, R. I., Prisner, T. F., and Crofts, A. R. (2007) Hydrogen bonds between nitrogen donors and the semiquinone in the Q_i-site of the bc_1 complex, *J. Biol. Chem. 282*.
34. Yap, L. L., Samoilova, R. I., Gennis, R. B., and Dikanov, S. A. (2007) Characterization of mutants that change the hydrogen bonding of the semiquinone radical at the Q_H site of the cytochrome bo_3 from *Escherichia coli*, *Journal of Biological Chemistry 282*, 8777-8785.
35. Jiang, F., McCracken, J., and Peisach, J. (1990) Nuclear Quadrupole Interaction in Copper(II)- Diethylenetriamin-Substituted Imidazole Complexes and in Copper (II) Proteins, *J. Am. Chem. Soc. 112*, 9035-9044.
36. Palmer, M. (1984) 14N Nuclear Quadruple Coupling in Glycyl-Glycine and Related Peptides, *Z. Naturforsch. 39a*, 1108-1111.
37. Deligiannakis, Y., Boussac, A., and Rutherford, A. W. (1995) ESEEM study of the plastoquinone anion radical (QA.bul.-) in 14N- and 15N-labeled photosystem II treated with cyanide, *Biochemistry 34*, 16030-16038.
38. Townes, C., and Dailey, B. (1949) Determination of Electronic Structure of Molecules from Nuclear Quadrupole Effects, *Journal of Chemical Physics 17*, 782-796.
39. Fritscher, J. (2004) Influence of hydrogen bond geometry on quadrupole coupling parameters: A theoretical study of imidazole–water and imidazole–semiquinone complexes, *Phys. Chem. Chem. Phys. 6*, 4950-4956.

40. Martin, E., Samoilova, R. I., Narasimhulu, K. V., Wraight, C. A., and Dikanov, S. A. (2010) Hydrogen Bonds between Nitrogen Donors and the Semiquinone in the Q_B Site of Bacterial Reaction Centers, *J. Am. Chem. Soc. 132*, 11671-11677.
41. Deligiannakis, Y., Hanley, J., and Rutherford, A. W. (1999) 1D- and 2D-ESEEM Study of the Semiquinone Radical QA- of Photosystem II, *J. Am. Chem. Soc. 121*, 7653-7664.
42. Morton, J. R., and Preston, K. F. (1978) Atomic Parameters for Paramagnetic Resonance Data, *J. Magn. Res. 30*, 577-582.
43. Wertz, J. E., and Bolton, J. R. (1972) *Electron Spin Resonance: Elementary Theory and Practical Applications*, McGraw-Hill Inc, United States of America.

Figures

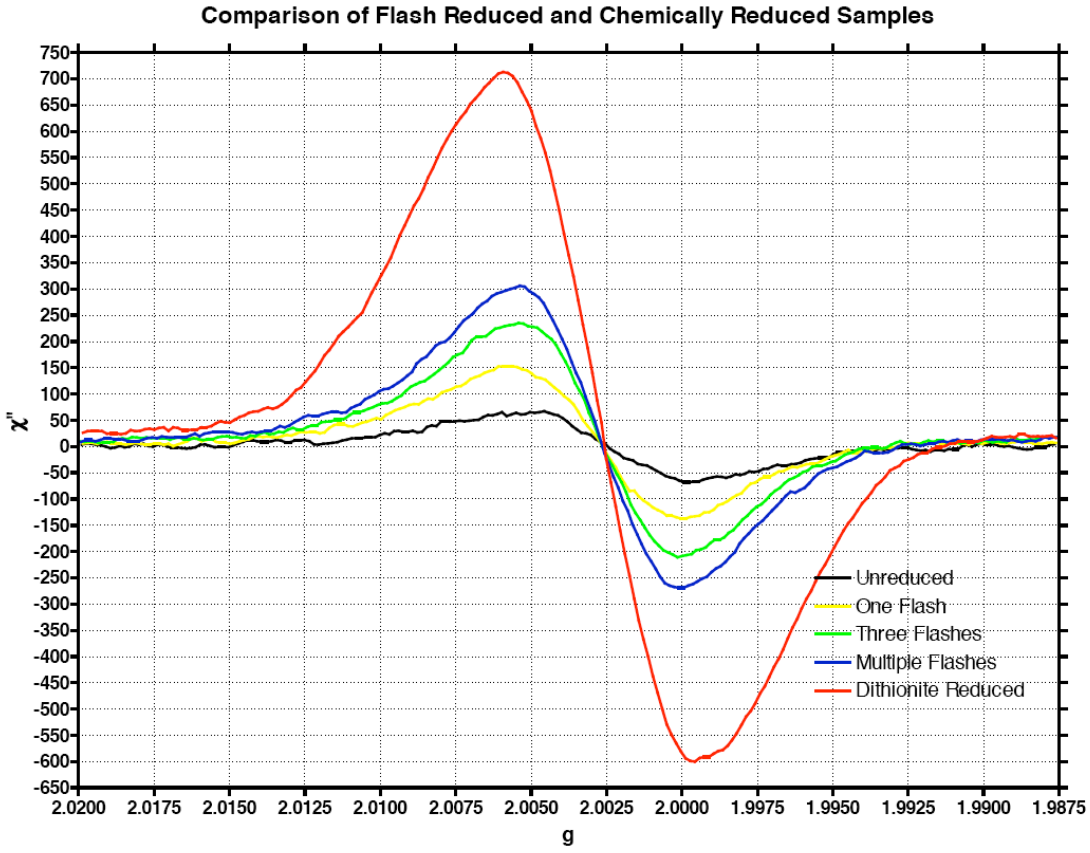

Figure 4.1. X-band EPR obtained at 10 K with 1 G modulation and 0.1 mW microwave power. The yield of chemically generated Q_A^- is far greater than attempts at phototrapping with laser flashes.

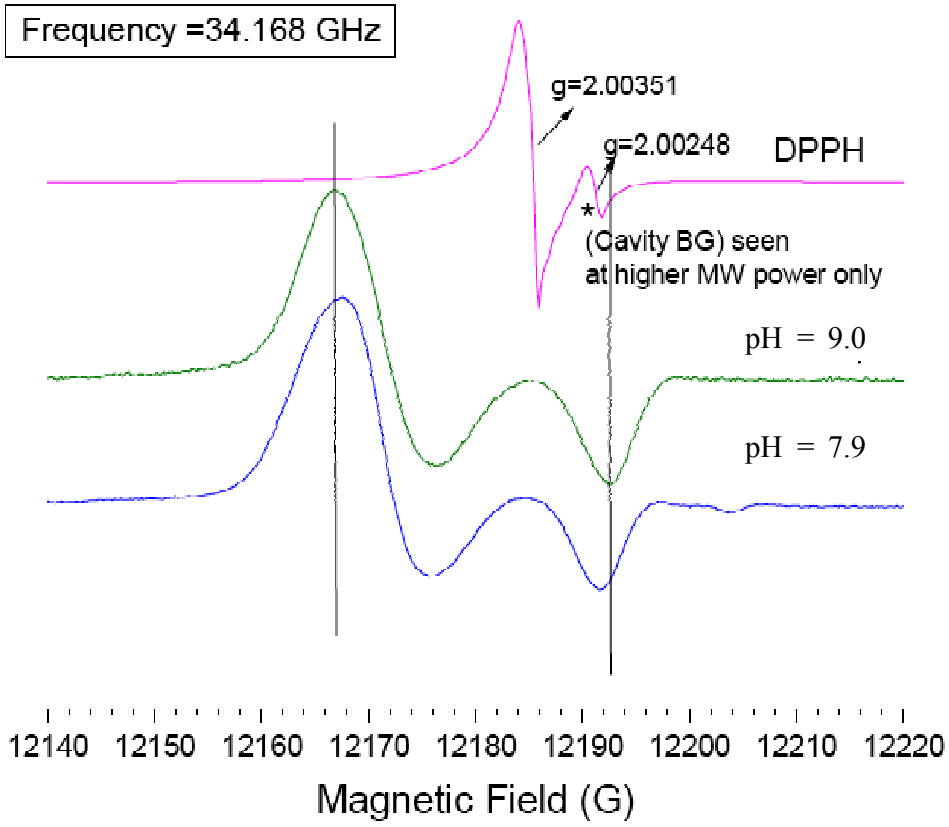

Figure 4.2. The Q-band EPR spectrum of a typical Q_A^- sample prepared by dithionite reduction at pH 9.0 and pH 7.9. This type of spectrum is used to calculate the components of g-tensor presented in Table 1. The spectrum was taken at ~65 K with 125 μW microwave power and 1.5 G modulation amplitude.

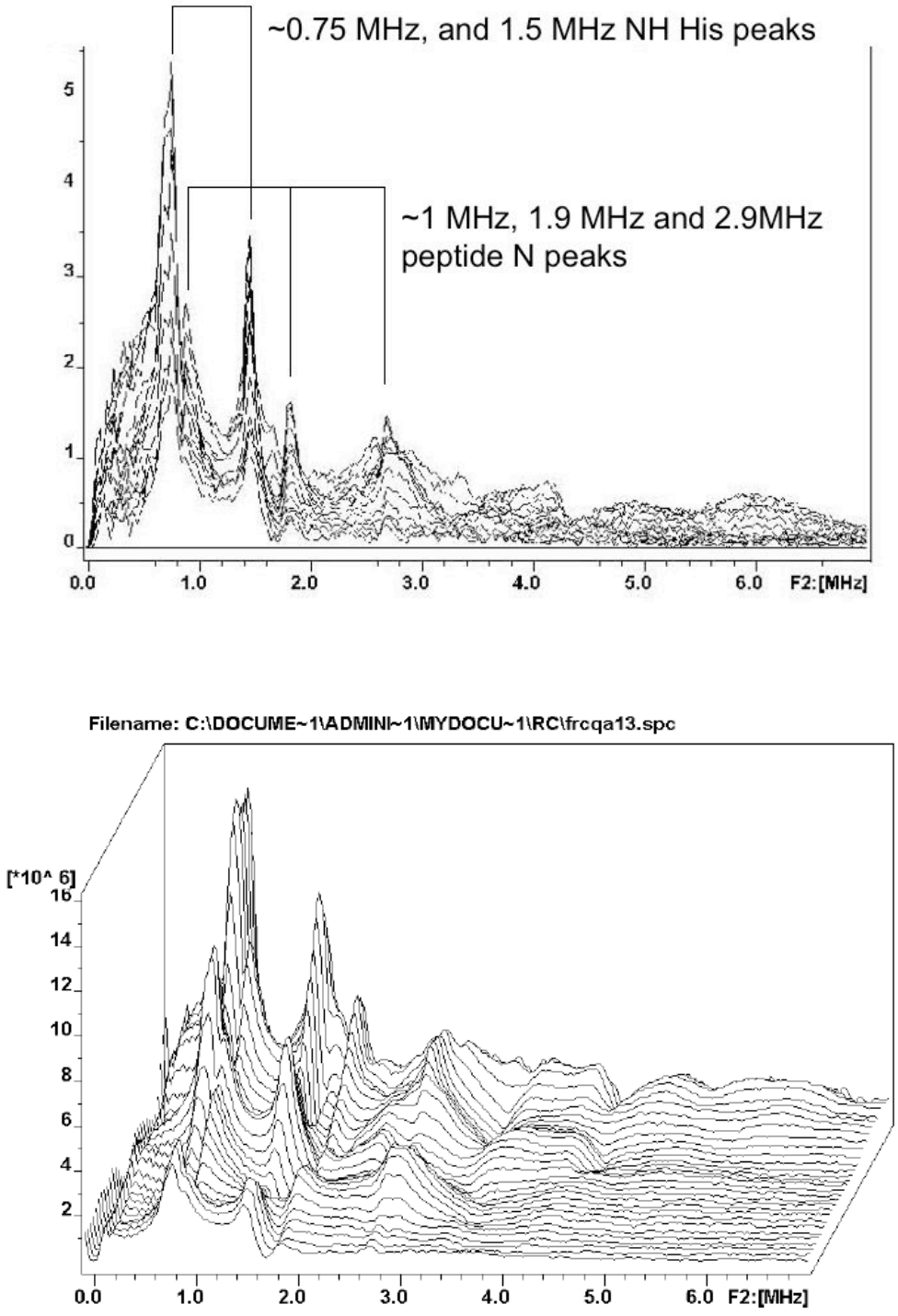

Figure 4.3. The X-band 3-pulse ESEEM spectrum of Q_A^-, represented as a stacked plot with the initial value of τ=100 ns followed by 16 ns steps. In the flattened view (Top) the peaks assigned to His-M219 and Ala-M260 are labeled.

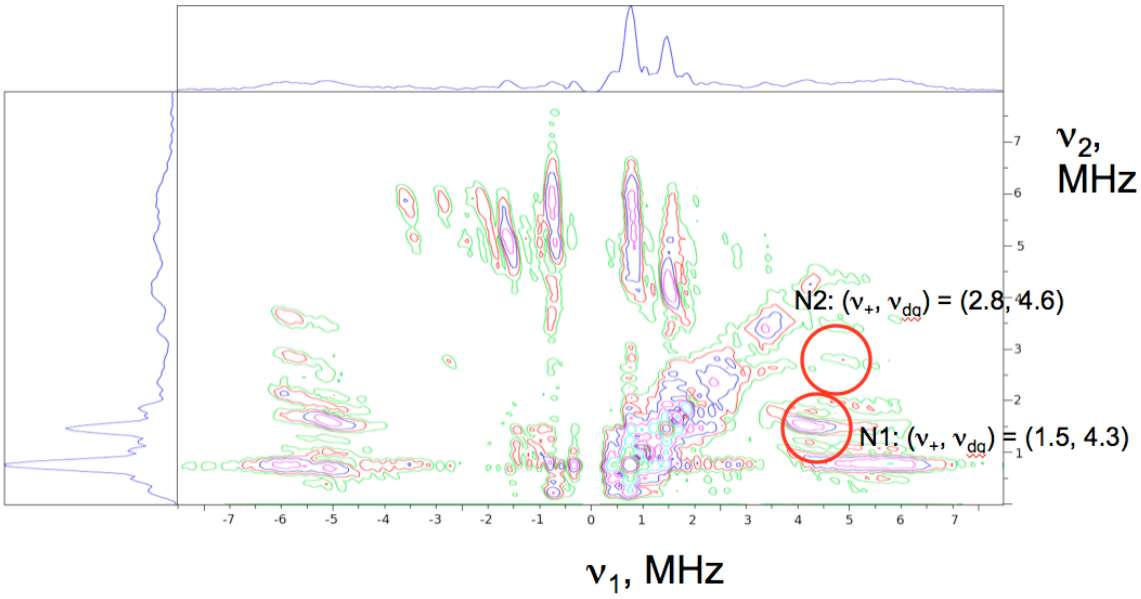

Figure 4.4. 2D ^{14}N-HYSCORE spectrum of Q_A^- in the contour presentation. Significant features are labeled indicated where double quantum transitions were resolved in this spectrum. τ =136 ns.

A

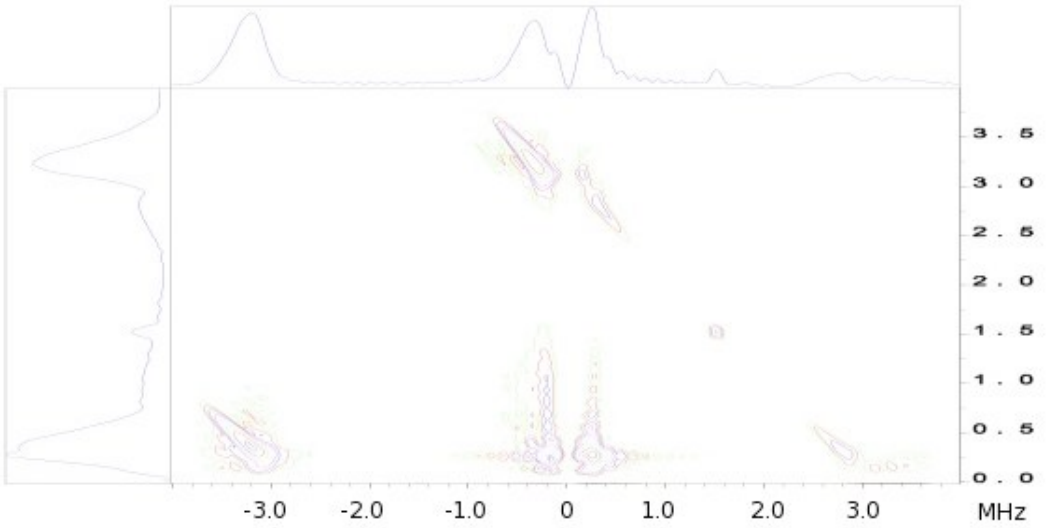

B

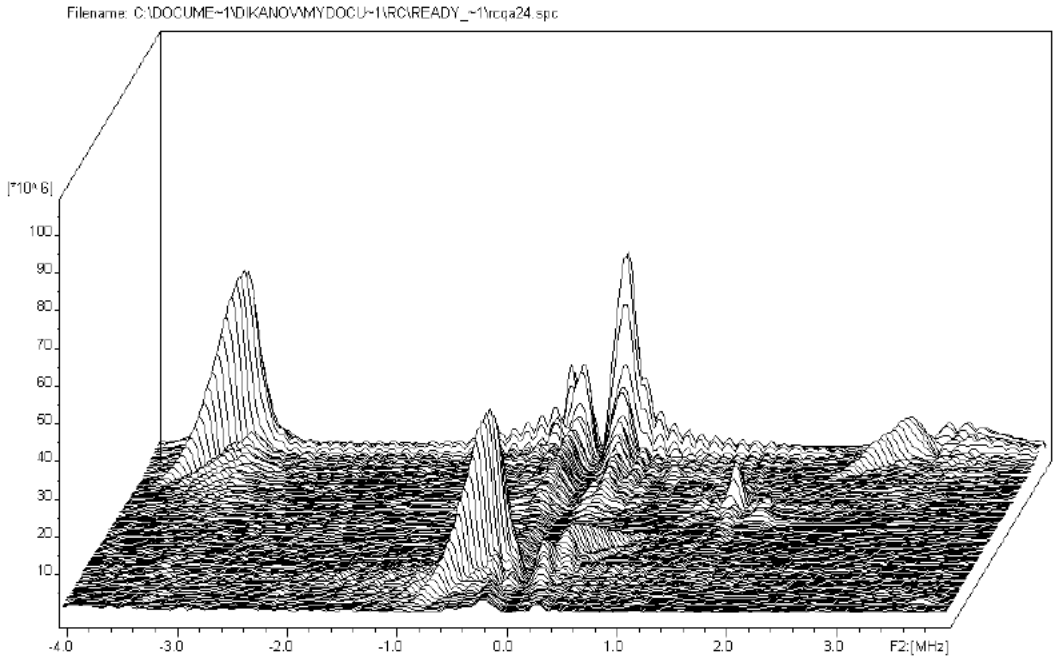

Figure 4.5. 2D HYSCORE spectrum of Q_A^- in ^{15}N labeled reaction centers shown as contours (A) and in stacked (B) presentations. Peaks in the (-,+) quadrant are attributable to His, while (+,+) peaks are primarily peptide. τ =136 ns.

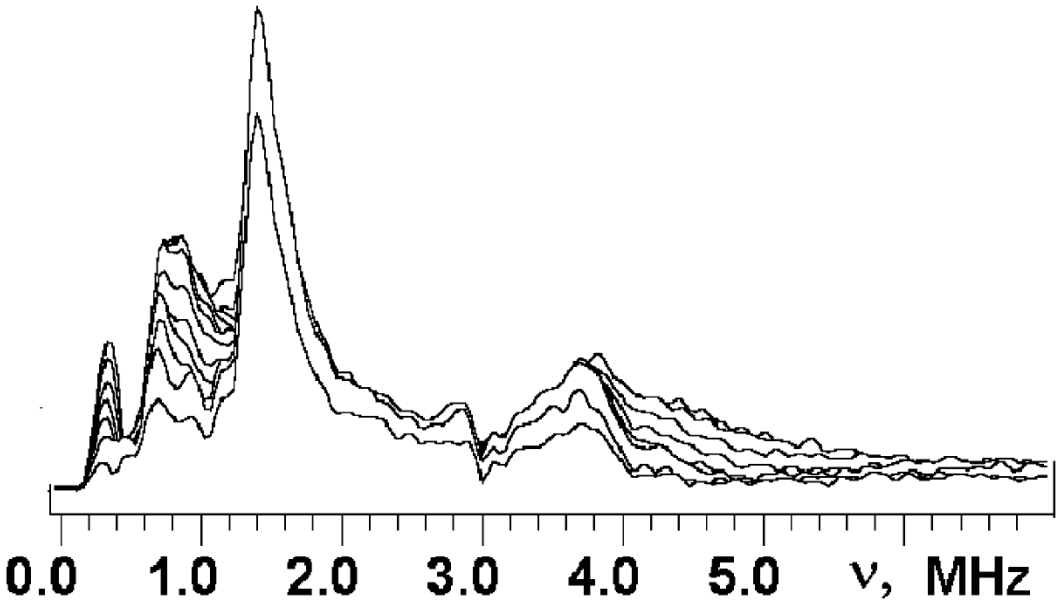

Figure 4.6. The X-band 3-pulse ESEEM spectrum of Q_B^-, represented as a stacked plot with the initial value of τ=100 ns followed by 16 ns steps.

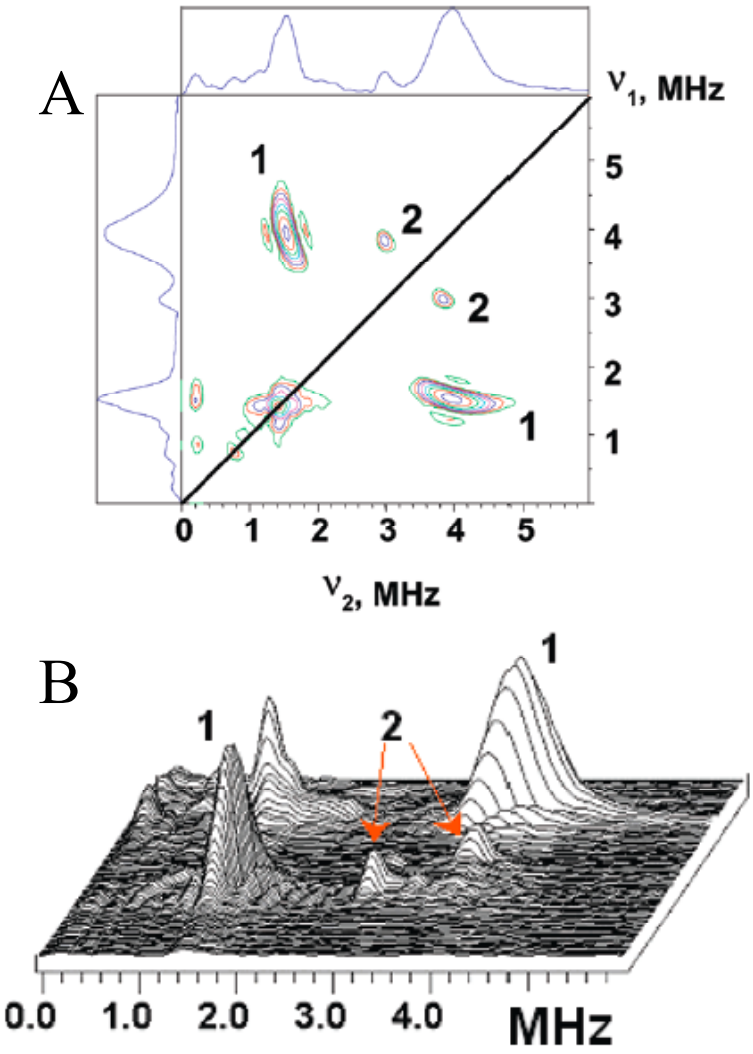

Figure 4.7. 2D ^{14}N-HYSCORE spectrum of Q_B^- shown as contours (A) and stacked (B) presentations. Peaks from two nitrogen nuclei are labeled. τ =136 ns.

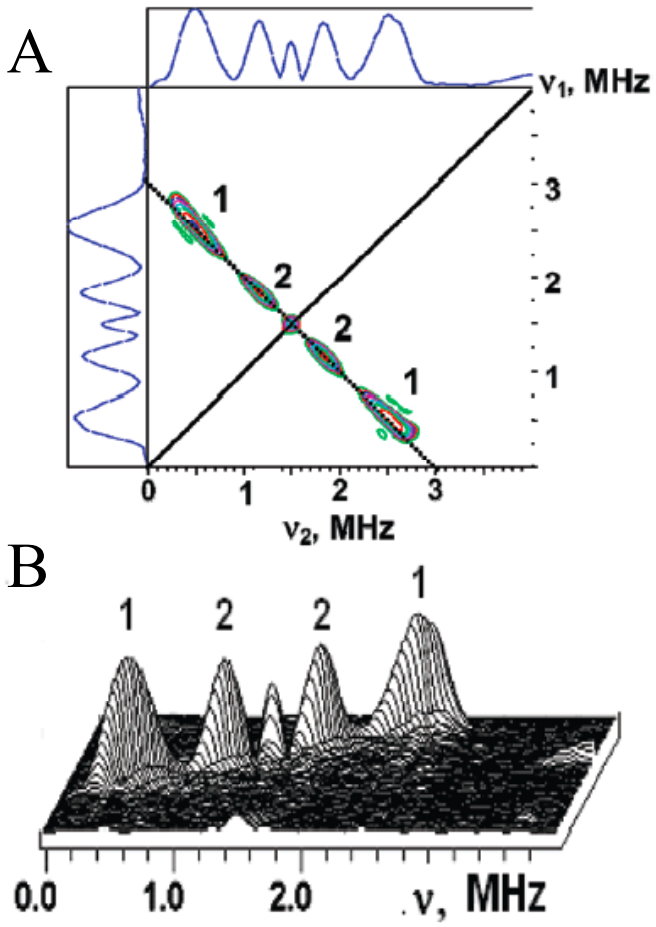

Figure 4.8. 2D HYSCORE spectrum of Q_B^- in ^{15}N labeled reaction centers presented in contour (A) and stacked (B) form. Peaks from two nitrogen nuclei are labeled. τ =136 ns.

Chapter 5:

Mutation of the Residue M265 Isoleucine to Threonine Examined by Pulsed EPR

Abstract

Mutation of residue M265 in the Q_A binding site from isoleucine to the small polar amino acids threonine and serine decreases the redox midpoint potential of Q_A by 80-100mV relative to wild type while mutation to the small non-polar amino acid valine has no energetic effect. 3-pulse ESEEM and HYSCORE are used to measure the nitrogen coupling to Q_A^- in the Ile-M265 to Thr (M265IT) mutant, and the results are compared to wildtype. In order to examine the potential structural effects, molecular dynamics simulations were performed on this mutant using the program NAMD. All the results suggest that although there is only a small effect on binding site structure, these are potentially significant effects on the electronic structure. Furthermore, preliminary electrostatic calculations yield changes in M265IT RCs of sufficient magnitude to suggest that the electric potential and/or field gradient are important contributions to the mutant phenotype.

Introduction

In *Rhodobacter sphaeroides*, Q_A and Q_B are identical ubiquinone-10 molecules. Despite this, Q_A and Q_B exhibit very distinct properties and the forward direction of electron transfer is always through Q_A to Q_B. Q_A functions exclusively to shuttle electrons one at a time to Q_B where two electrons (and protons) are accumulated. In order to perform these distinct functions, specific electrochemical properties must be conferred onto the accepter quinones by their protein environments. (*1-4*) High resolution crystal structures show the two quinones are bound to the reaction center (RC) in similar helix-loop-helix motifs (Q_A in the M subunit and Q_B in the L subunit) and contain several analogous hydrogen bonds. (*5-7*) Both quinones contain a H-bond between their O4 carbonyl and one of the Fe(II) liganded histidines, and a second H-bond between the O1 carbonyl and protein backbone. Given these striking similarities between the two binding pockets, it is important to understand how more subtle interactions could affect the function of the individual quinones.

Site directed mutagenesis was used to modify the properties of the quinones – directly indicating the importance of the binding pocket structure on quinone function. There are several good candidates for mutation in the RC that could effect changes in Q_A electrochemistry, including the bulky residues isoleucine at M265 and tryptophan at M252, which fill the space on opposite sides of the quinone head group. Site directed mutation of Trp-M252 to tyrosine or phenylalanine causes a modest change (≈ -30 mV) in the redox potential of Q_A. (*8, 9*) However, the potential usefulness of these mutations

to study structure-function effects in the binding pocket are tempered by low quinone affinity in the Trp-M252 to leucine RC, which showed the largest change in function. (*8, 9*)

While Trp-M252 has been suggested to participate in π stacking with the Q_A headgoup, Ile-M265 appears to be simply in van der Waals contact with the Q_A headgroup. Nevertheless, site directed mutation of M265 to the small polar amino acids, serine and threonine, showed a surprisingly large, 80-100 mV, drop in the redox potential of Q_A. (*10, 11*) Mutation of M265 to the small, non-polar amino acid, valine, however, showed no significant departure from the wild type, ruling out decreased van der Waals contact as a cause of the redox potential drop. Removing the bulky isoleucine could reduce steric restriction on quinone methoxy group orientations – which have been implicated in redox tuning. (*12, 13*) However, the methoxy groups were ruled out as the cause of the functional effects in this mutation. The redox shift in the polar mutants was similar when the native ubiquinone was replaced with 9,10-anthraquinone, which lacks methoxy groups. (*10*)

The lack of any significant change in midpoint potential in the valine mutant versus the wild type points to the hydroxyl group on the sidechain of threonine or serine as the source of these changes, and not simply steric or van der Waals interactions. Introducing a hydrogen bond donor into the quinone binding pocket could either have a direct effect on the quinone head group, or introduce perturbations in the backbone structure. (*10*) Investigation of the rotomers of Thr-M265 indicated that it is unlikely any hydrogen bonds form directly between the hydroxyl and the quinone but, instead, suggested the possibility of a H-bond between the threonine hydroxyl and backbone

carbonyl at M261.(*11*) Energy minimizations (using GROMOS96) showed a possible interaction between M265 hydroxyl and the M261 backbone carbonyl. This was accompanied by a perturbation of the backbone, which increased the H-bond distance between M260 and the semiquinone O1 carbonyl by up to 0.1 Å.(*11*)

If the change in H-bond length between M260 and the O1 carbonyl predicted by energy minimizations exists in these mutants, it is expected that there would be shifts in the carbonyl stretch frequency. This has been studied by Fourier transform infrared (FTIR) spectroscopy to measure the difference in IR absorption between RCs in the Q_A and Q_A^- states. (*14-16*) In fact, FTIR spectra of the M265 mutants did not provide conclusive evidence to support or disprove this hypothesis. An FTIR band at 1660 cm^{-1} has been shown by isotopic labeling to be due to the O1 carbonyl (*14*), and a change in H-bond distance between M260 and O1 could be expected to result in a shift in the frequency of this band. However, the O1 carbonyl stretch frequency, which is similar to that in apolar solvent, is buried in the amide I band and was not resolved.(*11*) Any effects on this stretch frequency due to the mutation aren't visible but, from the wild type spectra (*14*), it can be concluded that any H-bond to the O1 carbonyl is weak. These same FTIR measurements did show a small shift of another band from 1601 to 1603 cm^{-1} – a band known to be associated with the O4 carbonyl. (*11, 14*) The position of this band is certainly affected by the H-bond to His-M219 and the upshift in the polar mutations likely implies a change at His-M219, the O4 carbonyl or both. Any implications of this were not considered in depth in the original description.

In the IR spectral region characteristic of the anionic semiquinone (1430-1490 cm^{-1}), all M265 mutants showed distinctive frequency shifts versus the wild type. (*11*)

This "anion band" comprises contributions from the O1 and O4 semiquinone carbonyl stretch modes, but the assignments are uncertain. (*14, 17*)

All in all, the FTIR data are of limited use in identifying an origin of the substantial shift in the mid-point potential of Q_A seen in the M265 polar mutants. The IR band associated with the H-bond at the O1 carbonyl was, unfortunately, not observed and no specific changes were seen in the amide I and amide II regions of the spectrum, attributable to the backbone. A small shift was observed in the 1601 cm^{-1} band attributed to the H-bond at the O4 carbonyl (*11*), but this does not preclude changes in the O1 H-bond.

Preliminary crystallographic studies of the M265IT mutant RC reveal a threonine configuration that is similar (but not identical) to that proposed, but show little backbone movement (A. Mattis, personal communication). However, the backbone movement is expected to be small and it is doubtful that X-ray crystallography has the resolution to address this, or the H-bond length.

On the other hand, EPR and DFT studies on wild type RCs indicate that the H-bond to Ala-M260 is much weaker than the H-bond to His-M219 and the electron density of the Q_A semiquinone is asymmetric and biased toward the O4 carbonyl.(*18-21*) An increase in the length of the H-bond to the O1 carbonyl would further decrease the spin density transferred onto the M260 backbone NH and would add to the already existing asymmetry between H-bond strengths. In light of the fact that the H-bonding at the O1 carbonyl is already presumed to be weak, and electron transfer is in the direction of O4, it seems unlikely that this type of shift could be responsible for the significant shift in redox potential in the polar mutants.

The structural effects of the M265I—›T mutation are evidently quite minor. In the previous model, the possible significance of the sidechain dipole, i.e., electrostatics, was not considered likely but, clearly, the serine or threonine hydroxyl will alter the electric potential in or near the Q_A site, which could directly affect the redox potential. It could also cause a redistribution of electron density in the His-M219 π-electron structure and O4 of the semiquinone carbonyl, which is along the path of electron transfer from Q_A to Q_B. While a change in the electron density of O4 would affect the Q_A electron affinity and therefore specific redox properties, additional electronic redistribution in the space between RC quinones could change the stabilization of the Q_A^- state.

The failure of X-ray crystallography to provide insight to the structural changes that underlie the substantial drop in Q_A redox potential in the M265 polar mutants is essentially a matter of resolution, while the the FTIR data lack a firm basis for interpretation, especially of the semiquinone "anion band". In contrast, pulsed EPR can provide information about the hyperfine interactions (HFI) and nuclear quadrupole interactions (NQI), which are very sensitive to the electronic structure of the quinone and its binding pocket, and can be interpreted with the help of structure-based quantum mechanical calculations. HFI is a direct reflection of spin density transferred between the semiquinone and coupled nuclei. NQI parameters are related to the strength and symmetry of the electric field gradient (EFG) at the coupled nuclei. These two parameters are sensitive to minor changes in electronic structure not accessible in previously used techniques, and can potentially reveal any electronic redistribution due to the introduction of a polar sidechain at M265.

Q_A^- Sample Generation in M265IT mutants

The polar mutations at M265 (serine and threonine) showed similar decreases in midpoint potential and it is assumed that the mechanism involved in this electrochemical shift is similar in both mutants. The threonine mutant (M265IT) has a slightly larger shift in midpoint potential versus wildtype and might be expected to have a larger effect on EPR spectra. With this in mind, the M265IT mutant was chosen for initial pulsed EPR investigations. M265IT cells were grown by the semi-aerobic method described in detail in Chapter 2. Chemical procedures to replace the native Fe^{2+} with Zn^{2+}, described in Chapter 2, could be applied without modification to these types of RCs..

For EPR sample preparation, RCs were exchanged with buffer containing Triton X-100 as the detergent, by approximate 50 fold dilution and reconcentration to 200-300 μM in Amicon Ultra-15 centrifugal concentrators at 4 ^oC. When the sample requires deuterium exchange, the buffer used for the dilution was made with D_2O and allowed to incubate at 4 ^oC for 12-24 hours (overnight) prior to reconcentration. The RCs were combined with 10% glycerol and the semiquinone was generated chemically by adding 8 mM Na-dithionite from freshly prepared 128 mM stock (in 1 M Tris, pH 8). All solutions were bubbled with nitrogen or argon prior to reduction. The samples were put into Wilmad precision EPR tubes and frozen in liquid nitrogen. Pulsed EPR measurements were carried out using the Bruker ELEXSYS E580 spectrometer fitted with an X-band cavity and an Oxford CF 935 cryostat. Temperatures were routinely set at 70 K.

1D 3-pulse ESEEM of the M265IT Q_A Semiquinone

The 3-pulse ESEEM spectrum of Q_A^- in the wildtype RC was described in detail in Chapter 4.(Chapter 4, Figure 4.3) These spectra show features that were ascribed to NQI transitions from two ^{14}N nuclei and a higher frequency, poorly defined peak from double quantum transitions. Two peaks at 0.75 and 1.5 MHz were assigned to the His-M219 Nδ and a weaker triplet at ~1 MHz, 1.9 MHz, and 2.9 MHz was visible in stacked plots and was assigned to Ala-M260 NH.

The 3-pulse ESEEM spectrum for M265IT mutant RCs is dramatically different from the wildtype and is shown in Figure 5.1. The spectrum had well resolved peaks at 0.63, 0.85 and 1.48 MHz that conformed well to the type of triplet expected of NQI transitions under the cancellation condition, but not with the clear axial symmetry seen in the wild type. The spectrum also contains poorly resolved features at higher frequency (around 3 MHz). However, one clear triplet can be assigned in this spectrum – as opposed to two in wildtype. The higher frequency features were too small to assign with any certainty to NQI features on or off cancellation (described in depth in Chapter 3) but do suggest the presence of a second coupled nitrogen. Using Equation 1, the NQI parameters, K and η, were calculated for the one, well resolved triplet:

$$\nu_+ = K(3+\eta); \quad \nu_- = K(3-\eta); \quad \nu_o = 2K\eta \qquad (1)$$

The results are compared to the wild type in Table 5.1.

Table 5.1. NQI parameters

Nitrogen	*K* (MHz)	η
WT: His-M219 Nδ	0.375	~1
WT: Ala-M260 NH	0.766	0.63
M265IT Triplet	0.388	0.81

The poorly resolved features could be interpreted as having peaks at ~2.65 and ~2.8 MHz. If these peaks were part of a triplet in the cancellation condition, i.e., near zero field NQI transitions, they would be accompanied by a low frequency peak at ~0.15 MHz. It is possible that such a peak is present in the 3-pulse ESEEM spectrum (In Figure 5.1, the bottom panel shows an increase in intensity of a very low frequency peak at the longer values of τ), but peaks in this region are very low in intensity. Due to the exponential decrease in echo signal with time, very low frequency features are often unreliable in ESEEM.(*22*) If this triplet was to be considered real, it would be near the limit where η ~0 with K = 0.90 MHz and η = 0.083.(*23*)

2D HYSCORE of the M265IT Q_A Semiquinone

Our 3-pulse ESEEM spectrum of the M265IT mutant had virtually no resolution of the broad double quantum transition that is around 4 MHz in wild type.(*24*) However, the 4-pulse HYSCORE experiment generates correlations between opposite spin manifolds, allowing for positive identification of peaks from the same nucleus. In Figure 5.2, a HYSCORE spectrum of the M265IT mutant shows well defined lines off the diagonal in the (+,+) quadrant that relate to the 0.63 and 0.85 MHz peaks in the (well

resolved) triplet identified in the 3-pulse ESEEM spectrum. These two features are correlated with the double quantum transition at ~5 MHz. While there are many additional contours in the spectrum, there is nothing that can conclusively be associated with a second nitrogen.

$$\nu_{dq^+} = 2[\nu^2_{ef} + \kappa\,]^{1/2} \qquad (2)$$

$$\kappa = K^2(3+\eta^2).$$

Using Equation 2, the double quantum frequency (ν_{dq}) can be combined with the NQI parameters of the triplet (Table 5.1) and the relationship $\nu_{ef} = \nu_N \pm A/2$ to estimate the hyperfine contribution to the spectrum. Using a (ν_{dq}, ν_{dq}) correlation at (5.1, 1.6) MHz from the (-,+) quadrant of the HYSCORE spectrum, a value of A~ 2.7 MHz is calculated.

Uniform ^{15}N labeling eliminates the nitrogen NQI from the spectrum. A spectrum of ^{15}N nuclei coupled to Q_A^- in M265IT (Figure 5.3) shows peaks in the (-,+) quadrant at (+/-3.24, -/+0.34). A HFI value of A = 3.58 MHz (2.56 MHz corrected for ^{14}N nuclei) is determined from the center of the peak maxima (in the (-,+) quadrant the two peaks are centered on $A/2$ and are separated by ν_N). The spectrum shows additional weak features in the (+,+) quadrant. These weak features could be attributable to a second nitrogen, but are not significantly resolved above noise to assign values. Alternatively, given that $|T+2a| \sim 4\nu_N$, peaks from a single ^{15}N nucleus could be in both the (-,+) and (+,+) quadrants. (Discussed in greater detail in Chapter 3)

Analysis of the NQI Parameters

The NQI parameters describe the strength and symmetry of the EFG tensor. The quadrupole coupling constant K is dependent on the quadrupole moment, and the z

component of the EFG tensor (q_{zz}). The magnitude of *K* is characteristic of the type of bonding at the nitrogen nucleus and was used to assign peaks for the wild type to either peptide NH from Ala-M260 or Nδ from His-M219.(*25, 26*) Using Equation 1 and the well resolved frequencies in the M265IT spectra (0.63, 0.85, and 1.48 MHz), *K* = 0.388 MHz was calculated. This is very close to *K* for His-M219 Nδ in wild type (Table 5.1), and these strong peaks in the M265IT spectra were therefore similarly assigned to the His-M219 nitrogen. The *K* value calculated for the poorly resolved peaks (0.15, 2.65 and 2.8 MHz) is 0.9 MHz. This is significantly larger than the value for NH from Ala-M260 in wildtype, or for polyglycine. However, it cannot be ruled out as originating from backbone nitrogen in the M265IT mutant.(*26*)

It is unlikely that the mutation at M265 resulted in a significant chemical change at Ala-M260, and more appropriate interpretations might be that *K* calculated from the low intensity peaks is unreliable, or the hyperfine coupling has changed from the wild type so that cancellation conditions are not met. However, if the HFI between the semiquinone and the Ala-M260 nitrogen is significantly decreased, it could indicate a change in the length of the H-bond to the O1 carbonyl, but it is a stretch to draw any conclusions from values calculated from the low intensity peaks.

The asymmetry parameter, η, is determined by the ratio of the components of the EFG tensor ($(q_{xx} - q_{yy})/q_{zz}$). As described in Chapter 4, an increase in η toward 1 indicates a larger amount of spin density transferred to the external sp^2 orbital of the coupled nitrogen, and/or an increased linearity of the H-bond. Experiments on various Cu-coordinated imidazole derivatives were used to correlate increased occupancy of the external orbital with a larger asymmetry parameter.(*23, 27*) The value, η = 0.81, (from

M265IT 3-pulse ESEEM) (Table 5.1) is significantly decreased from $\eta \sim 1$ calculated for His-M219 Nδ in wildtype. The difference would correspond to an ~50% smaller transfer of spin density to the external orbital (compared to the model compounds with known sp^2 occupancy and with experimentally determined values: $\eta = 1$ versus $\eta = 0$).(*23*) It is possible that an increase in H-bond length or an increase in angle could be responsible for the decrease in η.(*27*) However, in the M265IT mutant it is also possible that the new dipole introduced into the Q_A binding pocket directly affects the electronic structure of the His-M219. The hydroxyl group pointed at the plane of the histidine could result in a change in the electronic structure decreasing the probability of electron occupancy at the external sp^2 orbital through electrostatic interactions.

Analysis of the HFI Parameters

Values of the isotropic hyperfine coupling, *a*, are read from ^{15}N HYSCORE spectra and can be calculated from ^{14}N ESEEM and HYSCORE. For the M265IT mutant, the *a* ~2.7 MHz calculated from ^{14}N spectra is very similar to 2.56 MHz from the ^{15}N spectrum (adjusted for a ^{14}N nucleus). An almost identical hyperfine coupling value of *a* = 2.55 MHz was measured in wild type and assigned to for His-M219. The well resolved features in M265IT ^{14}N spectra were also assigned to His-M219 Nδ based on the quadrupole parameter *K*.

Isotropic hyperfine coupling is due to transfer of *s* spin density from the semiquinone onto the coupled nitrogen. (*28-30*) The similarities between the mutant and wild type HFI indicate that there is little change in the direct spin delocalization across the O4-His(M219) H-bond. This result could be expected if there were only small

structural changes in the quinone binding pocket due to the mutation and the substantial impact on redox potential is from electronic redistribution. However, with poor (or no) resolution of a nitrogen attributable to the M260 NH it is difficult to refute the hypothesis that the H-bond to O1 is lengthened in the mutant. Further examination of this mutant, and calculation of the complete hyperfine tensor(s) will assist in interpretation.

Molecular Dynamics Investigation of M265IT Mutant RCs

The original energy minimizations on this mutant suggested that a H-bond could form between the hydroxyl of Thr-M265 and the backbone O of M261, and have a steric clash between methyl groups on Thr-M265 and M260. The postulated combined effect was to push the protein backbone away from Q_A, lengthening the H-bond from NH of M260 to the O1 carbonyl by ~ 0.1 Å.(*11*) The molecular dynamics (MD) package NAMD has been shown to be a powerful tool in simulating the behavior of enzymes.(*31, 32*) NAMD uses CHARMM potential functions and simulates the movement of proteins based on classical mechanics. RCs with the M265 residue changed to threonine were simulated in a lipid bilayer and water box with 100 mM salt concentration using NAMD.

RC coordinates for MD simulations have been taken from PDB files 1AIG (*7, 33*) and 2J8C (*7, 33*), and (most recently) a currently unpublished crystal structure of M265IT (A. Mattis, personal communication). In order to simulate the semiquinone state, a semiquinone charge set was calculated using the QM program Firefly.(*34*)

A series of MD trajectories was run where the starting orientation of the sidechain of Thr-M265 was varied with some impact on the final structure. When the sidechain was rotated to give the closest contact between the Thr-M265 hydroxyl and the M261

backbone carbonyl (Figure 5.4), the structure remained stable for an entire ~25 ns trajectory. (Figure 5.5) The average lengths of the H-bonds to O4 and O1 of Q_A are 3.02 ± 0.2 Å and 3.05 ± 0.2 Å respectively. (Figure 5.5) In any single trajectory, there was no deviation from this mean that could be related to an interaction between the Thr-M265 sidechain and protein backbone.

Using starting coordinates from the M265IT crystal structure, no stable H-bond was formed between the M265 hydroxyl and M261. (Figure 5.6) The threonine hydroxyl did not start in the ideal H-bonding conformation, compared to the trajectory discussed in the previous paragraph, and rotated further away from the backbone carbonyls to a distance of ~4Å (this result is similar to all trajectories where the starting H-bond length was longer than the ideal conformation). Figure 5.7 shows the distance between the proton on the Thr-M265 hydroxyl and the potential H-bond donors on the backbone. The hydroxyl rotates within the first 50ps and remains in that conformation for the remainder of the ~10 ns trajectory – implying that the orientation of the Thr-M265 OH was not at a reasonable energy minimum in the crystal structure. Visual examination of the trajectory shows that the backbone is substantially perturbed arising from an as yet undetermined source, but H-bond lengths to the quinone carbonyls are still unchanged (average of ~2.9Å for both).

The potential of a direct electrostatic effect from the Thr-M265 hydroxyl was considered in the trajectories that used the M265IT crystal structure coordinates as a starting point. An indication comes from the 3-pulse ESEEM and HYSCORE data, which showed a decrease in the NQI asymmetry parameter in the threonine mutant versus wild type, implying a change in the EFG at the His-M219 Nδ. As a preliminary study,

the pairwise electrostatic interactions between the Thr-M265 and His-M219 sidechains were calculated using NAMD. (Figure 5.8) While the absolute magnitude of these calculations has very little meaning, the differences between wild type trajectories and those of the M265IT mutant are significant. In the mutant, there is an ~2 kcal mol^{-1} energy difference between trajectories with semiquinone versus neutral quinone as Q_A. Similar calculations in trajectories of wildtype reaction centers showed no difference. The decreased redox potential of Q_A in the polar mutants at M265 indicates a relative destabilization of the semiquinone. In M265IT this decrease (≈100 mV) is equivalent to about 2 kcal mol^{-1}. Thus, the dependence of the electrostatic interaction energy between M265 and M219 sidechains on the charge state of Q_A suggests that electrostatics could have an important role in this redox tuning.

Conclusions

Mutations to the M265 residue provide an excellent opportunity to study the relationship between the structure of the RC and quinone function given the large shift in redox potential seemingly caused by small changes in structure. It is almost certain that the introduction of smaller residues at this site will reduce the rigidity of binding of Q_A. The polar hydroxyl on threonine or serine has a specific effect on the function of the quinone in addition to size. 3-pulse ESEEM and HYSCORE measurements of the M265IT mutant show an HFI coupling assigned to the His-M219 Nδ that is indistinguishable from the wildtype value of ~2.5 MHz. The quadrupole coupling constant is also very similar, 0.375 MHz in the mutant versus 0.388 MHz in wildtype. The only significant difference at this nitrogen is the decrease in the asymmetry

parameter to 0.81 in the mutant (from ~1 in wildtype). These results indicate that there is no substantial structural change, but suggests that the newly introduced dipole from the threonine hydroxyl has an electrostatic effect at His-M219. This conclusion is supported by calculations on MD trajectories that show a 2 kcal mol^{-1} difference in the electrostatic interaction energy between the His-M219 and Thr-M265 sidechains depending on the redox state of Q_A.

The large decrease in intensity (or disappearance) of peaks attributable to the M260 peptide NH in the mutant spectra seems to be in contradiction with the relatively subtle changes in the nitrogen coupling to O4. It seems unlikely that any significant structural change could exist that would decouple the peptide nitrogen but leave the histidine nitrogen coupling largely unchanged. It is easier to imagine that features due to the histidine are obscuring peaks from the peptide. Quite a few features in the ^{14}N HYSCORE are difficult to assign, and faint features in the (+,+) quadrant of ^{15}N spectra could be assigned to peptide nitrogen, but are of insufficient intensity above noise to provide meaningful data.

Much work remains to be done on the M265 mutants before any conclusions can be drawn with certainty. However, it seems likely and reasonable that there is a substantial electrostatic effect that disrupts the electronic structure of His-M219. More detailed spectroscopic studies need to be done including examining proton couplings to characterize these mutants. Both protein electrostatics and quantum mechanical calculations should also be performed to determine what effects electrostatics could be expected to have on both the functional redox properties of the quinone and the EPR parameters.

References

1. Feher, G., Allen, J. P., Okamura, M. Y., and Rees, D. C. (1989) Structure and function of bacterial photosynthetic reaction centres, *Nature 339*, 111-116.
2. Feher, G., and Okamura, M. Y. (1978) Chemical composition an properties of reaction centers, In *The Photosynthetic Bacteria* (Clayton, R. K., and Sistrom, W. R., Eds.), pp 349-386, Plenum, New York.
3. Okamura, M., Debus, R. J., Kleinfeld, D., and Feher, G. (1982) Chapter V, In *Function of Quinones in Endergy Conserving Systems* (Tumpower, B. L., Ed.), pp 299-317, Academic Press, New York.
4. Wraight, C. A., and Gunner, M. R. (2009) The Acceptor Quinones of Purple Photosynthetic Bacteria- Structure and Spectroscopy, In *Advances in Photosynthesis and Respiration: The Purple Photosynthetic Bacteria* (Hunter, C. N., Daldal, F., Thurnauer, M., and Beatty, J. T., Eds.), pp 379-405, Springer, Dordrecht, The Netherlands.
5. Allen, J. P., Feher, G., Yeates, T. O., Komiya, H., and Rees, D. C. (1988) Structure of the reaction center from *Rhodobacter sphaeroides* R-26: protein-cofactor (quinones and Fe^{2+}) interactions, *Proc. Natl. Acad. Sci. USA 85*, 8487-8491.
6. Chang, C. H., El-Kabbani, O., Tiede, D., Norris, J., and Schiffer, M. (1991) Structure of the membrane-bound protein photosynthetic reaction center from *Rhodobacter sphaeroides*, *Biochemistry 30*, 5352-5360.
7. Stowell, M. H. B., McPhillips, T. M., Rees, D. C., Soltis, S. M., Abresch, E., and Feher, G. (1997) Light-induced structural changes in photosynthetic reaction center: implication for mechanism of electron-proton transfer, *Science 276*, 812-816.
8. Rinyu, L., Martin, E. W., Takahashi, E., Maróti, P., and Wraight, C. A. (2004) Modulation of the free energy of the primary quinone acceptor (Q_A) in reaction centers from *Rhodobacter sphaeroides*: contributions from the protein and protein-lipid(cardiolipin) interactions., *Biochim. Biophys. Acta 1655*, 93-101.
9. Stilz, H. U., Finkele, U., Holzapfel, W., Lauterwasser, C., Zinth, W., and Oesterhelt, D. (1994) Influence of M subunit Thr222 and Trp252 on quinone binding and electron transfer in *Rhodobacter sphaeroides* reaction centres, *Eur. J. Bioch. 223*, 233-242.
10. Takahashi, E., Wells, T. A., and Wraight, C. A. (2001) Protein control of the redox potential of the primary quinone acceptor in reaction centers from *Rhodobacter sphaeroides*, *Biochemistry 40*, 1020-1028.
11. Wells, T. A., Takahashi, E., and Wraight, C. A. (2003) Primary quinone (Q_A) binding site of bacterial photosynthetic reaction centers: mutations at residue M265 probed by FTIR spectroscopy., *Biochemistry 42*, 4064-4074.

12. McComb, J. C., Stein, R. R., and Wraight, C. A. (1990) Investigations on the influence of headgroup substitution and isoprene side-chain length in the function of primary and secondary quinones of bacterial reaction centers, *Biochim. Biophys. Acta 1015*, 156-171.
13. Wraight, C. A., Vakkasoglu, A. S., Poluektov, Y., Mattis, A. J., Nihan, D., and Lipshutz, B. H. (2008) The 2-methoxy group of ubiquinone is essential for function of the acceptor quinones in reaction centers from *Rba. sphaeroides*, *Biochim. Biophys. Acta 1777*, 631-636.
14. Breton, J., Boullais, C., Burie, J.-R., Nabedryk, E., and Mioskowski, C. (1994) Binding sites of quinones in photosynthetic bacterial reaction centers investigated by light-induced FTIR difference spectroscopy: Assignment of the interactions of each carbonyl of Q_A in *Rhodobacter sphaeroides* using site-specific ^{13}C-labeled ubiquinone, *Biochemistry 33*, 14378-14386.
15. Breton, J., Burie, J.-R., Berthomieu, C., Berger, G., and Nabedryk, E. (1994) The binding sites of quinones in photosynthetic bacterial reaction centers investigated by light-induced FTIR difference spectroscopy: Assignment of the Q_A vibrations in *Rhodobacter sphaeroides* using ^{18}O- or ^{13}C-labeled ubiquinones and vitamin K1, *Biochemistry 33*, 4953-4965.
16. Breton, J., Burie, J.-R., Boullais, C., Berger, G., and Nabedryk, E. (1994) Binding sites of quinones in photosynthetic bacterial reaction centers investigated by light-induced FTIR difference spectroscopy: Binding of chainless symmetrical quinones to the Q_A site of *Rhodobacter sphaeroides*, *Biochemistry 33*, 12405-12415.
17. Breton, J., Nabedryk, E., Allen, J. P., and Williams, J. C. (1997) Electrostatic influence of Q_A Reduction on the IR vibrational mode of the 10a-ester CO of HA demonstrated by mutations at residues Glu L104 and Trp L100 in reaction centers from *Rhodobacter sphaeroides*, *Biochemistry 36*, 4515-4525.
18. Nimz, O., Lendzian, F., Boullais, C., and Lubitz, W. (1998) Influence of hydrogen bonds on the electronic g-tensor and ^{13}C-hyperfine tensors of ^{13}C-labeled ubiquinones — EPR and ENDOR study, *Appl. Magn. Res. 14*, 255-274.
19. O'Malley, P. J. (1998) ^{1}H, ^{13}C, and ^{17}O Isotropic and anisotropic hyperfine couplings for the plastosemiquinone anion radical, *J. Am. Chem. Soc. 120*, 5093-5097.
20. Lubitz, W., and Feher, G. (1999) The primary and secondary acceptors in bacterial photosynthesis III. Characterization of the quinone radicals Q_A^- and Q_B^- by EPR and ENDOR, *Appl. Magn. Reson. 17*, 1-48.
21. Sinnecker, S., Flores, M., and Lubitz, W. (2006) Protein-cofactor interactions in bacterial reaction centers from *Rhodobacter sphaeroides* R-26: effect of hydrogen bonding on the electronic and geometric structure of the primary quinone. A density functional theory study., *Phys. Chem. Chem. Phys. 8*, 5659-5670.
22. Schweiger, A., and Jeschke, G. (2001) *Principles of pulse electron paramagnetic resonance*, Oxford University Press, Oxford, UK.
23. Jiang, F., McCracken, J., and Peisach, J. (1990) Nuclear Quadrupole Interaction in Copper(II)- Diethylenetriamin-Substituted Imidazole Complexes and in Copper (II) Proteins, *J. Am. Chem. Soc. 112*, 9035-9044.

24. Dikanov, S. A., and Tsvetkov, Y. D. (1992) *Electron spin echo envelope modulation (ESEEM) spectroscopy* CRC Press, Boca Raton.
25. Dikanov, S. A., Holland, J. T., Endeward, B., Kolling, D. R. J., Samoilova, R. I., Prisner, T. F., and Crofts, A. R. (2007) Hydrogen bonds between nitrogen donors and the semiquinone in the Q_i-site of the bc_1 complex, *J. Biol. Chem. 282*.
26. Yap, L. L., Samoilova, R. I., Gennis, R. B., and Dikanov, S. A. (2007) Characterization of mutants that change the hydrogen bonding of the semiquinone radical at the Q_H site of the cytochrome bo_3 from *Escherichia coli*, *Journal of Biological Chemistry 282*, 8777-8785.
27. Sinnecker, S., Reijerse, E., Neese, F., and Lubitz, W. (2004) Hydrogen bond geometries from electron paramagnetic resonance and electron-nuclear double resonance parameters: density functional study of quinone radical anion-solvent interactions., *J. Am. Chem. Soc. 126*, 3280-3290.
28. Deligiannakis, Y., Boussac, A., and Rutherford, A. W. (1995) ESEEM study of the plastoquinone anion radical (Q_A^-) in ^{14}N- and ^{15}N-labeled photosystem II treated with cyanide, *Biochemistry 34*, 16030-16038.
29. Deligiannakis, Y., Hanley, J., and Rutherford, A. W. (1999) 1D- and 2D-ESEEM Study of the Semiquinone Radical Q_A^- of Photosystem II, *J. Am. Chem. Soc. 121*, 7653-7664.
30. Martin, E., Samoilova, R. I., Narasimhulu, K. V., Wraight, C. A., and Dikanov, S. A. (2010) Hydrogen bonds between nitrogen donors and the semiquinone in the Q_B site of bacterial reaction centers, *J. Am. Chem. Soc. 132*, 11671-11677.
31. Kale, L., Skeel, R., Bhandarkar, M., Brunner, R., Gursoy, A., Krawertz, N., Phillips, J., Shinozaki, A., Varadarajan, K., and Schulten, K. (1999) NAMD2: Greater scalability for parallel molecular dynamics, *Journal of Computational Physics 151*, 283-312.
32. Phillips, J., Braun, R., Wang, W., Gumbart, J., Tajkhorshid, E., Villa, E., Chipot, C., Skeel, R., Kale, L., and Schulten, K. (2005) Scalable molecular dynamics with NAMD, *Journal of Computational Chemistry 26*, 1781-1802.
33. Koepke, J., Eva-Maria Krammer, E.-M., Klingen, A. R., Sebban, P., Ullmann, G. M., and Fritzsch, G. (2007) pH modulates the quinone position in the photosynthetic reaction center from *Rhodobacter sphaeroides* in the neutral and charge separated states, *J. Mol. Biol. 371*, 13.
34. Granovsky, A. A. Firefly Version 7.1.G, www http://classic.chem.msu.su/gran/firefly/index.html.

Figures

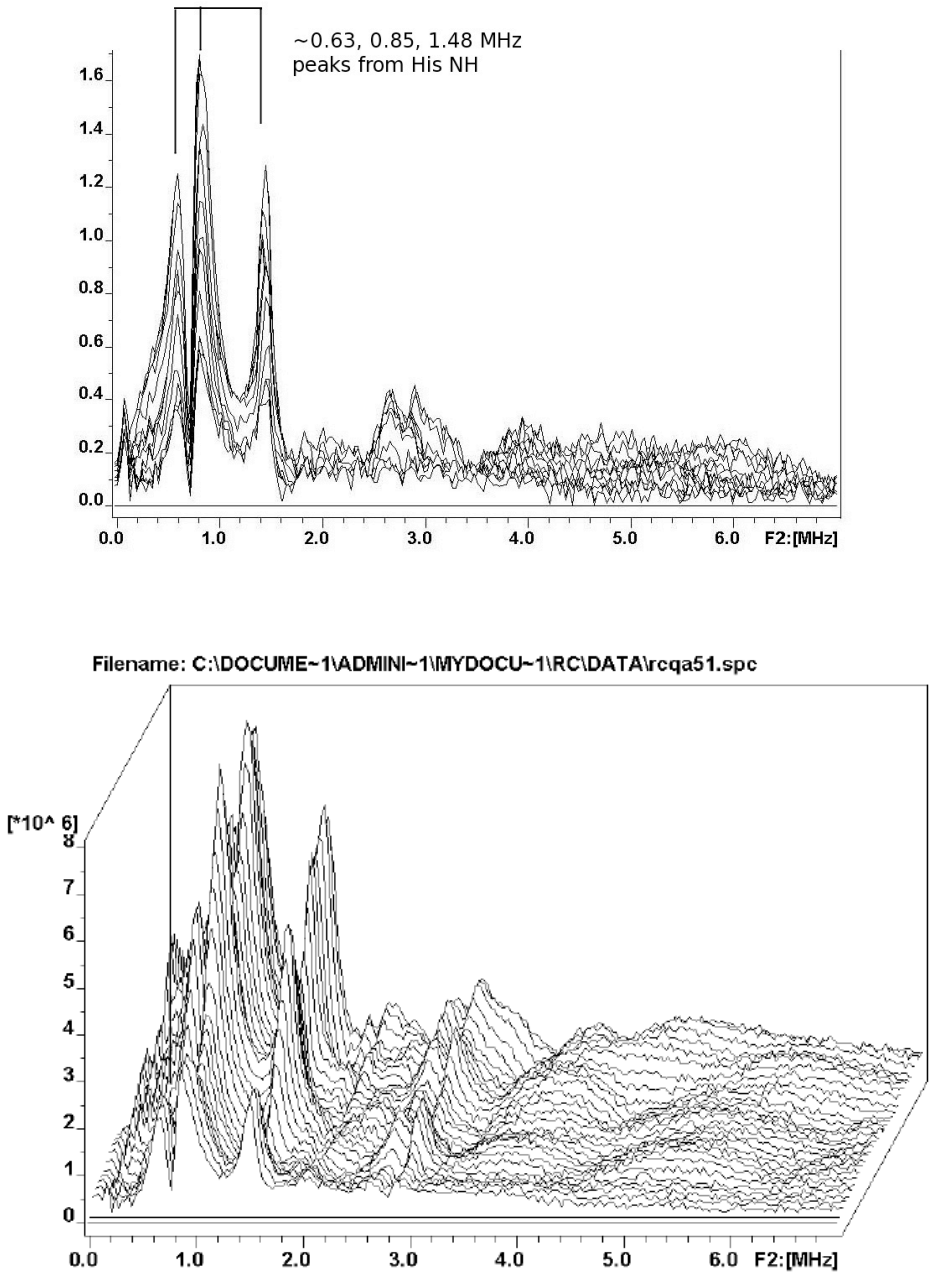

Figure 5.1. The X-band 3-pulse ESEEM spectrum of M265IT Q_A^-, represented as a stacked plot with the initial value of τ=100 ns followed by 16 ns steps. In the flattened view (Top) the peaks assigned to His-M219 are labeled.

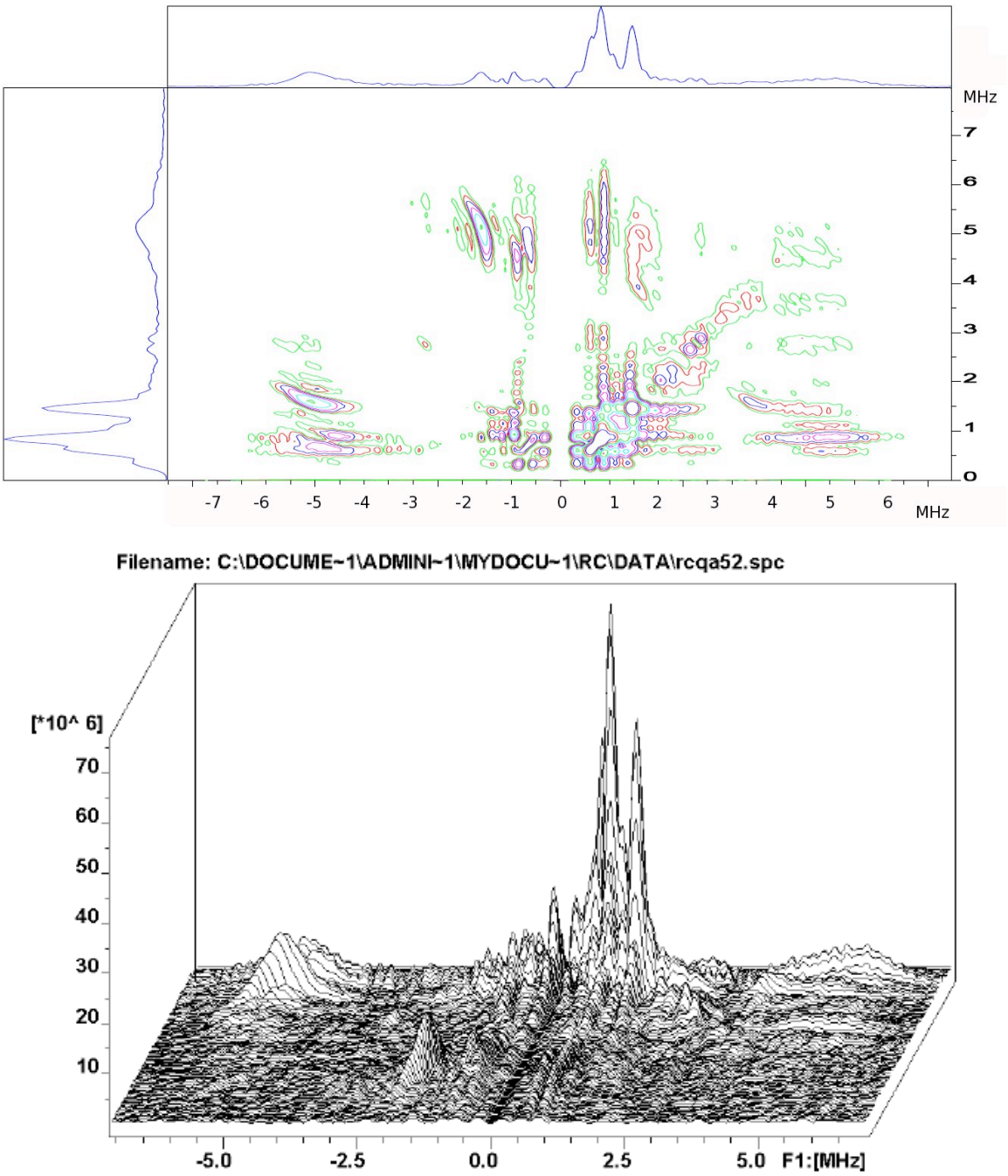

Figure 5.2. 2D ^{14}N-HYSCORE spectrum of Q_A^- in M265IT mutant RCs presented in contour (top) and stacked (bottom) form. τ =136 ns.

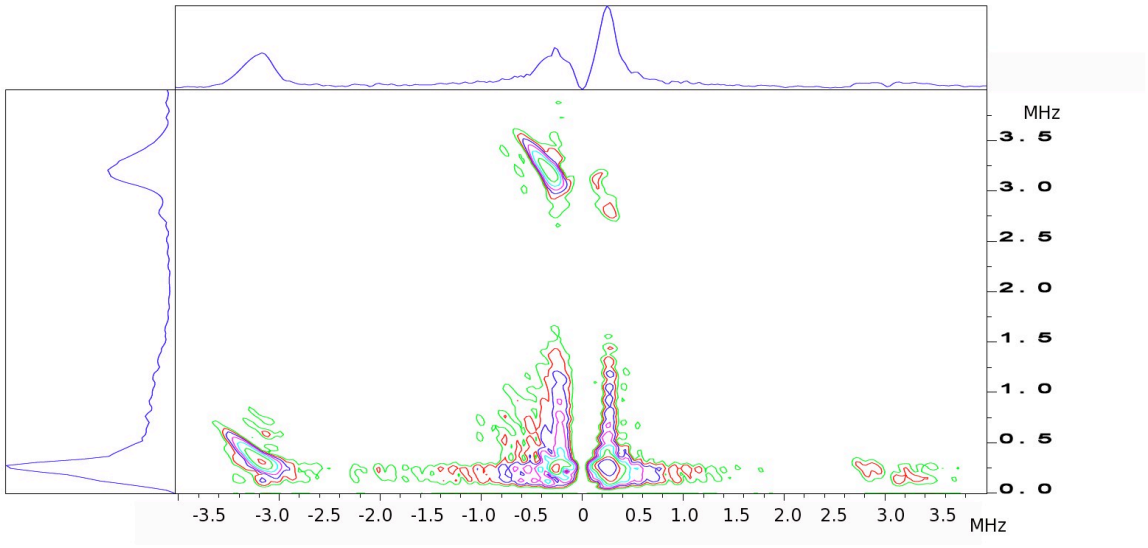

Figure 5.3. 2D HYSCORE spectrum of Q_A^- in ^{15}N labeled M265IT RCs shown as contours. Peaks in the (-,+) quadrant are attributable to His, while (+,+) peaks are very low intensity and could either be additional contributions from His-M219 or a second nitrogen. τ =136 ns.

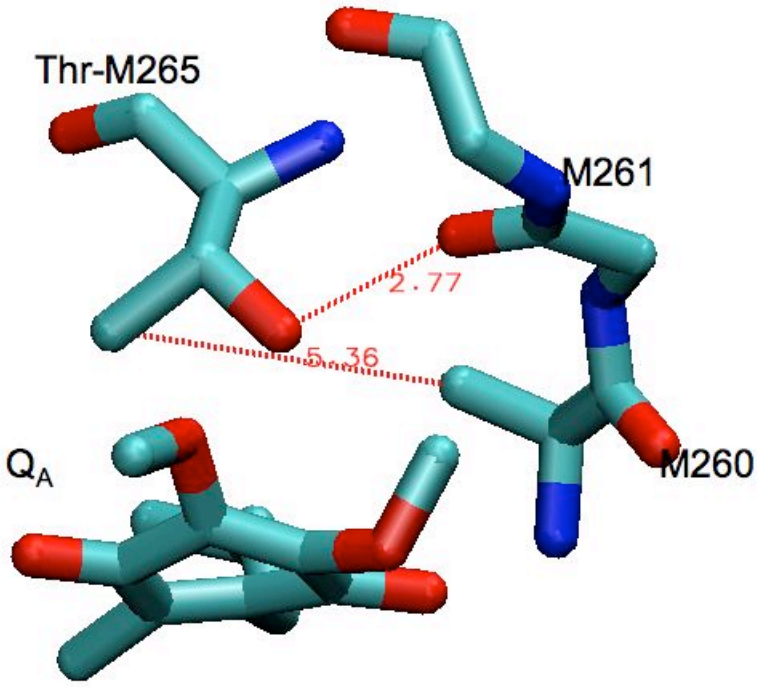

Figure 5.4. When MD trajectories were started with the Thr-M265 hydroxyl as close as was possible by manual sidechain rotation to the M260 backbone carbonyl, a H-bond was present in the majority of frames. The average distance between the hydroxyl oxygen and backbone carbonyl is 2.8 Å. In this simulation, Q_A was neutral.

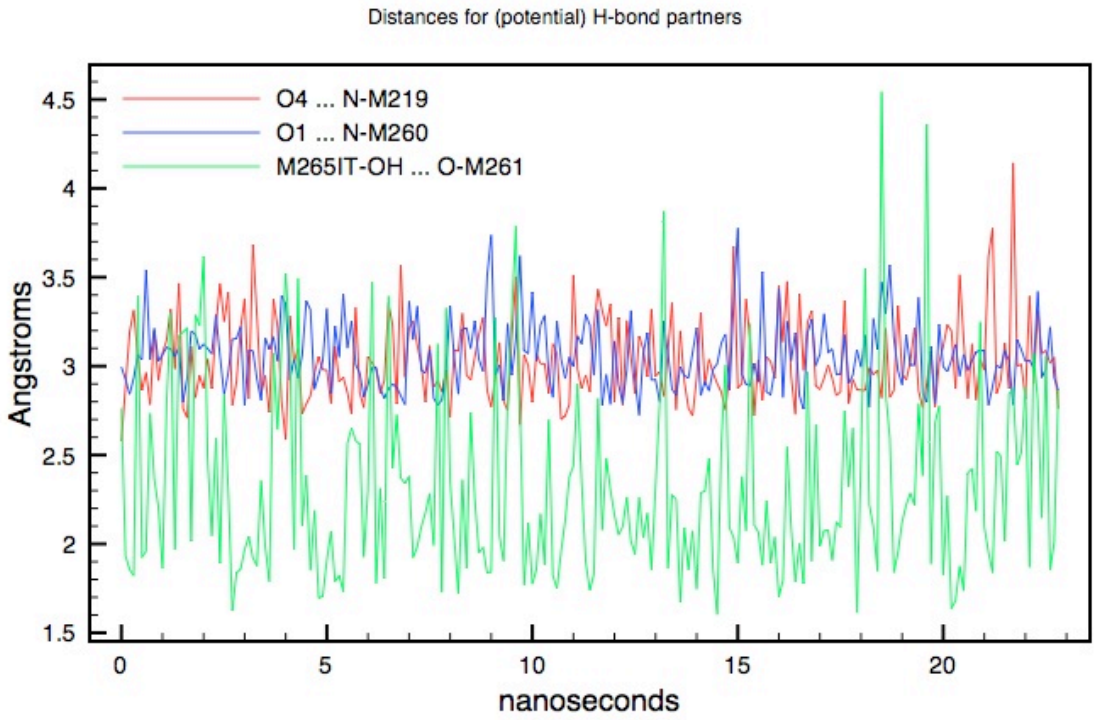

Figure 5.5. In the trajectory where the Thr-M265 hydroxyl to backbone M261 carbonyl distance was minimized, there were still some fluctuations in the H-bond distance shown in green (particularly in the first 10 ns).

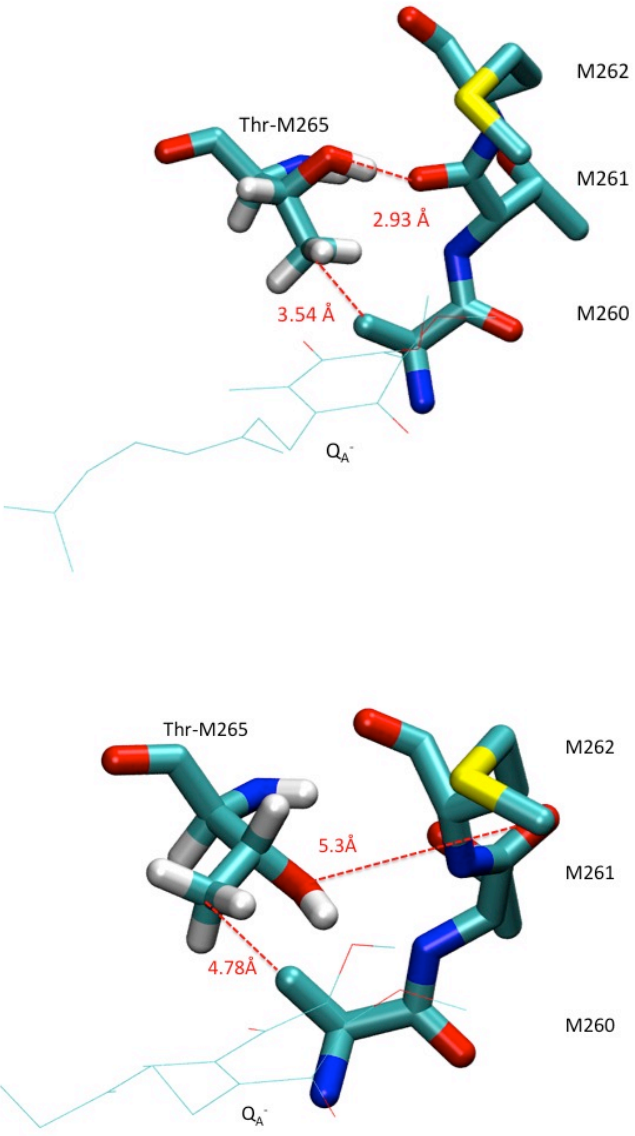

Figure 5.6. The structure of the Q_A^- site from a MD trajectory using starting coordinates from the crystal structure of the M265IT mutant. These two representations show the position at the beginning of the simulations where the coordinates are near to the crystal structure (top) and the hydroxyl at M265 is relatively close to the M261 backbone. At the bottom is the position after the "twist" and movement of the backbone away from M265.

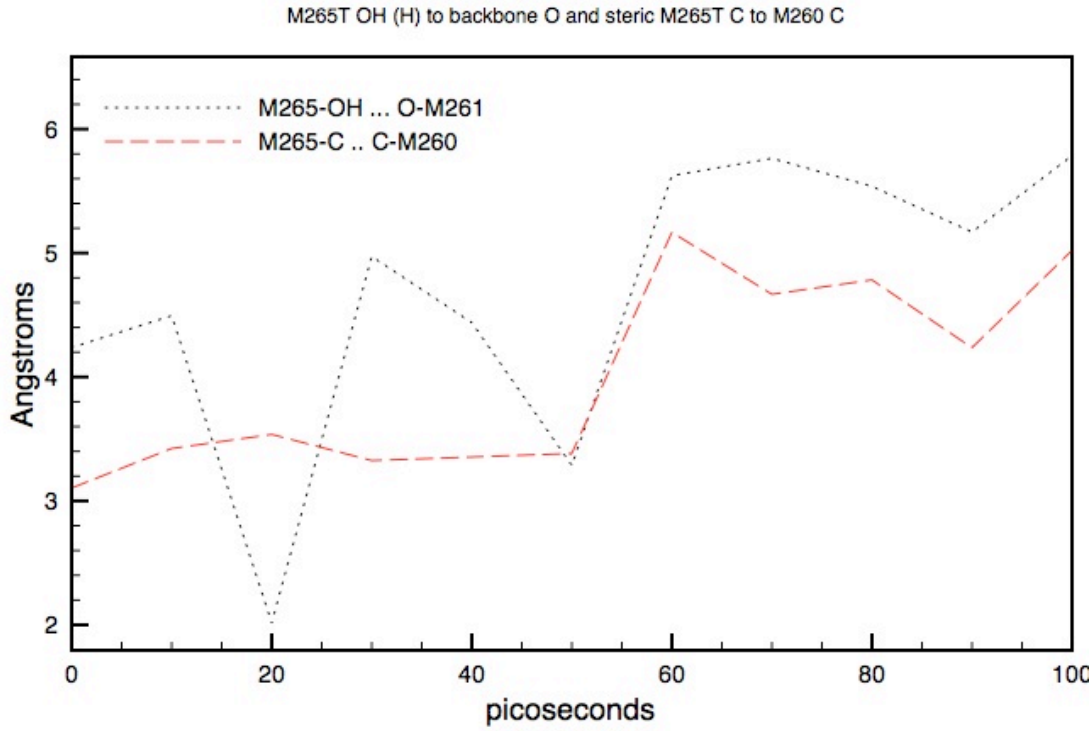

Figure 5.7. The distances between the Thr-M265 OH hydrogen and the backbone carbonyl of M261 and the distance Thr-M265 methyl C and the M260 methyl C are plotted for the first few frames for the trajectory – 100 ps. The sidechain flip, and subsequent backbone movement, is evident very early on, at 50 ps (frame 5) and is stable throughout the trajectory.

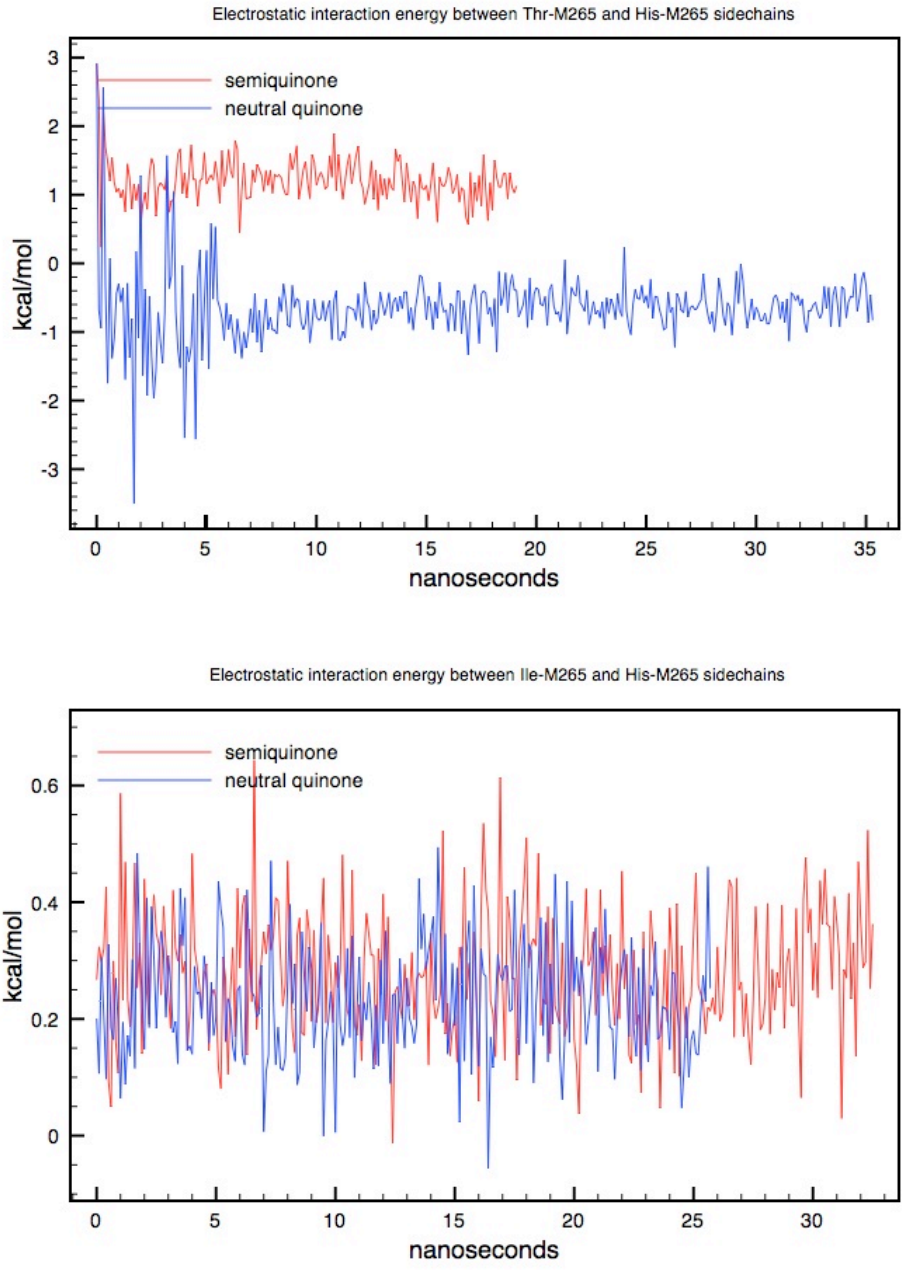

Figure 5.8. The electrostatic interaction energy between the sidechains of M265 and His-M219. Top – M265IT mutant RCs, Bottom – wild type RCs. The red and blue traces represent trajectories with semiquinone and neutral quinone at Q_A respectively.

Chapter 6:

The Protons Hydrogen Bonded to the Q_A and Q_B Semiquinones Studied by Pulsed EPR

Abstract

The HYSCORE experiment is applied here to examine protons coupled to the Q_A and Q_B semiquinones. Three types of protons - matrix, nonexchangeable and exchangeable - are expected contribute to the spectrum. Of particular interest are exchangeable protons that contribute to H-bonds. Exchangeable protons coupled to Q_A^- are analyzed in the context of earlier proton ENDOR studies (discussed in Chapter 3). HYSCORE spectra of the Q_A semiquinone show two exchangeable protons with anisotropic tensor components T in the range 4.6-5.4 MHz, in line with ENDOR data. The Q_B site shows signals from at least three exchangeable protons with the anisotropic component $T \sim 5.2$, 3.7 and 1.9. These signals are compared to combined QM/MM calculations and are assigned to four different protons from Ser-L223, Gly-L225, Ile-L224 and His-L190.

Introduction

The structure and function of the *Rba. sphaeroides* reaction center (RC) have been outlined in Chapter 1, and were introduced in the context of EPR spectroscopy in Chapter 4. The primary quinone, Q_A, is a tightly bound prosthetic group and is singly reduced after photoactivation of the RC. The secondary quinone, Q_B, functions as a two electron mobile carrier and its double reduction is coupled to the uptake of two protons. (*1-4*) The semiquinone, Q_B^-, is a stable intermediate that is tightly bound to the RC.

H-bonding between the protein and both quinones contributes to binding site affinity and, presumably, to the stabilization of the semiquinone species. Pulsed EPR data presented in Chapter 4 described the coupling of Q_A^- and Q_B^- to nitrogen nuclei. The existence of non-zero isotropic hyperfine coupling between the semiquinones and nitrogens indicated the presence of H-bonds. (*5-7*) The data in Chapter 4 showed that both Q_A^- and Q_B^- are strongly coupled to two nitrogen nuclei. Results from nitrogen ESEEM and HYSCORE were interpreted such that both quinones are H-bonded to the protein at the O1 and O4 carbonyls. In the case of Q_A this conclusion is in line with crystal structures and existing EPR data (reviewed in Chapter 3). It has been well established that Q_A^- is H-bonded at the O4 carbonyl to the Nδ of His-M219 and at the O1 carbonyl to the backbone NH of Ala-M260. (*8*) However, the exact H-bond distances and geometry are the subject of debate. (*4*)

Knowledge of H-bonding between the RC and Q_B^- is less certain. ESEEM and HYSCORE presented in Chapter 4, along with published ENDOR results, indicate two H-bonds similar to those of Q_A^- (*7, 9, 10*), but others are not excluded. Crystal structures of RCs containing Q_B have shown significant structural variability and suggest a far more ambiguous H-bonding structure. Q_B has been observed occupying two separate binding pockets labeled "proximal" and "distal". (*8*) Q_A^- has been shown to only be able to transfer electrons to Q_B in the proximal conformation, which is therefore the relevant structure to EPR measurements. In the proximal structure, the O4 carbonyl is H-bonded to the Nδ of His-L190, but the O1 carbonyl appears equally likely to be H-bonded to backbone NH from Ile-L224 or Gly-L225. (*8, 11, 12*) Additionally, the hydroxyl from Ser-L223 is thought to form a H-bond either with the O1 carbonyl or with Asp-L213 and has been implicated in proton transfer to Q_B^-. (*4, 13-15*) A recent RC structure also proposes a H-bond between the backbone NH of Thr-L226 and the Q_B methoxy group at C3. (*12*) It is impossible to definitively correlate ENDOR data, or nitrogen ESEEM and HYSCORE, with specific residues in the Q_B site. Thus, there are potentially as many as five hydrogen bonds to Q_B inferred from crystal structures, but EPR studies have only ever identified up to three. HYSCORE has proven to be effective in separating signals from multiple protons (^{1}H), with different hyperfine couplings, that are hydrogen bonded to semiquinones in the Q_i site of the cytochrome bc_1 complex and the Q_H site in cytochrome bo_3 oxidase. (*16, 17*)

HYSCORE measurements presented in this chapter show that ^{1}H coupled to Q_A^- are in good agreement with previous ENDOR data. HYSCORE has the advantage of not requiring complicated complete deuteration of samples necessary to remove extensive

overlap from non-exchangeable protons in ENDOR. ^{1}H HYSCORE is capable of shedding light on the ambiguous H-bonding structure at Q_B^- with relatively simple sample preparation. ENDOR studies of Q_B^- had shown HFI attributed to three protons, but complete characterization of the tensors was not acheived and the assignments were uncertain. (*9, 15, 18*) Characterization of the protons around Q_B^- by HYSCORE allows resolution of the tensor. Comparison of proton couplings with combined QM/MM calculations (provided by Prof. Patrick O'Malley, University of Manchester, U.K.) allows for assignment of individual exchangeable protons with nuclei identified in crystal structures.

Sample preparation

The growth of *Rba. sphaeroides* cells and preparation of RCs are described in Chapter 2. Generation of the Q_A^- and Q_B^- species are identical to the procedures discussed in Chapter 4 – in fact, the same samples were used in many cases. Samples for Q_A^- proton HYSCORE required uniform ^{15}N labeling. Samples with natural abundance ^{14}N produced deep ESEEM modulations that suppressed the higher frequency modulations due to protons. Cross-suppression effects have been characterized and, in studies of the bc_1 complex iron-sulfur protein, use of ^{15}N labeling was successful in allowing resolution of protons. (*19, 20*) In RC samples, ^{15}N labeling similarly succeeded in dramatically reducing the depth of ESEEM modulations, minimizing cross-suppression. (Figure 6.1).

ESEEM spectra of Q_B^-, in samples with natural abundance ^{14}N, did not show the same remarkably deep modulations seen for Q_A^- (left panel of Figure 6.1), and features

surrounding the ^{1}H Larmor frequency were visible. However, elimination of NQI by using ^{15}N enrichment increased the resolution and intensity of proton features.

^{1}H ENDOR of Q_A^- in the Context of HYSCORE

Protons coupled to Q_A^- have been identified using X-band and Q-band ENDOR. (*9, 21, 22*) At Q-band, orientation selection is possible and, along with complete deuteration of reaction centers, the hyperfine tensors for two coupled protons were characterized. (*22*) These ENDOR data were used to predict the HYSCORE spectrum associated with Q_A^- proton couplings.

The geometry of H-bonds and the proton hyperfine couplings in proteins are both influenced by the environment itself. For Q_A^-, ENDOR spectra indicate three couplings, A_1 = 4.7 MHz, A_2 = 6.3 MHz, and A_3 = 9.0 MHz (+/-0.1 MHz), which have been associated with H-bond protons. (*9, 21, 22*) The two smaller couplings, A_1 and A_2, were assigned to the $A_\perp$ components of the hyperfine tensors from two protons, and A_3 (with low intensity peaks) with contributions from one (or two overlapping) $A_\parallel$ component(s). The time dependence of the ENDOR line intensities, following exchange of $^{1}H_2O$ with $^{2}H_2O$ in fully protonated and fully deuterated RCs, confirmed that the three observed couplings belong to two protons. The $^{1}H/^{2}H$ exchange times for the protons of the Q_A semiquinone were found to be τ_1~50 min and τ_2~1200 min in protonated RCs and τ_1~10 min and τ_2~90 min in fully deuterated RCs. (*22*) Principal values of the anisotropic hyperfine tensors and isotropic couplings determined for these protons from Q-band ENDOR were presented in Chapter 3, Table 3.4.

For both protons identified by ENDOR, the symmetry is approximately axial (anisotropic tensor = {2*T*, -*T*, -*T*}). The proton that exchanged on a slow time scale exhibited nearly exact axial symmetry while the faster exchanging proton showed only a slight, ~4%, departure. For the purpose of HYSCORE estimates, this proton was also considered to have pure axial symmetry with the tensor {9.12, -4.56, -4.56} MHz. The proton Larmor frequency at X-band is ~ 14.7 MHz and, in a HYSCORE spectrum that meets the condition where $|T + 2a| < 4\nu_N$, all proton peaks are expected to be in the (+,+) quadrant where the condition $\nu_{\alpha(\beta)} = \nu_N \pm A/2$. (*23*) Using this relationship, and the components of the HFI tensor from ENDOR data ($A_\perp = a - T$, $A_\parallel = a + 2T$), the related HYSCORE frequencies associated with parallel and perpendicular components of the hyperfine tensor were calculated. (Table 6.1)

Table 6.1. ENDOR derived parallel and perpendicular hyperfine frequencies (MHz) for protons H1 and H2[a] *(15)*

Proton	H-bond	$A_\perp=a-T$	$A_\parallel=a+2T$	$\nu_{\alpha\parallel}$	$\nu_{\beta\parallel}$	$\nu_{\alpha\perp}$	$\nu_{\beta\perp}$
H1	O4–His (M219)	-6.50	9.15	19.29	10.15	11.47	17.97
H2	O1–Ala (M260)	-4.73	8.95	19.2	10.24	12.36	17.08

[a] parallel and perpendicular hyperfine frequencies were calculated for proton Zeeman frequency ν_I=14.73 MHz

HYSCORE crossridges in the (+,+) quadrant will be centered on the Larmor frequency and extend between ($\nu_{\alpha(\beta)\parallel}$, $\nu_{\beta(\alpha)\parallel}$) and ($\nu_{\alpha(\beta)\perp}$, $\nu_{\beta(\alpha)\perp}$). The idealized location of crossridges

and simulated HYSCORE spectra (using τ = 136ns) were calculated[1] using the ENDOR-derived parameters and are presented in Figure 6.2. In HYSCORE spectra, crossridge intensities are suppressed in the region of the Larmor frequency, along the diagonal, in a manner that is dependent on the values of τ used in the measurements. The effect of the suppression is the appearance of "tails" from the crossridges located symmetrically on either side of the diagonal (Figure 6.2, panels B, D, F). In order to maximize the resolution of features in experimental spectra, data is often obtained by taking measurements at multiple values of τ. These data can be presented either as unique spectra or as a sum of multiple τ values.

Isotropic and anisotropic components of the HFI tensor can be extracted from ^{1}H HYSCORE using the theoretical analysis outlined in Chapter 3. Arbitrary points (with coordinates ν_1, ν_2) were chosen along the crossridges in the simulated HYSCORE spectrum (Figure 6.2F). Above the diagonal, ν_1 is taken as the larger frequency and assigned to the nuclear manifold ν_α, whereas ν_2 is the smaller frequency and is assigned to ν_β. On the opposite side of the diagonal frequencies ν_1 and ν_2 are similarly chosen, but now the smaller frequencies are assigned to ν_α and the larger frequencies to ν_β. When plotted as ν_α^2 versus ν_β^2, frequencies from individual nuclei are linearly related as shown in Equation 1, with the slope and intercept given by $Q_{\alpha(\beta)}$ and $G_{\alpha(\beta)}$ respectively.

[1] Calculated HYSCORE spectra were obtained using custom software developed by Dr. Alexei Tyryshkin (currently at Princeton University).

$$\nu_\alpha^2 = Q_\alpha \nu_\beta^2 + G_\alpha$$
$$Q_\alpha = \frac{T + 2a - 4\nu_N}{T + 2a + 4\nu_N} \qquad (1)$$
$$G_\alpha = 2\nu_N \left(\frac{4\nu_N^2 - a^2 + 2T^2 - aT}{T + 2a + 4\nu_N} \right)$$

Figure 6.3 shows frequencies from the simulated HYSCORE spectra plotted as ν_α^2 versus ν_β^2 and demonstrates how a linear regression is used to identify the crossridge "tails" associated with a single nucleus. In Figure 6.3 these are labeled **1** and **1'** and **2** and **2'** and relate to the similarly labeled ridges in Figures 6.2 B, D and F. The linear relationship shows that **1** and **1'** are two features from the same proton, and the same is concluded for **2** and **2'**. The curve shown in bold in Figure 6.3 is $\nu_\alpha + \nu_\beta = 2\nu_N$, and the two points where this curve crosses a plot of ν_α^2 versus ν_β^2 indicates the two solutions for *a* and *T* that are obtained by solving Eqn. 1. For an axially symmetric hyperfine tensor, there are two possible assignments of the perpendicular and parallel orientation and consequently two sets of hyperfine tensors for each orientation. Table 6.2 shows values of *a* and *T* obtained from solving Eqn. 1.

Table 6.2. Parameters derived from contour lineshape analysis of the HYSCORE spectrum in Figure 6.2F.

Proton	Q_α (error)	G_α, MHz^2 (error)	*a, T* MHz	$A_\perp = a - T$, MHz (exptl)	$A_\parallel = a + 2T$, MHz (exptl)
H1 (ridges $\mathbf{1}_{\alpha\beta}$,$\mathbf{1'}_{\alpha\beta}$)	-1.10 (0.002)	487.04 (0.53)	∓4.04, ±5.17 **∓1.13, ±5.17**	∓9.2 **∓6.3** **(6.5)**	± 6.3 **±9.2** **(9.15)**
H2 (ridges $\mathbf{2}_{\alpha\beta}$,$\mathbf{2'}_{\alpha\beta}$)	-1.13 (0.004)	486.41 (0.78)	∓4.13, ±4.65 **∓0.52, ±4.65**	∓8.8 **∓5.2** **(4.73)**	± 5.2 **± 8.8** **(8.95)**

Solutions for *a* and *T* presented in Table 6.2 in bold show values that agree well with the parameters calculated from orientation selected Q-band ENDOR.(*22*) If frequencies from the crossridge "tails" on only one side of the diagonal are used for linear regression, similar values of *a* and *T* are obtained ($a = \mp 1.76$, $T = \pm 5.15$ for H1 and $a = \mp 0.61$, $T = \pm 4.42$ for H2), showing that only one side of the diagonal may suffice for analysis.

Q_A Semiquinone ^{1}H HYSCORE

Simulating HYSCORE spectra from proton hyperfine tensors reported from Q-band ENDOR experiments provides a good estimate of what can be expected from

exchangeable protons in experimental HYSCORE on Q_A^-. The frequencies associated with the parallel components of the hyperfine tensor ($\nu_{\alpha\|}$ and $\nu_{\beta\|}$) of the two protons are very similar (Table 6.1) and manifest in the simulated HYSCORE spectrum as overlapping features (labeled (**1**+**2**) in Figures 6.2E and 6.2F). It is expected that Q_A^- ^1H HYSCORE will contain three separated ridges corresponding to **1'**, **2'** and (**1**+**2**) in Figure 6.2E and 6.2F. The presence of two protons is clear from the separation of the perpendicular components generating crossridges **1'** and **2'**.

Experimental HYSCORE data will contain crossridges surrounding the proton Larmor frequency from strongly coupled exchangeable protons participating in H-bonding with the semiquinone and from nonexchangeable protons on methyl and methylene groups of the semiquinone. Exchanging the sample with ^2H_2O buffer will eliminate features attributable to the exchangeable protons, allowing for their identification. Protons with very little anisotropy will appear as nearly linear ridges normal to the diagonal and on either side, but not crossing it (due to suppression effects). Anisotropy will cause curvature in the ridges and lift them above the antidiagonal. (*23*)

HYSCORE spectra were taken with three values of τ = 136, 200, 400 ns to ensure adequate representation of all portions of the cross ridges. (Figure 6.4) The spectra from all recorded values of τ showed different relative peak intensities, but did not include any features absent in the spectrum recorded at only τ = 136 ns. (Figure 6.5)

The data presented in Figures 6.4 and 6.5 show up to four pairs of resolved crossridges when measured in ^1H_2O buffer, designated $\mathbf{1_A}$, $\mathbf{2_A}$, $\mathbf{3_A}$ and $\mathbf{4_A}$. Figures 6.4A, B and 6.5A, B show only the tails of the crossridges appearing above the diagonal in order to zoom in to accentuate ridge details, and the stacked presentations (Figures 6.4C,

D and 6.5C, D) illustrates how the ridges are symmetric around the diagonal (also rotated 90 degrees for clearer presentation). The ridge labeled $\mathbf{1_A}$ has an extended arch located above the antidiagonal, and is separated from the other features. Departure from the antidiagonal and extensive curvature is indicative of large hyperfine anisotropy. (*23*) The features labeled $\mathbf{2_A}$ and $\mathbf{3_A}$ both were located above the antidiagonal and show some curvature. In contrast, the ridge labeled $\mathbf{4_A}$ appeared nearly linear and normal to the diagonal, suggesting small anisotropy.

After overnight ^2H_2O buffer exchange, a significant portion of the exchangeable protons are expected to be exchanged for deuterons and the related HYSCORE features will be diminished. Figures 6.4B and 6.5B show the ridges above the antidiagonal after deuterium exchange. Ridge $\mathbf{2_A}$ nearly completely disappeared in Figure 6.5B and is therefore attributable to an exchangeable proton(s). Ridges $\mathbf{1_A}$ and $\mathbf{3_A}$ both are significantly diminished. Given the significantly different exchange rates reported for the two protons from ENDOR studies, it is reasonable to conclude that these features are also from exchangeable protons but that the exchange is incomplete. However, $\mathbf{4_A}$ is unchanged indicating it originates from non-exchangeable protons on the semiquinone. The intensity of the peak on the diagonal (bottom right corner of each panel), which arises from protons with weak HFI, is diminished in ^2H_2O samples, suggesting the presence of some weakly coupled, exchangeable protons.

HYSCORE simulations presented in Figure 6.2E and 6.2F suggest the assignment of crosspeaks attributable to exchangeable protons in the experimental HYSCORE. The large feature, $\mathbf{1_A}$, exhibited extensive curvature and was similar to the overlap peak $\mathbf{(1+2)_{\alpha\beta}}$ in the simulation, which includes contributions from two protons. Then,

crosspeaks $\mathbf{2}_\mathbf{A}$ and $\mathbf{3}_\mathbf{A}$ should relate to $\mathbf{2'}_{\beta\alpha}$ and $\mathbf{1'}_{\beta\alpha}$, respectively. Points were chosen from these features and the frequencies were plotted as ν_α^2 versus ν_β^2, in the process outlined for the simulated HYSCORE spectra in Figure 6.2F. Experimental HYSCORE data for Q_A^- are shown in Figure 6.6. In this figure, the large and small coordinates from $\mathbf{2}_\mathbf{A}$ and $\mathbf{3}_\mathbf{A}$ are permuted such that they will appear below the diagonal to show any correlations with $\mathbf{1}_\mathbf{A}$. Figure 6.6 shows that points from permuted $\mathbf{2}_\mathbf{A}$ and $\mathbf{3}_\mathbf{A}$ coordinates fall along two separate lines that run through the points from $\mathbf{1}_\mathbf{A}$ located above the diagonal. The linear relationship confirms the conclusion that $\mathbf{2}_\mathbf{A}$ and $\mathbf{3}_\mathbf{A}$ are from two protons and that $\mathbf{1}_\mathbf{A}$ contains overlapping contributions from both. The ridge labeled $\mathbf{4}_\mathbf{A}$ is produced by nonexchangeable protons that have very little anisotropy, producing cross features that are symmetric to the diagonal but do not cross it. (*23*) Only one cross feature for $\mathbf{4}_\mathbf{A}$ (located above the diagonal in Figure 6.6) is used for linear regression.

Two sets of *T* and *a* are obtained from solutions to Eqn. 1 using the slope and intercept of the three lines in Figure 6.6. Exchangeable protons are labeled $H1_A$ (from ridges $\mathbf{1}_\mathbf{A}$ and $\mathbf{3}_\mathbf{A}$) and $H2_A$ (from ridges $\mathbf{1}_\mathbf{A}$ and $\mathbf{2}_\mathbf{A}$). A third, nonexchangeable proton $H3_A$ is associated with ridge $\mathbf{4}_\mathbf{A}$. The results are shown in Table 6.3. The correct solutions for *T* and *a* were chosen based on orientation selected ENDOR data and numerical simulations of HYSCORE data.

Table 6.3. Characteristics of hyperfine tensors of the protons $H1_A$-$H3_A$ derived from experimental HYSCORE spectra of Q_A^-.

Proton(s)	a, T (MHz)	$A_\perp = a - T$ (MHz)	$A_\parallel = a + 2T$ (MHz)
$H1_A$ (ridges **1_A**,**3_A**)	−1.38**,** 5.41	-6.8	9.6
$H2_A$ (ridges **1_A**,**2_A**)	-0.17, 5.07	-5.2	10
$H3_A$ (ridge **4_A**)	4.39, 1.71	2.7	7.8
$H3_A$ (ridge **4_A**)[a]	4.0**,** 1.6	2.4	7.2

[a]sample in ^2H_2O;

HYSCORE spectra simulated for $H1_A$ and $H2_A$ using the rejected solutions with large isotropic constants (a = 4.03 and 4.9 MHz for $H1_A$ and $H2_A$ respectively) contain only sub-ridges similar to $\mathbf{1}_{\alpha\beta(\beta\alpha)}$ and $\mathbf{2}_{\alpha\beta(\beta\alpha)}$ in Figure 6.2 while sub-ridges $\mathbf{1'}_{\alpha\beta(\beta\alpha)}$ and $\mathbf{2'}_{\alpha\beta(\beta\alpha)}$ are absent, in contrast to the experimental spectra and the spectra simulated with the preferred parameter set. Additionally it can be noted that the large isotropic HFI measured for coupled nitrogen nuclei, presented in Chapter 4, indicate that protons participating in the same H-bond should have small isotropic HFI. Positive spin-density transferred onto the nitrogen by spin polarization mechanisms equates to negative spin

density transferred onto the proton. The result is cancellation of isotropic HFI due to positive spin directly transferred and negative spin transferred by spin polarization.(*5, 6*)

Q_B Semiquinone ^{1}H HYSCORE

Hyperfine couplings A_1 = 3.1 MHz and A_2 = 5.0 MHz have been identified for Q_B^- in X- and Q-band ENDOR experiments. Different ^{2}H exchange times indicated that different protons contribute to each couplings. (*9, 15, 18*) ^{1}H HYSCORE provides new information about protons coupled to Q_B^-, and analysis using Eqn. 1 can resolve the hyperfine anisotropy. Figure 6.7 shows the contour and stacked presentations of the ^{1}H HYSCORE spectra recorded with τ = 136, 200 and 400 ns. Unlike spectra presented for Q_A^-, suppression effects mask some features from individual spectra recorded at τ = 136 ns and all three delay times (τ = 136, 200, 400 ns) are needed for analysis.

Six pairs of crossridges, labeled **1_B – 6_B** can be identified in Figure 6.7. Crossridge **1_B** exhibited the same extensive curvature and position away from the antidiagonal as the **1_A** feature in spectra of Q_A^-, indicating extensive anisotropy. Adjacent to **1_B** is a ridge that could be interpreted as being a single feature, but close examination of the location and lineshape of the crossridges in Figure 6.7C shows it to represent two overlapping tails, labeled **2_B** and **3_B**. The ridges **4_B** and **5_B** are unique to Q_B^-. Both are close to the antidiagonal and exhibit only minor curvature. Located on the antidiagonal and nearly linear is a crossridge labeled **6_B**, which is analogous to **4_A** seen in Q_A^- HYSCORE. Figure 6.7B and 6.7D show the HYSCORE spectrum after overnight exchange in ^2H_2O; the only remaining intensity is from the ridge **6_B** and on the diagonal.

Frequencies from the crossridges **1$_B$** – **6$_B$** are plotted as ν_α^2 versus ν_β^2 in Figure 6.8, showing correlations between the crossridges. The frequencies chosen for **2$_B$** and **4$_B$** were permuted so that they fall on the lower side of the diagonal. Features labeled **1$_B$** and **2$_B$** fall on one line and **3$_B$** and **4$_B$** fall on another line. In terms of the ridge designations in Figure 6.2, **1$_B$** and **2$_B$** correspond to **1$_{\alpha\beta}$** and **1'$_{\beta\alpha}$** for one proton, $H1_B$, and **2$_B$** and **4$_B$** to **2$_{\alpha\beta}$** and **2'$_{\beta\alpha}$** for a second proton, $H2_B$. The ridges labeled **5$_B$** and **6$_B$** have no counterparts that can be generated opposite of the diagonal. **5$_B$** is presumed to originate from a third exchangeable proton, $H3_B$, with low anisotropy compared to $H1_B$ and $H2_B$. The ridge **6$_B$** is from a nonexchangeable proton, $H4_B$, and is similar to $H3_A$ in Q_A^- spectra. Preferred solutions to Eqn. 1 are presented in Table 6.4 for $H1_B$ – $H4_B$.

Table 6.4. Characteristics of hyperfine tensors of the protons $H1_B$-$H4_B$ derived from experimental HYSCORE spectra of Q_B^-.

Proton	*a, T* MHz	$A_\perp = a - T$ MHz	$A_\parallel = a + 2T$ MHz
$H1_B$ (ridges **1_B,2_B**)	–0.83, 5.2	–6.0	9.6
$H2_B$ (ridges **3_B,4_B**)	-0.88**,** 3.71	–4.6	6.5
$H3_B$ (ridges **5_B**)	1.09, 1.87	–0.8	4.9
$H4_B$ (ridges **6_B**)	4.27, 1.92	2.4	8.1
$H4_B$ (ridges **6_B**)[a]	4.8, 1.6	3.2	8.0

[a]sample in ^2H_2O;

Similar to the Q_A^- hyperfine values presented in Table 6.3, the preferred solution for *T* and *a* are the solutions to Eqn. 1 with lower isotropic HFI couplings. However, the Q_B site has not been as extensively studied with orientation selected Q-band ENDOR and the selections in Table 6.4 aren't confirmed by any existing data.

Discussion

Exchangeable protons observed in ^{1}H HYSCORE are presumed to contribute to H-bonding to the RC acceptor quinones. HYSCORE studies of Q_A^- are consistent with published ENDOR data. (*21, 22*) Two protons, $H1_A$ and $H2_A$ from HNδ of His-M219 and NH Ala-M260 respectively, are involved in H-bonding and have similar anisotropic HFI couplings T~5.1-5.4 MHz. However, X-band HYSCORE spectra of Q_A^- do not have high enough resolution to fully differentiate between individual crosspeaks without the aid of models built on Q-band ENDOR data. The HYSCORE signal is broadened by a static distribution of HFI parameters that likely contributes to line broadening. Q-band ENDOR of the protons contributing H-bonds to the Q_A semiquinone indicated that this distribution should not exceed ±5%. (*22*) A static HFI distribution could contribute up to 0.5 MHz broadening for a value of T ~5MHz and could effectively obscure the resolution in a powder type X-band spectrum of individual features from protons with very similar HFI couplings as indicated in Table 6.1.

HYSCORE data presented here agree with the current picture of the Q_A site that has one H-bond to each quinone carbonyl oxygen. (Table 6.2) The two protons have similar anisotropic HFI, but the isotropic HFI is significantly larger, -1.38 MHz, for the proton associated with the hydrogen bond to the O4 carbonyl than for the proton H-bonded to O1, -0.17 MHz. Despite the similar anisotropy, the larger (more negative) isotropic HFI for His-M219 indicates that more spin density is transferred through this H-bond to the Nδ atom.

^{1}H HYSCORE of Q_B^- is presumably susceptible to the same broadening apparent in the spectra of Q_A^- but appears not to suffer from the same overlap of crossridges. Two

sets of crosspeaks in the Q_B^- spectra showed significant anisotropy (identified as $H1_B$ and $H2_B$). Both showed similar values of $a \sim -0.8$ MHz but different anisotropic HFI $T = 5.2$, 3.7 MHz. No experimental data exist to aid in the assignment of features in Q_B^- HYSCORE, but it is clear that there are more than two H-bonds, based on the identification of $H1_B$-$H3_B$.

In order to aid in the assignment of features from HYSCORE measurements, they were compared with values obtained from combined QM/MM calculations, performed by P. O'Malley and T. Lin (U. Manchester, U.K.). Calculated values for HFI in the Q_A site have been already reported(*24*) and similar calculations for the Q_B site were performed using a model of the Q_B site based on the 1dv3.pdb X-ray structure.(*11*) These are shown in Table 6.5.

Table 6.5. Calculated ^{1}H hyperfine couplings (MHz) for the Q_A and Q_B site hydrogen bonding interactions.

Q_A site			Q_B site		
Position	**Anisotropic** T_{33}, T_{22}, T_{11}	**Isotropic**	**Position**	**Anisotropic** T_{33}, T_{22}, T_{11}	**Isotropic**
^{1}HN Ala-M260	9.3 -4.7 -4.6	-1.8	^{1}HN Gly-L225	6.6 -3.7 -2.9	-0.6
^{1}HN His-M219	10.4 -5.3 -5.0	0.6	^{1}HN His-L190	10.2 -5.3 -4.9	-0.4
			^{1}HN Ile-L224	3.9 -2.1 -1.8	-0.1
			^{1}HO Ser-L223	7.6 -4.0 -3.7	-0.8

In the anisotropic tensors presented in Table 6.5, T_{33} is equal to the maximum component of the anisotropic hyperfine tensor ($2T$ for axial symmetry). The anisotropic

coupling calculated for protons associated with His-M219 and Ala-M260 in the Q_A site, 5.2 and 4.65 MHz respectively, are in fairly good agreement with the experimental values, 5.4 and 5.1 MHz ($H1_A$ and $H2_A$ in Table 6.3). The assignment of $H1_A$ to the His-M219 HNδ and $H2_A$ to Ala-M260 NH appears reasonable in the context of these calculated values.

Combined QM/MM calculations predict strong interactions between protons of His-L190, Gly-L225 and Ser-L223 and Q_B^-, and an additional weak coupling with Ile-L224. The four potential H-bonds to Q_B^- should create a very different spectrum than the structure of Q_A^-, so the simulated spectra in Figure 6.2 provide very little analytical benefit. However, unlike Q_A^- spectra, the peaks from Q_B^- are sufficiently separated to be analyzed on their own. HNδ from His-L190 shows the largest value of T = 5.1 MHz in calculations and is in good agreement with $H1_B$. Anisotropic HFI couplings calculated for Gly-L225 HN and Ser-L223 OH are very similar (3.3-3.8 MHz), and proton $H2_B$, which has T = 3.7 MHz (Table 6.4), could contain contributions from both L225 and L223 protons. Figure 6.9 shows simulated HYSCORE spectra for the exchangeable protons of Q_B^- using the hyperfine tensors given in Table 6.5, and shows that $H2_B$ is likely to be from the two overlapping protons.

Proton $H3_B$, with small T ~1.9 MHz, is likely from the backbone peptide of L224. The assignment of H-bonds to both L224 and L225 is in agreement with N HYSCORE presented in Chapter 4. (See Chapter 4. Figures 4.7 and 4.8) While only one peptide nitrogen is seen with significant hyperfine coupling, both ^{14}N and ^{15}N HYSCORE show a significant feature centered at the nitrogen Larmor frequency. These features are sufficiently broad to include a weakly coupled peptide N from L224.

Conclusions

^{1}H HYSCORE was able to provide extensive information about the hyperfine tensors of protons coupled to both RC acceptor quinones. Spectra of Q_A^- were in good agreement with proton HFI reported for Q-band ENDOR. (*21, 22*). Obtaining the ^{1}H HYSCORE spectra did not require complete deuteration of RCs and quinones, but the exchangeable protons did overlap and meaningful interpretation would have been difficult without comparison to ENDOR data. In HYSCORE spectra of Q_B^-, we were able to resolve previously unreported HFI couplings. Crystal structures have suggested the possibility of up to five H-bonds between the protein and Q_B but only two have been consistently reported. HYSCORE measurements showed at least three exchangeable protons. When analyzed in the context of combined QM/MM measurements, it was apparent that $H1_B$-$H3_B$ could originate from four H-bonds. It is also possible that a H-bond between the Thr-L226 NH and a methoxy oxygen could show very small transfer of unpaired spin density and therefore not be observed in EPR measurements.

It has been proposed that the symmetry of electron spin density is significantly different between Q_A^- and Q_B^- and could contribute to the different functions of the two quinones. (*9*) The H-bond between Q_A^- and His-M219 draws more spin density than the H-bond to Ala-M260 and polarizes Q_A^- in the direction of electron transfer. In contrast, the strong H-bond between L190 and the Q_B semiquinone is balanced by multiple H-bonds at the O1 carbonyl. The Q_B semiquinone O1 carbonyl has strong H-bonds to both OH of Ser-L223 and HN of Gly-L225 and an additional weak H-bond to backbone L224 compared to the single H-bond between Q_A^- O1 and M260. The result of the multiple H-

bonds to Q_B^- is a highly symmetric electronic density distribution. This symmetry mimics what would be expected of a ubisemiquinone in protic solvent, which – much like Q_B – is readily doubly reduced. The differences in H-bonding structure between the two RC quinones can be expected to aid in the generation of an electronic environment that facilitates their unique functions.

References

1. Okamura, M., Debus, R. J., Kleinfeld, D., and Feher, G. (1982) Chapter V, In *Function of Quinones in Endergy Conserving Systems* (Tumpower, B. L., Ed.), pp 299-317, Academic Press, New York.
2. Okamura, M. Y., Paddock, M. L., Graige, M. S., and Feher, G. (2000) Proton and electron transfer in bacterial reaction centers, *Biochim. Biophys. Acta 1458*, 148-163.
3. Wraight, C. A. (2004) Proton and electron transfer in the acceptor quinone complex of photosynthetic reaction centers from *Rhodobacter sphaeroides*, *Frontiers Biosci. 9*, 309-337.
4. Wraight, C. A., and Gunner, M. R. (2009) The Acceptor Quinones of Purple Photosynthetic Bacteria- Structure and Spectroscopy, In *Advances in Photosynthesis and Respiration: The Purple Photosynthetic Bacteria* (Hunter, C. N., Daldal, F., Thurnauer, M., and Beatty, J. T., Eds.), pp 379-405, Springer, Dordrecht, The Netherlands.
5. Deligiannakis, Y., Boussac, A., and Rutherford, A. W. (1995) ESEEM study of the plastoquinone anion radical (Q_A^-) in ^{14}N- and ^{15}N-labeled photosystem II treated with cyanide, *Biochemistry 34*, 16030-16038.
6. Deligiannakis, Y., Hanley, J., and Rutherford, A. W. (1999) 1D- and 2D-ESEEM Study of the Semiquinone Radical Q_A^- of Photosystem II, *J. Am. Chem. Soc. 121*, 7653-7664.
7. Martin, E., Samoilova, R. I., Narasimhulu, K. V., Wraight, C. A., and Dikanov, S. A. (2010) Hydrogen bonds between nitrogen donors and the semiquinone in the Q_B site of bacterial reaction centers, *J. Am. Chem. Soc. 132*, 11671-11677.
8. Stowell, M. H. B., McPhillips, T. M., Rees, D. C., Soltis, S. M., Abresch, E., and Feher, G. (1997) Light-induced structural changes in photosynthetic reaction center: implication for mechanism of electron-proton transfer, *Science 276*, 812-816.
9. Lubitz, W., and Feher, G. (1999) The primary and secondary acceptors in bacterial photosynthesis III. Characterization of the quinone radicals Q_A^- and Q_B^- by EPR and ENDOR, *Appl. Magn. Reson. 17*, 1-48.
10. Paddock, M. L., Chang, C., Xu, Q., Abresch, E. C., Axelrod, H. L., Feher, G., and Okamura, M. Y. (2005) Quinone (Q_B) reduction by B-branch electron transfer in mutant bacterial reaction centers from *Rhodobacter sphaeroides*: quantum efficiency and X-ray structure., *Biochemistry 44*, 6920-6928.
11. Axelrod, H. L., Abresch, E. C., Paddock, M. L., Okamura, M. Y., and Feher, G. (2000) Determination of the binding sites of the proton transfer inhibitors Cd^{2+} and Zn^{2+} in bacterial reaction centers., *Proc. Natl. Acad. Sci. USA 97*, 1542-1547.
12. Koepke, J., Eva-Maria Krammer, E.-M., Klingen, A. R., Sebban, P., Ullmann, G. M., and Fritzsch, G. (2007) pH modulates the quinone position in the photosynthetic reaction center from *Rhodobacter sphaeroides* in the neutral and charge separated states. , *J. Mol. Biol. 371*, 13.

13. M. L. Paddock, G. F., M. Y. Okamura. (1995) Pathway of proton transfer in bacterial reaction centers: Further investigations on the role of Ser-L223 studied by site-directed mutagenesis, *Biochemistry 34*, 15742-15750.
14. Xu, Q., Axelrod, H. L., Abresch, E. C., Paddock, M. L., Okamura, M. Y., and Feher, G. (2004) X-Ray structure determination of three mutants of the bacterial photosynthetic reaction centers from *Rb. sphaeroides*; altered proton transfer pathways., *Structure 12*, 703-715.
15. Paddock, M. L., Flores, M., Isaacson, R., Chang, C., Abresch, E. C., and Okamura, M. Y. (2007) ENDOR spectroscopy reveals light induced movement of the H-bond from Ser-L223 upon forming the semiquinone (Q_B^-) in reaction centers from *Rhodobacter sphaeroides*, *Biochemistry 46*, 8234-8243.
16. Dikanov, S. A., Samoilova, R. I., Kolling, D. R. J., Holland, J. T., and Crofts, A. R. (2004) Hydrogen bonds involved in binding the Q_i-site semiquinone in the bc_1 complex, identified through deuterium exchange using pulsed EPR, *J. Biol. Chem. 279*, 15814-15823.
17. Yap, L. L., Samoilova, R. I., Gennis, R. B., and Dikanov, S. A. (2007) Characterization of mutants that change the hydrogen bonding of the semiquinone radical at the Q_H site of the cytochrome bo_3 from *Escherichia coli*, *Journal of Biological Chemistry 282*, 8777-8785.
18. Paddock, M. L., Flores, M., Isaacson, R., Chang, C., Abresch, E. C., Selvaduray, P., and Okamura, M. Y. (2006) Trapped conformational states of semiquinone ($D^+Q_B^-$) formed by B-branch electron transfer at low temperature in *Rhodobacter sphaeroides* reaction centers., *Biochemistry 45*, 14032-14042.
19. Stoll, S., Calle, C., Mitrikas, G., and Schweiger, A. (2005) Peak suppression in ESEEM spectra of multinuclear spin systems, *J. Magn. Res. 177*, 93-101.
20. Kolling, D. R., Samoilova, R. I., Shubin, A. A., Crofts, A. R., and Dikanov, S. A. (2009) Proton environment of reduced Rieske iron-sulfur cluster probed by two-dimensional ESEEM spectroscopy., *J. Phys. Chem. A 113*, 653-667.
21. Flores, M., Isaacson, R., Abresch, E., Calvo, R., Lubitz, W., and Feher, G. (2006) Protein-cofactor interactions in bacterial reaction centers from *Rhodobacter sphaeroides* R-26: I. Identification of the ENDOR lines associated with the hydrogen bonds to the primary quinone Q_A^-, *Biophys. J. 90*, 3356-3362.
22. Flores, M., Isaacson, R., Abresch, E., Calvo, R., Lubitz, W., and Feher, G. (2007) Protein-cofactor interactions in bacterial reaction centers from *Rhodobacter sphaeroides* R-26: II. Geometry of the hydrogen bonds to the primary quinone formula by ^1H and ^2H ENDOR spectroscopy., *Biophys. J. 92*, 671-682.
23. Dikanov, S. A., and Bowman, M. K. (1995) Cross-peak lineshape of two-dimensional ESEEM spectra in disordered S = 1/2, I = 1/2 spin systems, *J. Magn. Res. A 116*, 125-128.
24. Lin, T.-J., and O'Malley, P. J. (2008) An ONIOM study of the Q_A site semiquinone in the *Rhodobacter sphaeroides* photosynthetic reaction centre*, J. Mol Struct. 870*, 31-35.

Figures

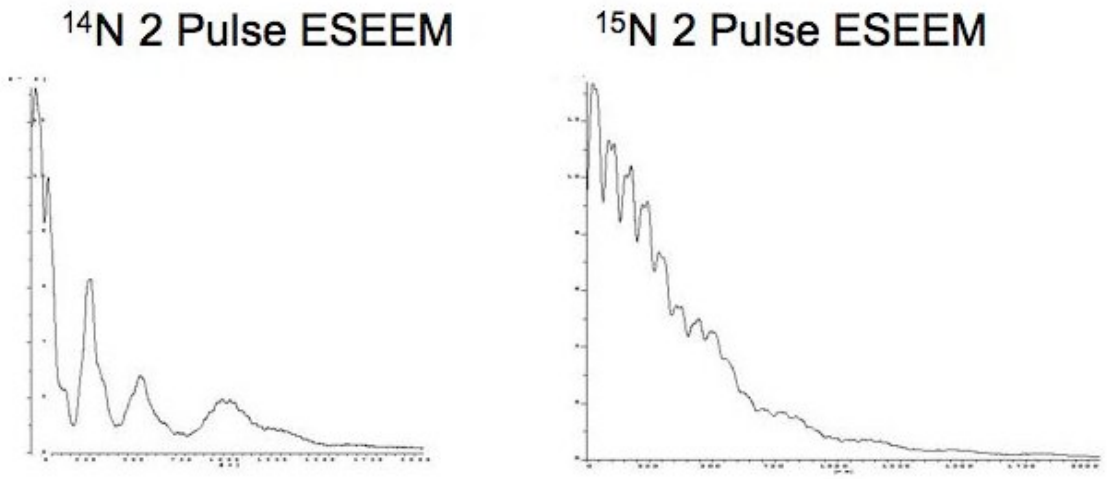

Figure 6.1. Two-pulse ESEEM spectra of Q_A^-. The spectrum on the right shows the significant decrease in ESEEM modulation depth after ^{15}N enrichment.

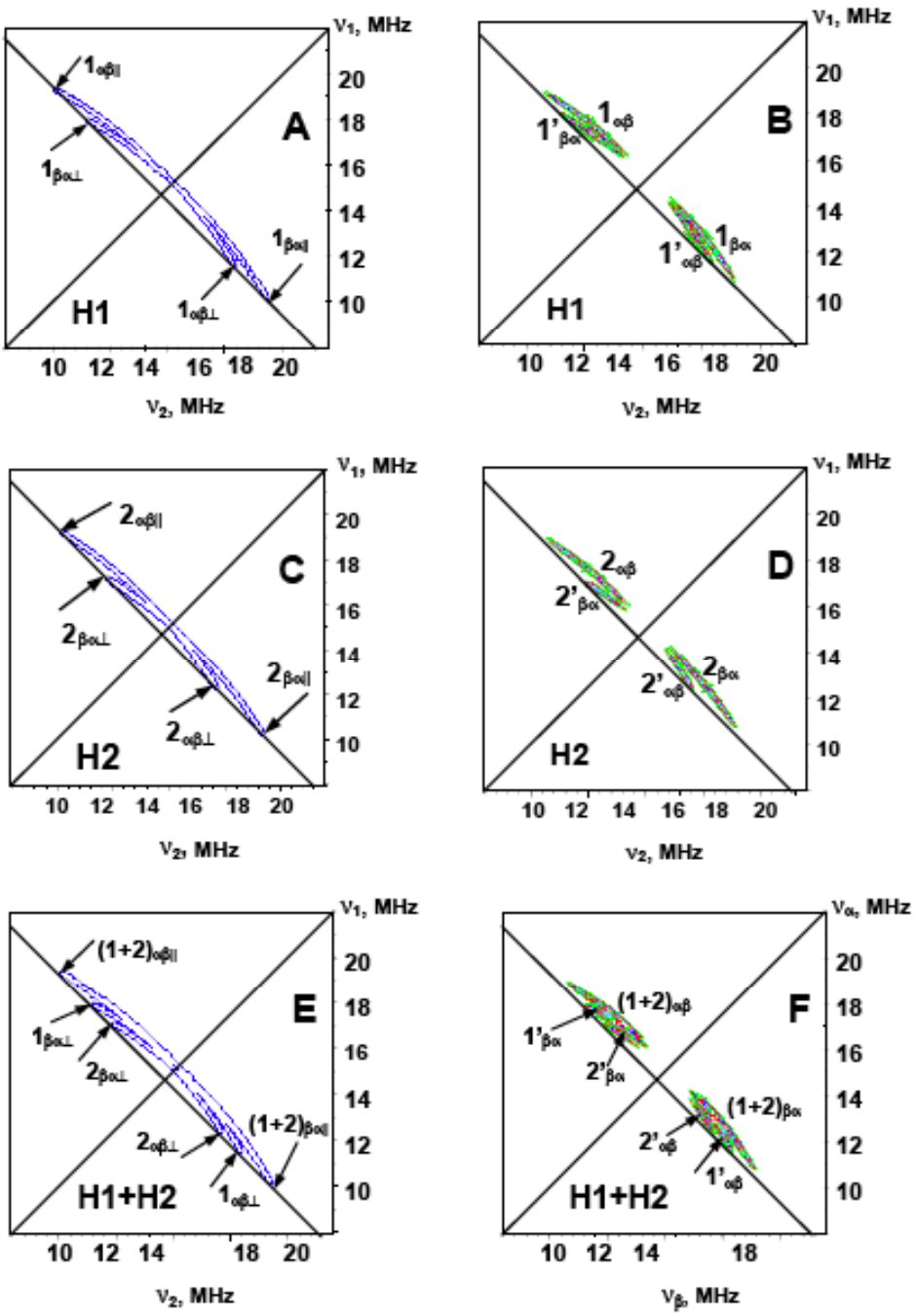

Figure 6.2. Simulated HYSCORE data based on ENDOR proton couplings to Q_A^-. In panels A, C and E the locations of crossridges for two protons (H1 and H2) are given without any consideration given to suppression effects present in actual HYSCORE spectra. Panels B, D and F show the corresponding simulated HYSCORE spectra calculated with τ = 136 ns.

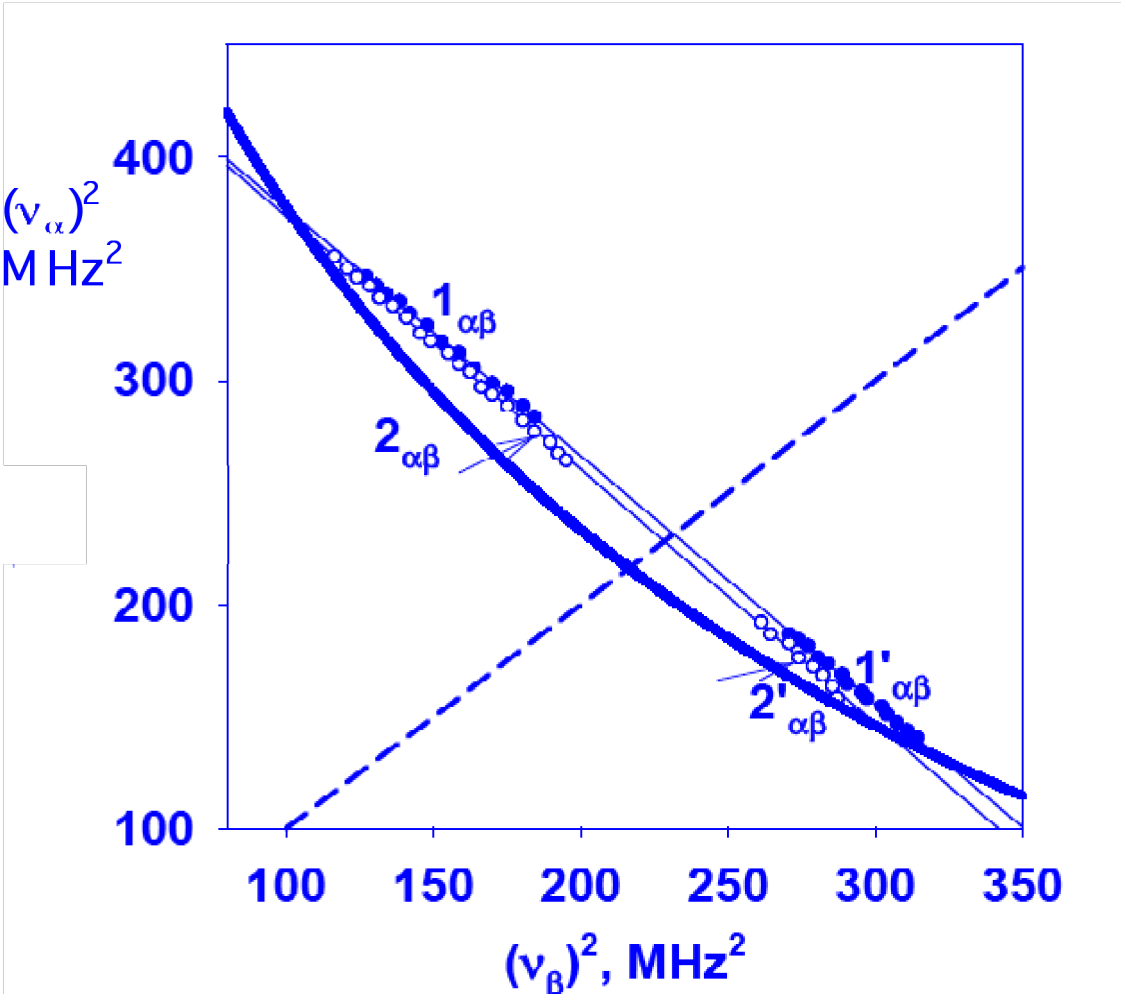

Figure 6.3. Coordinates of points along the ridges in the simulated HYSCORE spectrum plotted as ν_α^2 versus ν_β^2. Narrow, solid lines indicate the linear relationship between 1 and 1' and 2 and 2'. The narrow, dashed line represents the diagonal in the related HYSCORE spectrum. The bold curve is $\nu_\alpha + \nu_\beta = 2\nu_I$ where ν_I is the proton frequency 14.7 MHz.

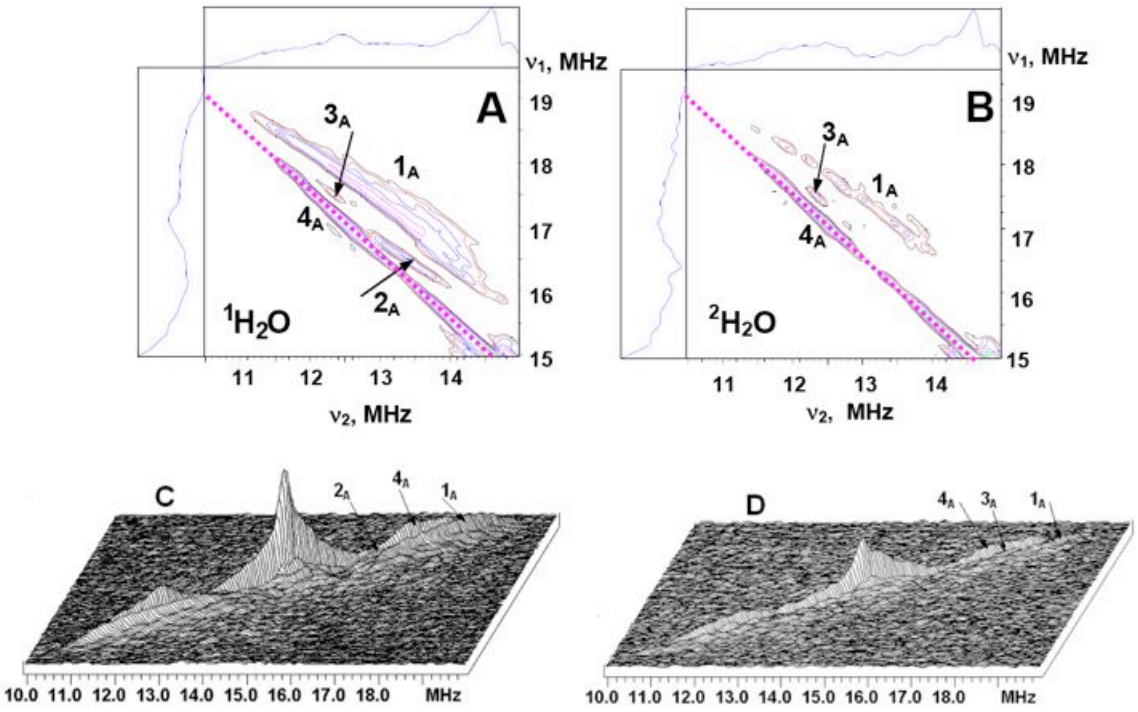

Figure 6.4. The ^1H HYSCORE spectrum of Q_A^- in ^1H_2O (A and C) and ^2H_2O (B and D) buffer. A and B show the spectra presented in contour representation while C and D show stacked representations of the same spectra (rotated 90 degrees with respect to A and B for clarity). In C, peak **3**$_A$ is hidden between ridges **1**$_A$ and **4**$_A$. Spectra were obtained as a sum of three individual spectra recorded with time between first and second pulses τ=136, 200, and 400 ns.

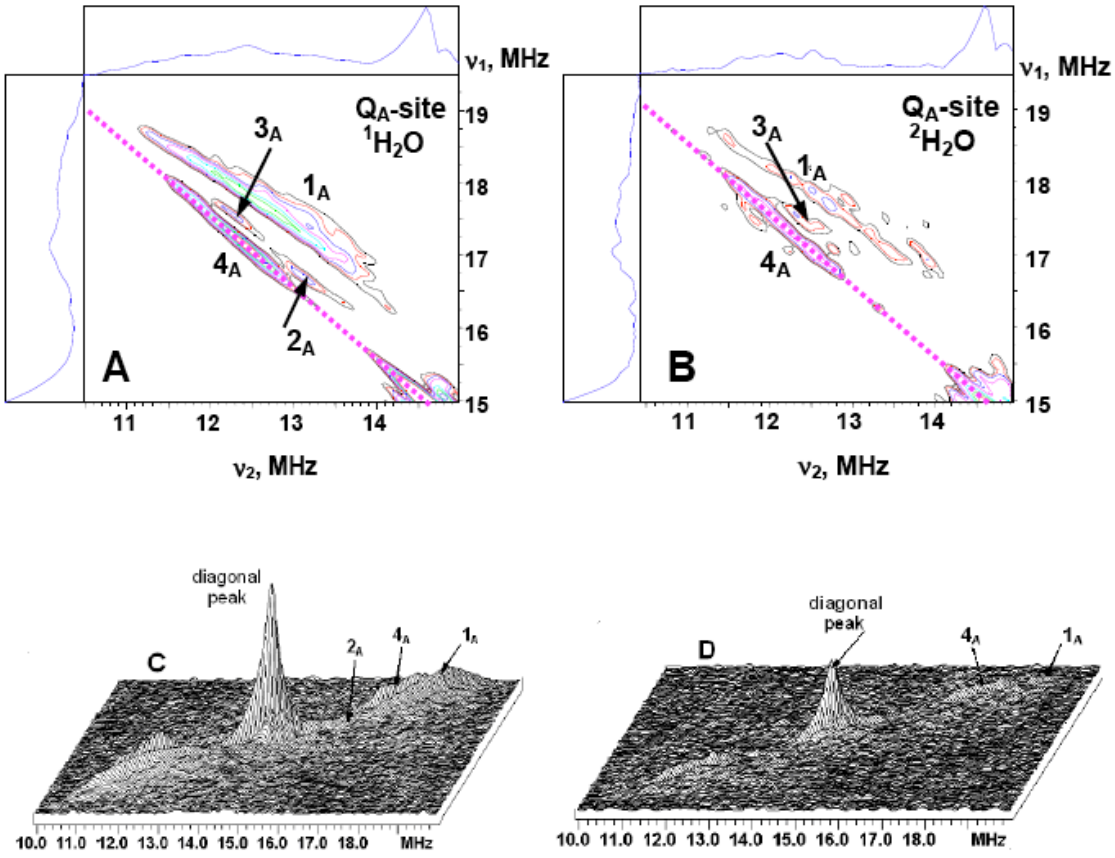

Figure 6.5. The ^{1}H HYSCORE spectrum of Q_A^- in $^{1}H_2O$ (A and C) and $^{2}H_2O$ (B and D) buffer. A and B show the spectra presented in contour representation while C and D the stacked representation of the same spectra (rotated 90 degrees with respect to A and B for clarity). In C, peak $\mathbf{3_A}$ is hidden between ridges $\mathbf{1_A}$ and $\mathbf{4_A}$. Spectra were obtained with τ=136 ns

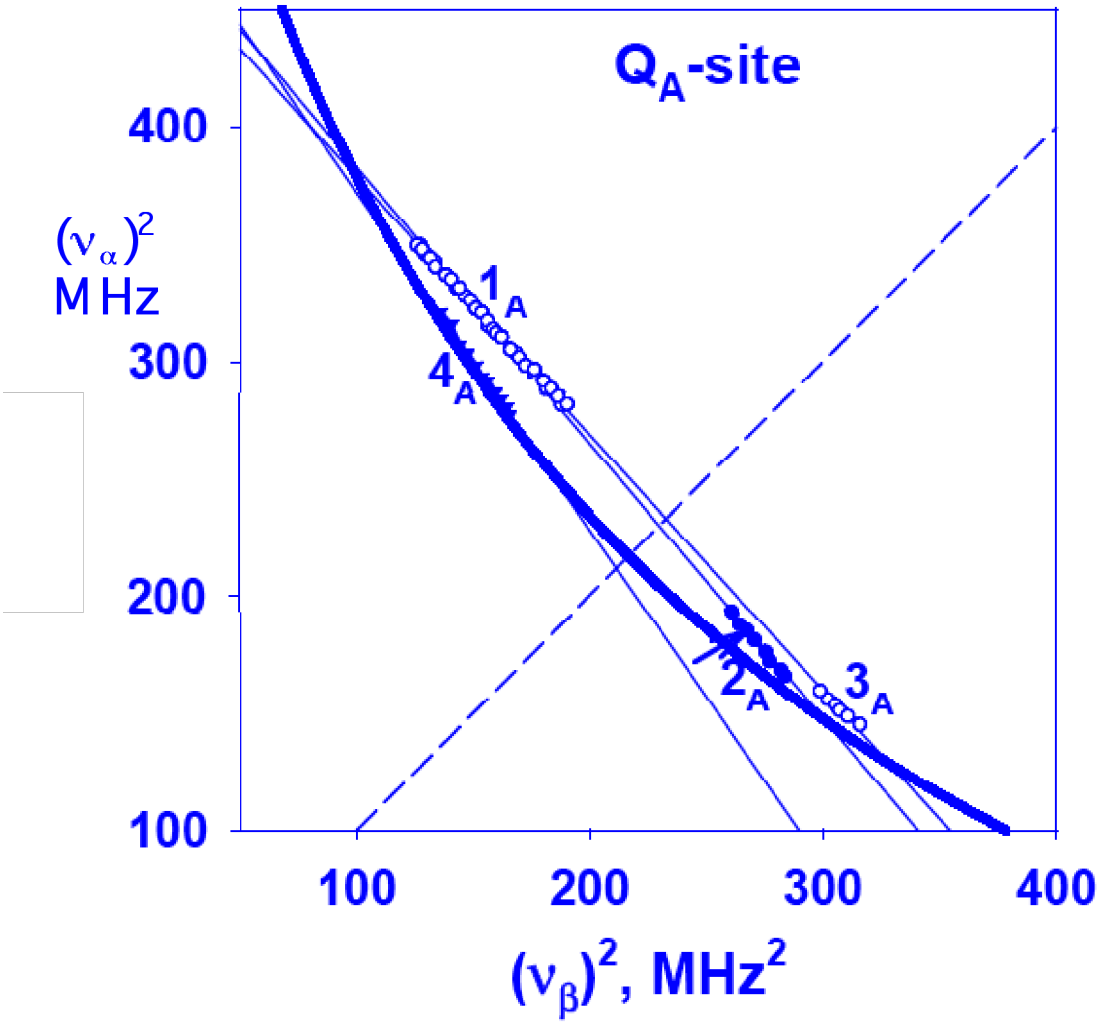

Figure 6.6. Coordinates from crosspeaks 1_A, 4_A and the permutated coordinates from 2_A and 3_A, from the ^{1}H HYSCORE Q_A^- spectrum, plotted as ν_α^2 versus ν_β^2. Narrow, solid lines indicate the linear relationship between 1_A and 2_A or 3_A. The narrow, dashed line represents the diagonal in the related HYSCORE spectrum. The bold curve is $\nu_\alpha + \nu_\beta = 2\nu_I$ where ν_I is the proton frequency 14.7 MHz.

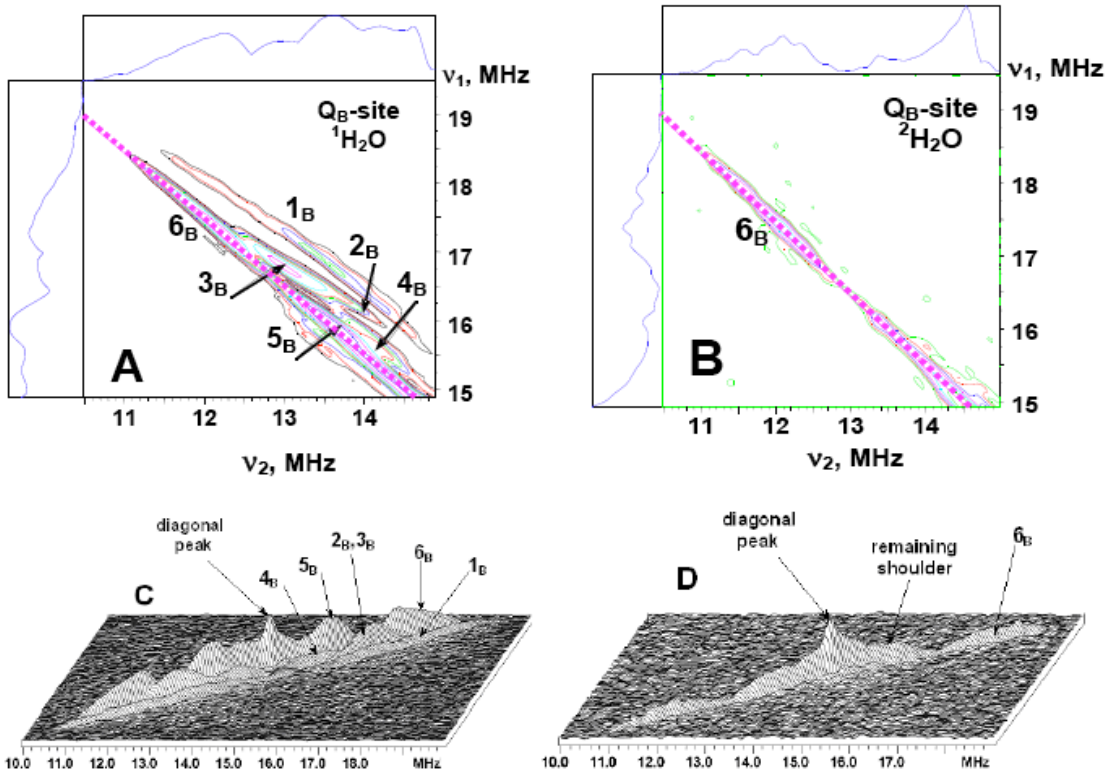

Figure 6.7. The Q_B^- ^1H HYSCORE spectrum in ^1H_2O (A and C) and ^2H_2O (B and D) buffer. A and B show the spectra presented in contour representation while C and D the stacked representation of the same spectra. Spectra were obtained with only τ=136, 200, and 400 ns.

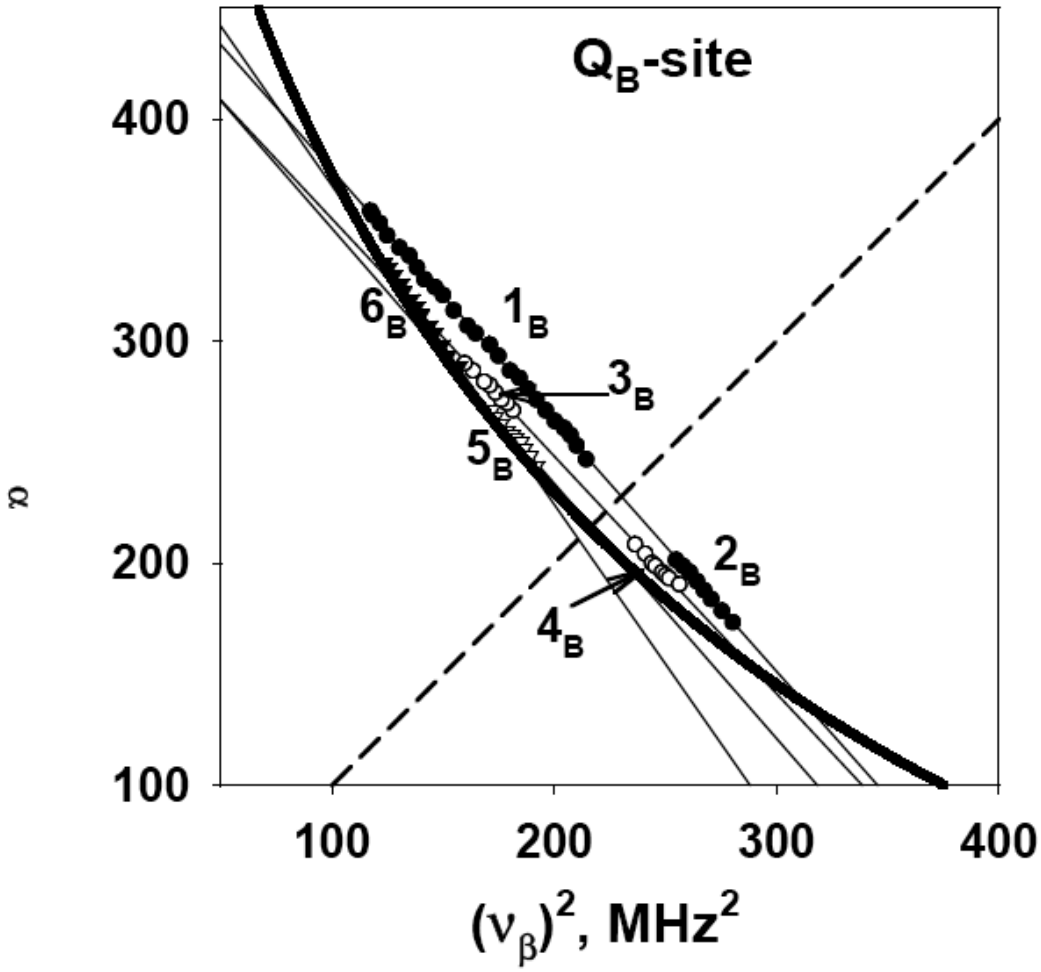

Figure 6.8. Coordinates from crosspeaks 1_B, 3_B, 5_B, 6_B and the permuted coordinates from 2_B and 4_B from the ^{1}H HYSCORE Q_B^- spectrum plotted as ν_α^2 versus ν_β^2. Narrow, solid lines indicate the linear relationship between crossridges. The narrow, dashed line represents the diagonal in the related HYSCORE spectrum. The bold curve is $\nu_\alpha + \nu_\beta = 2\nu_I$ where ν_I is the proton frequency 14.7 MHz.

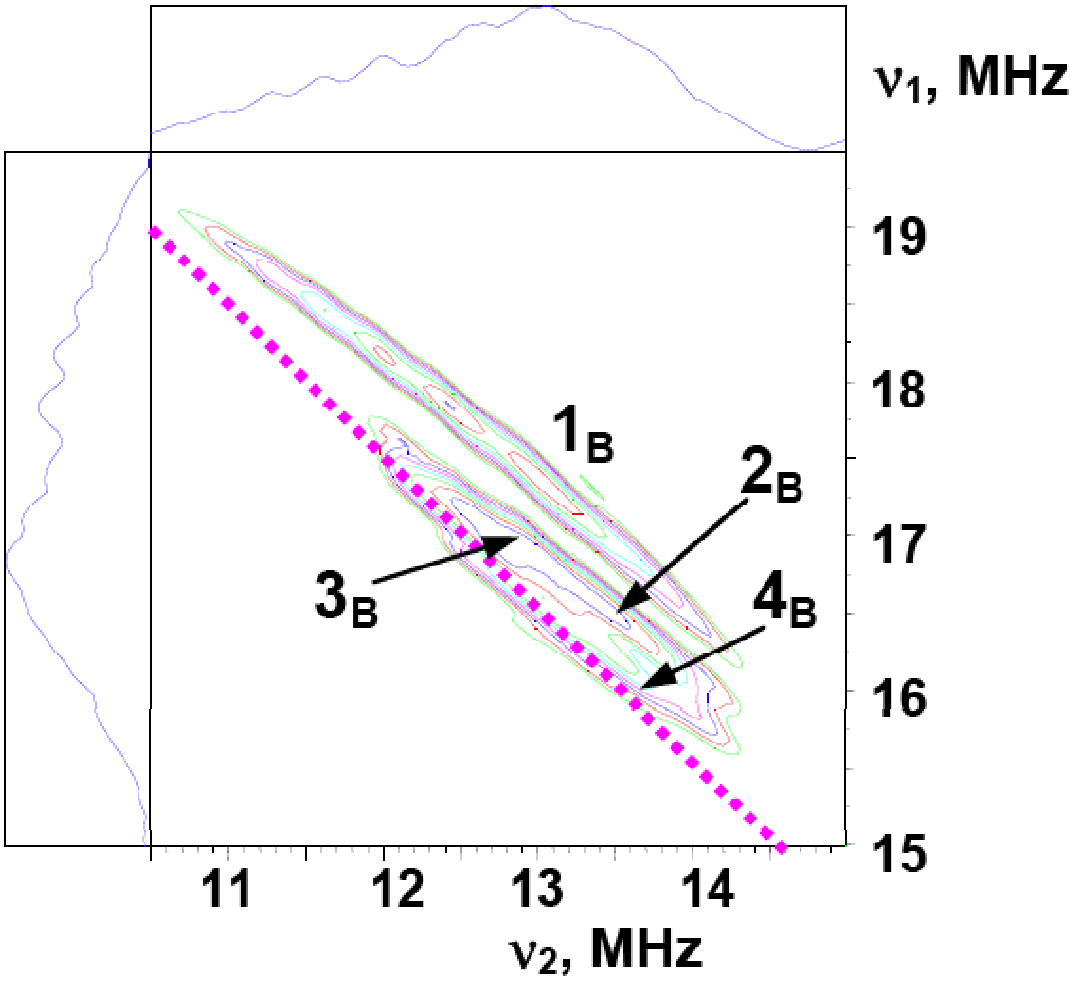

Figure 6.9. Simulated HYSCORE spectrum, above the diagonal, based on HFI tensors provided by combined QM/MM calculations. The three protons implicated in calculations generate similar features as seen in experimental HYSCORE.